NASA CR-112254

A THEORETICAL STUDY OF MIXING DOWNSTREAM OF TRANSVERSE INJECTION INTO A SUPERSONIC BOUNDARY LAYER

By

A.J. Baker and S.W. Zelazny

Prepared under Contract No. NAS1-11214 by

Bell Aerospace Company
P.O. Box 1, Buffalo, New York

For Langley Research Center
NATIONAL AERONAUTICS AND SPACE ADMINISTRATION

1. Report No. NASA CR-112254	2. Government Accession No.	3. Recipient's Catalog No.
4. Title and Subtitle A Theoretical Study of Mixing Downstream of Tranverse Injection into a Supersonic Boundary Layer.		5. Report Date December 1972 6. Performing Organization Code
7. Author(s) A. J. Baker, S. W. Zelazny		8. Performing Organization Report No. 9500-920263
9. Performing Organization Name and Address Bell Aerospace Company P.O. Box One Buffalo, New York 14240		10. Work Unit No. 11. Contract or Grant No. NAS1-11214
12. Sponsoring Agency Name and Address National Aeronautics & Space Administration Washington, D.C. 20546		13. Type of Report and Period Covered Contractor Report 14. Sponsoring Agency Code
15. Supplementary Notes		

16. Abstract

A theoretical and analytical study was made of mixing downstream of transverse hydrogen injection, from single and multiple orifices, into a Mach 4 air boundary layer over a flat plate. Numerical solutions to the governing three-dimensional, elliptic boundary layer equations were obtained using a general purpose computer program (COMOC) founded upon a finite element solution algorithm. A prototype three-dimensional turbulent transport model was developed using mixing length theory in the wall region and the mass defect concept in the outer region.

Excellent agreement between the COMOC-computed flow field and experimental data for a jet/freestream dynamic pressure ratio of unity was obtained in the centerplane region of the single-jet configuration. Poorer agreement off centerplane suggests an inadequacy of the extrapolated two-dimensional turbulence model. Considerable improvement in off-centerplane computational agreement occurred for a multi-jet configuration, using the same turbulent transport model.

One alternative to requiring detailed initial condition data was explored, i.e., a "virtual source" concept, wherein the complex transverse injection phenomena is computationally replaced by a hydrogen jet imbedded within the air boundary layer, the distinguishing features of which are solely a function of freestream and injectant parameters. A theoretical model for establishing initial conditions for a virtual source was derived. Good computational agreement with experimental data for the multiple-injector configuration was obtained for three dynamic pressure ratios (q_r = 0.5, 1.0, 1.5).

COMOC was adapted to compute a mixing efficiency parameter defined as the percentage of hydrogen that could stoichiometrically react in a given concentration and velocity distribution within the air boundary layer. Mixing was determined to be noticeably poorer for q_r = 1.5 than the other two dynamic pressure ratios. Sample results are discussed illustrating how the COMOC predictive analysis capability may be expanded to compute actual reacting flows of practical interest in combustor design and optimization.

17. Key Words (Selected by Author(s))	18. Distribution Statement
Computer Program Scramjet Mixing Finite Elements Turbulent boundary layer Three-dimensional elliptic boundary layer	Unclassified - Unlimited

19. Security Classif. (of this report)	20. Security Classif. (of this page)	21. No. of Pages	22. Price*
Unclassified	Unclassified	69	

*For sale by the Clearinghouse for Federal Scientific and Technical Information, Springfield, Virginia 22151.

ACKNOWLEDGMENT

The authors wish to gratefully acknowledge the support given this work by Bell Aerospace Company, and in particular Mr. Joe Orzechowski, whose innovative programming efforts have made COMOC operational. We also wish to thank Mr. Paul Manhardt, who helped in many ways, and Dr. F. D. Hains for his assistance with the virtual-source.

1. Report No. NASA CR-112254	2. Government Accession No.	3. Recipient's Catalog No.
4. Title and Subtitle A Theoretical Study of Mixing Downstream of Tranverse Injection into a Supersonic Boundary Layer.		5. Report Date December 1972 6. Performing Organization Code
7. Author(s) A. J. Baker, S. W. Zelazny		8. Performing Organization Report No. 9500-920263
9. Performing Organization Name and Address Bell Aerospace Company P.O. Box One Buffalo, New York 14240		10. Work Unit No. 11. Contract or Grant No. NAS1-11214
12. Sponsoring Agency Name and Address National Aeronautics & Space Administration Washington, D.C. 20546		13. Type of Report and Period Covered Contractor Report 14. Sponsoring Agency Code
15. Supplementary Notes		

16. Abstract

A theoretical and analytical study was made of mixing downstream of transverse hydrogen injection, from single and multiple orifices, into a Mach 4 air boundary layer over a flat plate. Numerical solutions to the governing three-dimensional, elliptic boundary layer equations were obtained using a general purpose computer program (COMOC) founded upon a finite element solution algorithm. A prototype three-dimensional turbulent transport model was developed using mixing length theory in the wall region and the mass defect concept in the outer region.

Excellent agreement between the COMOC-computed flow field and experimental data for a jet/freestream dynamic pressure ratio of unity was obtained in the centerplane region of the single-jet configuration. Poorer agreement off centerplane suggests an inadequacy of the extrapolated two-dimensional turbulence model. Considerable improvement in off-centerplane computational agreement occurred for a multi-jet configuration, using the same turbulent transport model.

One alternative to requiring detailed initial condition data was explored, i.e., a "virtual source" concept, wherein the complex transverse injection phenomena is computationally replaced by a hydrogen jet imbedded within the air boundary layer, the distinguishing features of which are solely a function of freestream and injectant parameters. A theoretical model for establishing initial conditions for a virtual source was derived. Good computational agreement with experimental data for the multiple-injector configuration was obtained for three dynamic pressure ratios (q_r = 0.5, 1.0, 1.5).

COMOC was adapted to compute a mixing efficiency parameter defined as the percentage of hydrogen that could stoichiometrically react in a given concentration and velocity distribution within the air boundary layer. Mixing was determined to be noticeably poorer for q_r = 1.5 than the other two dynamic pressure ratios. Sample results are discussed illustrating how the COMOC predictive analysis capability may be expanded to compute actual reacting flows of practical interest in combustor design and optimization.

17. Key Words (Selected by Author(s))	18. Distribution Statement
Computer Program Scramjet Mixing Finite Elements Turbulent boundary layer Three-dimensional elliptic boundary layer	Unclassified - Unlimited

19. Security Classif. (of this report)	20. Security Classif. (of this page)	21. No. of Pages	22. Price*
Unclassified	Unclassified	69	

*For sale by the Clearinghouse for Federal Scientific and Technical Information, Springfield, Virginia 22151.

CONTENTS

ILLUSTRATIONS

CONTENTS

ILLUSTRATIONS (CONT)

A THEORETICAL STUDY OF MIXING DOWNSTREAM OF TRANSVERSE INJECTION INTO A SUPERSONIC BOUNDARY LAYER

A. J. Baker and S. W. Zelazny

Bell Aerospace Company

SUMMARY

This report presents the results of a theoretical and analytical study of mixing downstream of transverse hydrogen injection, from single and multiple orifices, into a Mach 4 air boundary layer flow over a flat plate. Numerical solutions to the governing three-dimensional, elliptic boundary layer equations were obtained using a general purpose computer program (COMOC) founded upon a finite element solution algorithm. The concepts of two-dimensional turbulent mixing length and mass defect theories were extended to establish a prototype three-dimensional turbulent transport model.

Excellent agreement between the COMOC-computed flow field and experimental data for a jet/freestream dynamic pressure ratio of unity was obtained in the centerplane region of the single jet configuration. Poorer agreement off centerplane may be indicative of the inadequacy of the extrapolated two-dimensional turbulence model that neglects flow field three-dimensionality. A considerable improvement in off-centerplane computational agreement occurred for a multi-jet configuration, using the same turbulent transport model.

Some of the computational disagreement with measurements may well reflect initial condition variability. One alternative to requiring detailed initial data is to employ the "virtual source" concept, wherein the complex transverse injection phenomena is computationally replaced by a hydrogen jet imbedded within the air boundary layer, the distinguising features of which are solely a function of freestream and injectant parameters. A theoretical model for establishing initial conditions for a virtual source was derived. Very good computational agreement with experimental data was obtained for the multiple injector geometry for the three dynamic pressure ratios investigated (q_r = 0.5, 1.0, 1.5), at stations up to 60 (injector orifice) diameters downstream. Single jet comparisons could be obtained using the virtual source concept, if desired by a simple change in lateral boundary condition specifications.

The COMOC-computed solutions for the three-dimensional flow field provide considerably detailed information, much more than is typically available by experimental means. Important design guidance for the engineer may be obtained by integrating these data over the problem solution domain to generate scalar correlating parameters. Since the prediction of reacting flows is an ultimate goal, a simple integral parameter, defined as the percentage of hydrogen that could stoichiometrically react in a given concentration and velocity distribution within the air boundary layer was computed. Shown in figure 1 are the COMOC-computed mixing efficiencies, η, for the "virtual source" modeling of multi-jet injection, as a function of distance downstream from the injection orifice. Mixing efficiency is computed to be noticeably poorer for q_r = 1.5 than the other two dynamic pressure ratio conditions.

COMOC can be readily expanded to predict either equilibrium or finite rate chemistry for the three-dimensional mixing problem. On a relative basis, however, if reaction is fast, hence diffusion con-

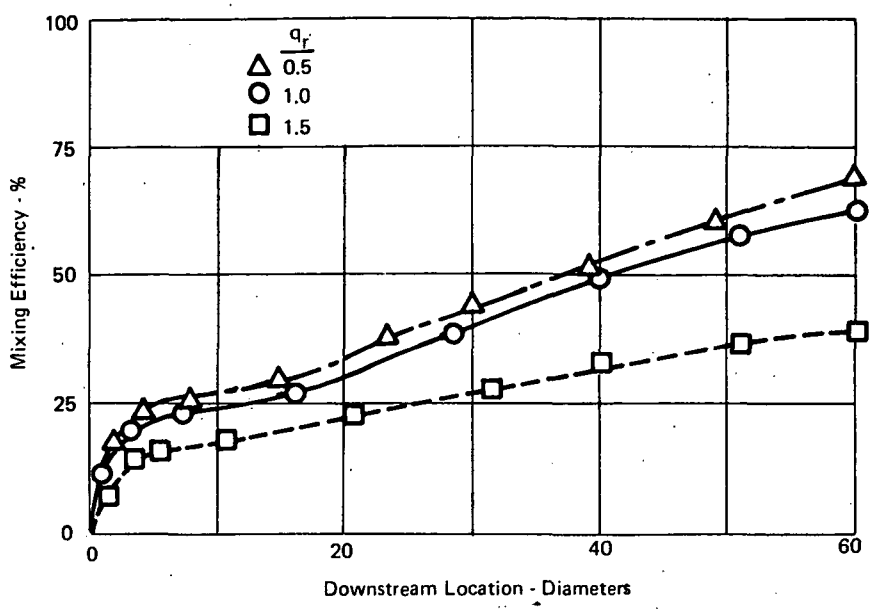

Figure 1. COMOC Computed Mixing Efficiency for Virtual Source, Multi-Jet Configuration for Three Dynamic Pressure Ratios

trolled, the computation of mixing efficiency for a cold flow configuration may provide important design guidance, by capturing the detailed three-dimensional computed flow field description within a single scalar parameter.

INTRODUCTION

The hydrogen fueled scramjet engine is a prominent candidate for propulsion of the next generation of hypersonic cruise vehicles, see for example Becker and Kirkham (ref. 1) and Bushnell (ref. 2). An airframe-integrated underbody engine configuration has been suggested (ref. 3), and design considerations are discussed by Henry and Anderson (ref. 4). Over the years many alternative designs have been proposed by the Air Force, Navy, and NASA as well. They all enjoy a certain commonality in that fuel introduction arrangements typically consist of rows of circular, choked flow fuel injector orifices mounted flush or normal to the combustor wall or in fins spanning the combustor inlet. The various proposed component designs have largely emerged from experimentation wherein empirical relations have established a preliminary configuration for a starting point. Early attempts to establish a theoretical basis for this developing technology have been confined by lack of detailed data over the complete three-dimensional flow field. Since the pattern of fuel injection, hence three-dimensional mixing, will exert significant influence on combustor performance, an in-depth analytical analysis of the complex three-dimensional flow fields is required to lend critical support to design technology.

The results of comprehensive experimentation on prototype injector subsystems are now becoming available. For example, Rogers has performed detailed measurements over the entire three-dimensional mixing region downstream of hydrogen injection from a single discrete orifice (ref. 5), and multiple, laterally-disposed orifices (ref. 6), into a Mach 4 airstream over a flat plate. Similar measurements for a Mach 2.7 airstream, including Schlieren photographs of the near injection region, are reported by Wagner, Cameron and Billig (ref. 7). These data are not only useful for

A THEORETICAL STUDY OF MIXING DOWNSTREAM OF TRANSVERSE INJECTION INTO A SUPERSONIC BOUNDARY LAYER

A. J. Baker and S. W. Zelazny

Bell Aerospace Company

SUMMARY

This report presents the results of a theoretical and analytical study of mixing downstream of transverse hydrogen injection, from single and multiple orifices, into a Mach 4 air boundary layer flow over a flat plate. Numerical solutions to the governing three-dimensional, elliptic boundary layer equations were obtained using a general purpose computer program (COMOC) founded upon a finite element solution algorithm. The concepts of two-dimensional turbulent mixing length and mass defect theories were extended to establish a prototype three-dimensional turbulent transport model.

Excellent agreement between the COMOC-computed flow field and experimental data for a jet/freestream dynamic pressure ratio of unity was obtained in the centerplane region of the single jet configuration. Poorer agreement off centerplane may be indicative of the inadequacy of the extrapolated two-dimensional turbulence model that neglects flow field three-dimensionality. A considerable improvement in off-centerplane computational agreement occurred for a multi-jet configuration, using the same turbulent transport model.

Some of the computational disagreement with measurements may well reflect initial condition variability. One alternative to requiring detailed initial data is to employ the "virtual source" concept, wherein the complex transverse injection phenomena is computationally replaced by a hydrogen jet imbedded within the air boundary layer, the distinguishing features of which are solely a function of freestream and injectant parameters. A theoretical model for establishing initial conditions for a virtual source was derived. Very good computational agreement with experimental data was obtained for the multiple injector geometry for the three dynamic pressure ratios investigated (q_r = 0.5, 1.0, 1.5), at stations up to 60 (injector orifice) diameters downstream. Single jet comparisons could be obtained using the virtual source concept, if desired by a simple change in lateral boundary condition specifications.

The COMOC-computed solutions for the three-dimensional flow field provide considerably detailed information, much more than is typically available by experimental means. Important design guidance for the engineer may be obtained by integrating these data over the problem solution domain to generate scalar correlating parameters. Since the prediction of reacting flows is an ultimate goal, a simple integral parameter, defined as the percentage of hydrogen that could stoichiometrically react in a given concentration and velocity distribution within the air boundary layer was computed. Shown in figure 1 are the COMOC-computed mixing efficiencies, η, for the "virtual source" modeling of multi-jet injection, as a function of distance downstream from the injection orifice. Mixing efficiency is computed to be noticeably poorer for q_r = 1.5 than the other two dynamic pressure ratio conditions.

COMOC can be readily expanded to predict either equilibrium or finite rate chemistry for the three-dimensional mixing problem. On a relative basis, however, if reaction is fast, hence diffusion con-

determining the mixing resulting from various given injector configurations but, of equal importance, they provide the required accuracy comparison for theoretical analysis of the resultant turbulent flow fields. Concomitant with the establishment of appropriate models for turbulent mass and momentum transport coefficient distributions in three-dimensional flow fields will be the emergence of the capability to perform analytical studies for both detailed flow description and design optimization. The success of this approach depends upon establishment of a proven capability to model the three-dimensional viscous flow field equations numerically, and to generate computational solutions for practical geometrical configurations.

This numerical analysis capability is now operational within the COMOC general purpose computer program system. The theoretical foundation for COMOC is a finite element solution algorithm for a generalized initial-valued, quasi-linear elliptic boundary value partial differential equation, systems of which typically describe the mechanics and thermodynamics of continuum mechanical phenomena. Employing an extrapolation of two-dimensional mixing length/mass defect turbulent transport concepts, as a prototype three-dimensional turbulent transport model, an analytical study of mixing downstream of transverse hydrogen injection into a Mach 4, three-dimensional air boundary layer flow over a flat plate has been performed using COMOC. Detailed numerical prediction of the flow field is presented, in a solution domain spanning 30 to 120 injector diameters downstream, for the single jet geometry of Rogers (ref. 5), for a jet to freestream dynamic pressure ratio (q_r) of unity, an injection orifice diameter (D) equal to 0.102 cm (0.040 in.), stagnation freestream pressure of 13.6 atm (1 atm = 101.325 kN/m^2) and a stagnation temperature of 300°K. These conditions correspond to a Reynolds number per meter of 6.19×10^7; the boundary layer thickness at the injector longitudinal station was equal to 2.7 injector diameters. The results of computations for a multi-jet configuration, with injector separation equal to 12.5 injector diameters, are also presented, for the freestream conditions similar to the single-jet case.

Considerable experimental data management is required to establish initial conditions for numerical three-dimensional solutions. A candidate alternative method is computational replacement of the complex injection and turning phenomena with a "virtual source" of injectant imbedded within the air boundary layer flow. A theory is presented to establish the initial condition specification of a virtual source configuration based solely upon freestream and injectant parameters. Employing the same extrapolated turbulence model as before, analytical results are presented for propagation of the virtual source of hydrogen into the downstream mixing region, for a solution domain spanning 0 to 60 injector diameters downstream. The computational configuration is identical to the multi-jet geometry of Rogers, and results are established for the three dynamic pressure ratios of $q_r = 0.5$, 1.0, and 1.5. The agreement between computed and experimentally measured data is described in terms of decay of the maximum hydrogen concentration, trajectory of the maximum concentration, and lateral spreading of the diffusion pattern.

For all computational solutions, COMOC was adapted to compute the integral mixing efficiency parameter, η, of ref. 6. The potential usefulness of this scalar correlation parameter as a design optimization tool on a relative basis is discussed. Combustion data are required to establish an absolute comparison basis. Sample results are discussed illustrating how the COMOC predictive analysis capability can be expanded to compute the actual reacting flows of practical interest in combustor design and optimization.

THE DIFFERENTIAL EQUATION SYSTEM GOVERNING THREE-DIMENSIONAL MIXING FLOW FIELDS

The description of a state point in viscous fluid mechanics is contained within the solution of the system of coupled, nonlinear, second-order partial differential equations enforcing local conservation of species mass, total mass, linear momentum, and energy. Closure of this equation system requires identification of constitutive laws. For laminar flows, transport properties such as viscosity and thermal conductivity are describable in terms of molecular behavior and therefore dependent solely upon the material present. In turbulent flows, the time-averaged Navier-Stokes equations appear identical to the laminar flow equations, after identification of turbulent or "eddy" transport coefficients which are dependent upon the kinematics of the flow field and not the molecular properties of the fluid. In this development, a generalized transport property description is assumed, which may be selectively laminar or turbulent as required.

An illustration of the subject three-dimensional flow field is shown in figure 2. The predominant direction of flow is aligned with the x axis. Although the essential character of the flow is boundary layer, the common three-dimensional boundary layer equations, (ref. 8) are an insufficient description, since some dependent variable gradients in the lateral direction (z axis) may not be uniformly negligible (in comparison to those parallel to the y axis). The governing equation system is thus the elliptic boundary layer form of the parabolic Navier-Strokes equations, which retain all derivatives in the lateral flow direction. The three-dimensional velocity vector $\vec{U}$ has scalar components in the rectangular Cartesian basis, figure 2 as

$$\vec{U} \equiv u\hat{i}+v\hat{j}+w\hat{k} \tag{1}$$

It is useful to identify a two-dimensional vector differential operator ∇_2,

$$\nabla_2 \equiv \hat{j}(\ )_{,y}+\hat{k}(\ )_{,z} \tag{2}$$

and the comma notation signifies partial differentiation. The three-dimensional, elliptic boundary layer equations for a multispecies and compressible fluid can then be written as,

Global Continuity:

$$0 = \nabla_2 \cdot (\rho\vec{U}) \qquad + (\rho u)_{,x} \tag{3}$$

i^{th} Species Continuity:

$$\rho u Y^i_{,x} = \nabla_2 \cdot (\frac{\mu Le}{Pr} \nabla_2 Y^i) - \rho\vec{U} \cdot \nabla_2 Y^i + S^i \tag{4}$$

Longitudinal Momentum:

$$\rho u u_{,x} = \nabla_2 \cdot (\mu \nabla_2 u) \qquad - \rho\vec{U} \cdot \nabla_2 u \quad - p_{,x} \tag{5}$$

Lateral Momentum:

$$\rho u w_{,x} = \nabla_2 \cdot (\mu \nabla_2 w) \qquad - \rho\vec{U} \cdot \nabla_2 w \quad - p_{,z} \tag{6}$$

determining the mixing resulting from various given injector configurations but, of equal importance, they provide the required accuracy comparison for theoretical analysis of the resultant turbulent flow fields. Concomitant with the establishment of appropriate models for turbulent mass and momentum transport coefficient distributions in three-dimensional flow fields will be the emergence of the capability to perform analytical studies for both detailed flow description and design optimization. The success of this approach depends upon establishment of a proven capability to model the three-dimensional viscous flow field equations numerically, and to generate computational solutions for practical geometrical configurations.

This numerical analysis capability is now operational within the COMOC general purpose computer program system. The theoretical foundation for COMOC is a finite element solution algorithm for a generalized initial-valued, quasi-linear elliptic boundary value partial differential equation, systems of which typically describe the mechanics and thermodynamics of continuum mechanical phenomena. Employing an extrapolation of two-dimensional mixing length/mass defect turbulent transport concepts, as a prototype three-dimensional turbulent transport model, an analytical study of mixing downstream of transverse hydrogen injection into a Mach 4, three-dimensional air boundary layer flow over a flat plate has been performed using COMOC. Detailed numerical prediction of the flow field is presented, in a solution domain spanning 30 to 120 injector diameters downstream, for the single jet geometry of Rogers (ref. 5), for a jet to freestream dynamic pressure ratio (q_r) of unity, an injection orifice diameter (D) equal to 0.102 cm (0.040 in.), stagnation freestream pressure of 13.6 atm (1 atm = 101.325 kN/m^2) and a stagnation temperature of 300°K. These conditions correspond to a Reynolds number per meter of 6.19×10^7; the boundary layer thickness at the injector longitudinal station was equal to 2.7 injector diameters. The results of computations for a multi-jet configuration, with injector separation equal to 12.5 injector diameters, are also presented, for the freestream conditions similar to the single-jet case.

Considerable experimental data management is required to establish initial conditions for numerical three-dimensional solutions. A candidate alternative method is computational replacement of the complex injection and turning phenomena with a "virtual source" of injectant imbedded within the air boundary layer flow. A theory is presented to establish the initial condition specification of a virtual source configuration based solely upon freestream and injectant parameters. Employing the same extrapolated turbulence model as before, analytical results are presented for propagation of the virtual source of hydrogen into the downstream mixing region, for a solution domain spanning 0 to 60 injector diameters downstream. The computational configuration is identical to the multi-jet geometry of Rogers, and results are established for the three dynamic pressure ratios of $q_r = 0.5$, 1.0, and 1.5. The agreement between computed and experimentally measured data is described in terms of decay of the maximum hydrogen concentration, trajectory of the maximum concentration, and lateral spreading of the diffusion pattern.

For all computational solutions, COMOC was adapted to compute the integral mixing efficiency parameter, η, of ref. 6. The potential usefulness of this scalar correlation parameter as a design optimization tool on a relative basis is discussed. Combustion data are required to establish an absolute comparison basis. Sample results are discussed illustrating how the COMOC predictive analysis capability can be expanded to compute the actual reacting flows of practical interest in combustor design and optimization.

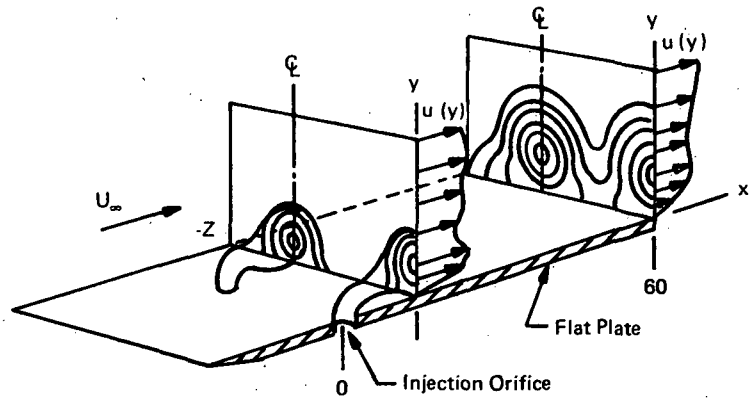

Figure 2. Three-Dimensional Flow Field for Mixing Downstream of Transverse Injection from Discrete Orifices

Energy:

$$\rho u H_{,x} = \nabla_2 \cdot \left(\frac{\mu}{Pr} \nabla_2 H\right) - \rho \vec{U} \cdot \nabla_2 H$$
$$- \nabla_2 \cdot \left[(1 - Pr) \frac{\mu}{2Pr} \nabla_2 (u^2 + w^2)\right]$$
$$- \nabla_2 \cdot \left[(1 - Le) \frac{\mu}{Pr} \sum_i h^i \nabla_2 Y^i\right] \qquad (7)$$

The variables appearing in equations (3) through (7) have their usual fluid mechanic interpretation: Y^i is the mass fraction of the i^{th} species, Pr is the Prandtl Number, and Le is the Lewis Number specified for essentially binary diffusion. The stagnation enthalpy H is defined as,

$$H \equiv \sum_i h^i Y^i + 1/2 (u^2 + w^2) \qquad (8)$$

and the static enthalpy of the i^{th} species is expressed in terms of temperature as,

$$h^i \equiv \int_0^T c_p^i \, dT \qquad (9)$$

Each species is assumed to behave as a perfect gas. From Dalton's law, the equation of state takes the form

$$p = \rho R T \sum_i \frac{Y^i}{W^i} \qquad (10)$$

where R is the universal gas constant, and W^i is the molecular weight of the i^{th} species.

Solution is required for the equation system (3) through (10), with appropriate specification of both boundary and initial conditions, as well as the pressure distribution, p (x,z), in the external inviscid flow field. The form selected for writing these equations purposefully illustrates the mathematical uniformity that pervades the system which is of considerable significance in establishing the (finite element) numerical solution algorithm.

FINITE ELEMENT SOLUTION ALGORITHM

Each of the partial differential equations (4) through (7), requiring solution for the three-dimensional mixing problem, is a special case of the general initial-valued, quasi-linear elliptic boundary value problem of mathematical physics. The global continuity equation (3) is purely initial value, and requires special consideration as detailed after the general development. For the numerical algorithm development, full advantage is taken of the mathematical uniformity pervading equations (4) through (7) by noting that each is a special case of the general equation, $L(q) \equiv 0$, or specifically,

$$\rho u q_{,x} = \nabla_2 \cdot (k \nabla_2 q) - \rho \vec{U} \cdot \nabla_2 q + f \tag{11}$$

In equation (11), q is a generalized dependent variable, k is the generalized diffusional transport coefficient, and f is any forcing function that may or may not be explicitly independent of q. Table 1 lists the functions k and f appropriate to q identified with each dependent variable.

TABLE 1
COEFFICIENTS IN GENERAL EQUATION

Equation Number	q	k	f
(4)	Y^i	$\frac{\mu Le}{Pr}$	S^i
(5)	u	μ	$-p_{,x}$
(6)	w	μ	$-p_{,z}$
(7)	H	$\frac{\mu}{Pr}$	$-\nabla_2 \cdot [(1 - Pr) \frac{\mu}{2Pr} \nabla_2 (u^2 + w^2)]$
			$-\nabla_2 \cdot [(1 - Le) \frac{\mu}{Pr} \sum_i h^i \nabla_2 Y^i]$

The initial conditions for solution of equations (4) through (7) comprise a specified distribution for each q at the initial longitudinal station, $x=x_o$, of the form

$$q(x_o,y,z) = Q_o(y,z) \tag{12}$$

All boundary conditions of practical importance, for the elliptic solution domain, can be written in the form

$$a_1(x) q(\bar{y},\bar{z}) + a_2(x) \nabla_2 q(\bar{y},\bar{z}) \cdot \hat{n} = a_3(x) \tag{13}$$

The superscript bar constrains the independent variable to lie on the closure, ∂R, of the elliptic domain R, and $\hat{n}$ is the outward pointing unit vector everywhere normal to the domain closure. Table 2 lists representative values of the a_i, equation (13), required to enforce sample boundary condition specifications for select dependent variables.

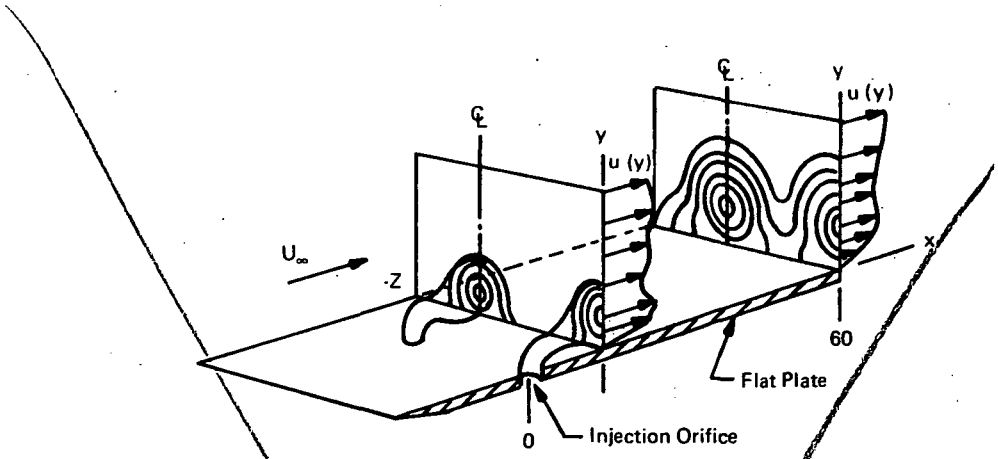

Figure 2. Three-Dimensional Flow Field for Mixing Downstream of Transverse Injection from Discrete Orifices

Energy:

$$\rho u H_{,x} = \nabla_2 \cdot \left(\frac{\mu}{Pr} \nabla_2 H\right) - \rho \vec{U} \cdot \nabla_2 H$$
$$- \nabla_2 \cdot \left[(1 - Pr) \frac{\mu}{2Pr} \nabla_2 (u^2 + w^2)\right]$$
$$- \nabla_2 \cdot \left[(1 - Le) \frac{\mu}{Pr} \Sigma h^i \nabla_2 Y^i\right] \qquad (7)$$

The variables appearing in equations (3) through (7) have their usual fluid mechanic interpretation: Y^i is the mass fraction of the i^{th} species, Pr is the Prandtl Number, and Le is the Lewis Number specified for essentially binary diffusion. The stagnation enthalpy H is defined as,

$$H \equiv \sum_i h^i Y^i + 1/2 (u^2 + w^2) \qquad (8)$$

and the static enthalpy of the i^{th} species is expressed in terms of temperature as,

$$h^i \equiv \int_0^T c_p^i \, dT \qquad (9)$$

Each species is assumed to behave as a perfect gas. From Dalton's law, the equation of state takes the form

$$p = \rho R T \sum_i \frac{Y^i}{W^i} \qquad (10)$$

where R is the universal gas constant, and W^i is the molecular weight of the i^{th} species.

Solution is required for the equation system (3) through (10), with appropriate specification of both boundary and initial conditions, as well as the pressure distribution, p (x,z), in the external inviscid flow field. The form selected for writing these equations purposefully illustrates the mathematical uniformity that pervades the system which is of considerable significance in establishing the (finite element) numerical solution algorithm.

TABLE 2
COEFFICIENTS IN GENERAL BOUNDARY CONDITION STATEMENT

Boundary Condition	Coefficients		
	a_1	a_2	a_3
No-Slip at Wall	1	0	0
Slip at Wall	†	-1	0
Mass Injection	0	1	†
Adiabatic Wall	0	1	0
Specified Heat Flux	0	1	†
Temperature Dependent Flux	†	†	†
Symmetry Condition	0	1	0

† Non-zero values, user specified to enforce desired conditions.

Solution of the differential equation system, equations (4) through (7) is thus reduced to establishment of a numerical solution algorithm for equations (11) through (13). The finite element method is suggested, as has been presented by Baker (ref. 9, 10). Briefly, solution is sought to equation (11) using Galerkin criteria within the Method of Weighted Residuals (MWR), see Finlayson and Scriven (ref. 11) by approximation of a (each) dependent variable within the solution domain, R, by a series expansion of the form.

$$q^*(\vec{x}) = \sum_{k=1} C_k(x)\,\phi_k(y,z) \tag{14}$$

In equation (14), the $C_k(x)$ are unknown expansion coefficients modifying members, $\phi_k(y,z)$, of a set of functions that are complete in the space of the elliptic domain. Certain of the expansion coefficients are evaluated by requiring that the approximate solution, equation (14), satisfies appropriate boundary conditions, equation (13). The remaining unknown coefficients are then determined by setting to zero the differential equation residuals, formed by substitution of q^* into equation (11), multiplication by a set of weighting functions, W_k, typically identical to the spatial approximation functions, ϕ_k, and integrating over the elliptic domain R. This produces the N ordinary differential equations.

$$\int_R W_k(\vec{x})\, L(q^*)\, d\tau \equiv 0 \quad k=1,2,\ldots,N \tag{15}$$

where N corresponds to the total number of remaining unknown coefficients in the definition of the approximation function, equation (14), and $L(q^*)$ is equation (11) written on the approximate solution.

When non-vanishing gradient boundary conditions exist, a generalization to MWR relaxes the constraints formed by the boundary condition statement. Form the N boundary residuals, defined from equation (13) as

$$\int_{\partial R} W_k(\vec{x})\left[q^* - \frac{1}{a_1}(a_3 - a_2 \nabla_2 q^* \cdot \hat{n}\right] d\sigma \equiv 0 \quad k=1,2,\ldots,N \tag{16}$$

Looking to the variational calculus for guidance, multiply equation (16) by a Lagrange multiplier, λ, and subtract the set from equation (15). Noting that the N weighting functions can be written as,

$$W_k(\vec{x}) = \frac{\partial q^*(\vec{x})}{\partial C_k(x)} \tag{17}$$

integrating by parts the differential equation term involving the elliptic operator, and identifying λa_2 with the generalized diffusional transport coefficient, k, Table 1, achieves a cancellation of terms. The resultant ordinary differential equation system for determination of the remaining unknown expansion coefficients, equation (14), is

$$-\int_R \nabla_2 \left(\frac{\partial q^*}{\partial C_k}\right) \cdot k \nabla_2 q^* \, d\tau - \int_R \frac{\partial q^*}{\partial C_k} \rho \vec{U}^* \cdot \nabla_2 q^* \, d\tau$$

$$+ \int_\theta \frac{\partial q^*}{\partial C_k} f^* \, d\tau - \int_R \frac{\partial q^*}{\partial C_k} \rho u^* q^*_{,x} \, d\tau + \int_{\partial R} \frac{\partial q^*}{\partial C_k} a_3 \, d\sigma$$

$$- \int_{\partial R} \frac{\partial q^*}{\partial C_k} a_1 \, q^* \, d\sigma = 0 \tag{18}$$

Throughout equation (18), the superscript star notation implies an approximation to the function and/or parameter, consistant with equation (11).

Application of these concepts on a local basis may be termed Numerical Method of Weighted Residuals. Establishment of an assembly procedure for generation of the global algorithm provides the theoretical basis for a finite element numerical solution algorithm. Since equation (11) is valid at a point, it is similarly valid in arbitrary subdomains, R_m, of R with closures ∂R_m. In actuality, for fluid mechanics, the integral formulation transforming system behavior to a subdomain (control volume) can be viewed as fundamental, the more familiar differential equations having been derived therefrom. Hence, in each of M, disjoint interior subdomains, R_m, defined by $(y,z,x) \epsilon R_m x [x_o, \infty)$, and where $UR_m = R$, define a local approximation function

$$q^*_m(\vec{x}) \equiv \sum_k^N C_{mk}(x) \, \phi_k(y,z) \tag{19}$$

where the subscript, m, constrains the domain of equation (19) to R_m. Evaluate equation (18) within each R_m, so selected that $k_m(\vec{x})$ is adequately represented by a local value $k_m(x)$ within R_m. This yields an ordinary differential equation system for solution of the local approximation function, equation (19), within R_m. The global solution algorithm is established employing Boolean algebra to assemble the MxN equations (18) into an equation system which enforces weighted average global adherence to the original differential equation system, equations (11) through (13).

The globally assembled equation system is similarly a first order, ordinary differential equation system, written on the totality of local expansion coefficients, $C_{mk}(x)$, equation (19), that do not coincide with locations on the global closure, ∂R, where fixed boundary conditions are applied,

TABLE 2
COEFFICIENTS IN GENERAL BOUNDARY CONDITION STATEMENT

Boundary Condition	Coefficients		
	a_1	a_2	a_3
No-Slip at Wall	1	0	0
Slip at Wall	†	-1	0
Mass Injection	0	1	†
Adiabatic Wall	0	1	0
Specified Heat Flux	0	1	†
Temperature Dependent Flux	†	†	†
Symmetry Condition	0	1	0

† Non-zero values, user specified to enforce desired conditions.

Solution of the differential equation system, equations (4) through (7) is thus reduced to establishment of a numerical solution algorithm for equations (11) through (13). The finite element method is suggested, as has been presented by Baker (ref. 9, 10). Briefly, solution is sought to equation (11) using Galerkin criteria within the Method of Weighted Residuals (MWR), see Finlayson and Scriven (ref. 11) by approximation of a (each) dependent variable within the solution domain, R, by a series expansion of the form.

$$q^*(\vec{x}) = \sum_{k=1} C_k(x)\,\phi_k(y,z) \tag{14}$$

In equation (14), the $C_k(x)$ are unknown expansion coefficients modifying members, $\phi_k(y,z)$, of a set of functions that are complete in the space of the elliptic domain. Certain of the expansion coefficients are evaluated by requiring that the approximate solution, equation (14), satisfies appropriate boundary conditions, equation (13). The remaining unknown coefficients are then determined by setting to zero the differential equation residuals, formed by substitution of q^* into equation (11), multiplication by a set of weighting functions, W_k, typically identical to the spatial approximation functions, ϕ_k, and integrating over the elliptic domain R. This produces the N ordinary differential equations.

$$\int_R W_k(\vec{x})\,L(q^*)\,d\tau \equiv 0 \quad k=1,2,\ldots,N \tag{15}$$

where N corresponds to the total number of remaining unknown coefficients in the definition of the approximation function, equation (14), and $L(q^*)$ is equation (11) written on the approximate solution.

When non-vanishing gradient boundary conditions exist, a generalization to MWR relaxes the constraints formed by the boundary condition statement. Form the N boundary residuals, defined from equation (13) as

$$\int_{\partial R} W_k(\vec{x})\left[q^* - \frac{1}{a_1}(a_3 - a_2\,\nabla_2 q^*\cdot\hat{n}\right]d\sigma \equiv 0 \quad k=1,2,\ldots,N \tag{16}$$

i.e., $a_2=0$, equation (13). The order of this equation system is less than MxN by both connectivity of the subdomains and enforcement of fixed boundary conditions.

The last step to establishment of the finite element solution algorithm is selection of the functionals $\phi_k(y,z)$, equation (19), and specification of the finite element subdomain geometry. From the vast choice which exists, experience with general purpose computer codes indicates that many practical problems are amenable to solution using linear functionals. The natural two-dimensional finite element shape, illustrated in figure 3, is a triangle with (at least) vertex node points. Equation (19) constrained to a linear representation over the triangular shaped finite element domain, where $\{\ \}$ denotes a column matrix, becomes

$$q_m^*(\vec{x}) = C_{1m}(x) + C_{2m}(x)\,y + C_{3m}(x)\,z \equiv \{C(x)\}_m^T \{x\} \tag{20}$$

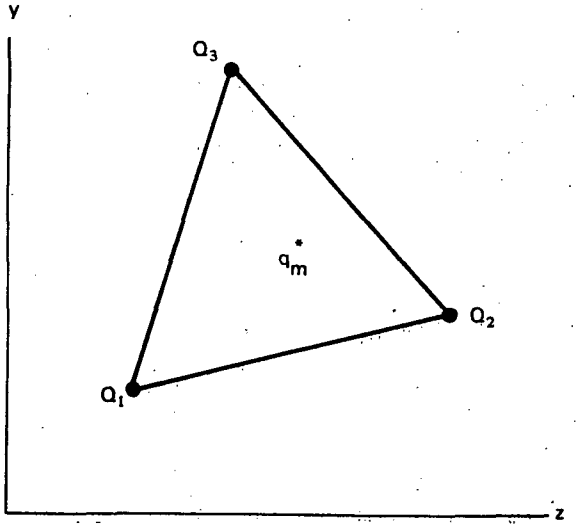

Figure 3. Triangular Finite Element

Evaluating equation (20), at the three vertex nodes of the finite element, produces a linear algebraic equation system which can be solved analytically for matrix elements of $\{C(x)\}_m$. Hence, an alternate and useful expression for q_m^* is

$$q_m^*(x,y,z) = \{x\}^T [\Gamma]_m \{Q(x)\}_m \tag{21}$$

The elements of the 3x3 coefficient matrix, $[\Gamma]_m$, are known constants, derived strictly from geometrical considerations, as

$$[\Gamma]_m = \frac{1}{2A_m} \begin{bmatrix} \alpha_i & \alpha_j & \alpha_k \\ \beta_i & \beta_j & \beta_k \\ \gamma_i & \gamma_j & \gamma_k \end{bmatrix} \tag{22}$$

where

$$\alpha_p = y_q z_r - y_r z_q$$

$$\beta_p = z_q - z_r \tag{23}$$

$$\gamma_p = y_r - y_q$$

and the indices (p,q,r) permute cyclicly in the order (i,j,k). The elements of $\{x\}$ are $\{1,y,z\}$, and the three elements of $\{Q(x)\}_m$ are the local values of the dependent variable, q^*_m, at each node point location of the finite element. In equation (22), A_m is the plane area of the finite element.

The establishment of equation (21) allows direct evaluation of terms within the finite element algorithm, which is equation (18) constrained to the subdomain R_m. The weighting functions for Galerkin criteria are now expressible as

$$\frac{\partial q^*_m}{\partial C_{mk}} = \frac{\partial q^*_m}{\partial \{Q(x)\}_m} = [\Gamma]^T_m \{x\} \tag{24}$$

Substituting equations (21) and (24) into equation (18), the solution algorithm for the typical initial-boundary value differential equation system for the three-dimensional flow field becomes

$$[C]_m \{Q\}'_m = -\sum_{I=1} [KI]_m \{Q\}_m + \sum_{I=1} \{LI\}_m \tag{25}$$

In equation (25), the superscript prime denotes the ordinary derivative with respect to the x coordinate. The indicated finite element matrices, common to all q, are

$$[C]_m \equiv [\Gamma]^T_m \int_{R_m} \{x\}\{x\}^T [\Gamma]_m \{\rho U\}_m \{x\}^T d\tau [\Gamma]_m$$

$$[K1]_m \equiv [\Gamma]^T_m \int_{R_m} \nabla_2 \{x\} \cdot k_m \nabla_2 \{x\}^T d\tau [\Gamma]_m$$

$$[K2]_m \equiv [\Gamma]^T_m \int_{R_m} \{x\}\{x\}^T [\Gamma]_m \left(\{\rho V\}_m \hat{j} + \{\rho W\}_m \hat{k} \right) \cdot \nabla_2 \{x\}^T d\tau [\Gamma]_m$$

$$[K3]_m \equiv [\Gamma]^T_m \int_{\partial R_m} \{x\} a_{ml} \{x\}^T d\sigma [\Gamma]_m$$

$$\{L1\}_m \equiv [\Gamma]^T_m \int_{\partial R_m} \{x\} a_{m3} d\sigma \tag{26}$$

i.e., $a_2 = 0$, equation (13). The order of this equation system is less than MxN by both connectivity of the subdomains and enforcement of fixed boundary conditions.

The last step to establishment of the finite element solution algorithm is selection of the functionals $\phi_k(y,z)$, equation (19), and specification of the finite element subdomain geometry. From the vast choice which exists, experience with general purpose computer codes indicates that many practical problems are amenable to solution using linear functionals. The natural two-dimensional finite element shape, illustrated in figure 3, is a triangle with (at least) vertex node points. Equation (19) constrained to a linear representation over the triangular shaped finite element domain, where $\{\ \}$ denotes a column matrix, becomes

$$q_m^*(x) = C_{1m}(x) + C_{2m}(x)\, y + C_{3m}(x)\, z \equiv \{C(x)\}_m^T \{x\} \tag{20}$$

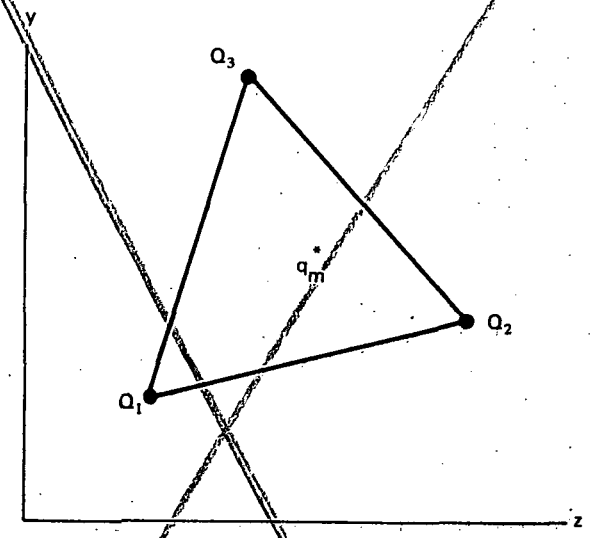

Figure 3. Triangular Finite Element

Evaluating equation (20), at the three vertex nodes of the finite element, produces a linear algebraic equation system which can be solved analytically for matrix elements of $\{C(x)\}_m$. Hence, an alternate and useful expression for q_m^* is

$$q_m^*(x,y,z) = \{x\}^T [\Gamma]_m \{Q(x)\}_m \tag{21}$$

The elements of the 3x3 coefficient matrix, $[\Gamma]_m$, are known constants, derived strictly from geometrical considerations, as

$$[\Gamma]_m = \frac{1}{2A_m} \begin{bmatrix} \alpha_i & \alpha_j & \alpha_k \\ \beta_i & \beta_j & \beta_k \\ \gamma_i & \gamma_j & \gamma_k \end{bmatrix} \tag{22}$$

The source term finite element matrices, for each particular identification of q, are

$$q = Y^i: \{L2\}_m \equiv [\Gamma]_m^T \int_{R_m} \{x\} S^i \, d\tau$$

$$q = u: \{L2\}_m \equiv -[\Gamma]_m^T \int_{R_m} \{x\} p_{,x} \, d\tau$$

$$q = w: \{L2\}_m \equiv -[\Gamma]_m^T \int_{R_m} \{x\} p_{,z} \, d\tau$$

$$q = H: \{L2\}_m \equiv [\Gamma]_m^T \int_{R_m} \{x\} \nabla_2 \cdot (1-Pr) \frac{\mu}{Pr} \Big(\{U\}_m^T [\Gamma]_m^T \{x\} \nabla_2 \{x\}^T [\Gamma]_m \{U\}_m + \{W\}_m^T [\Gamma]_m^T \{x\} \nabla_2 \{x\}^T [\Gamma]_m \{W\}_m \Big) \, d\tau$$

$$\{L3\}_m \equiv [\Gamma]_m^T \int_{R_m} \{x\} \nabla_2 \cdot (1-Le) \frac{\mu}{Pr} \Sigma_i \{h^i\}_m^T [\Gamma]_m^T \{x\} \nabla_2 \{x\}^T [\Gamma]_m \{Y^i\}_m \, d\tau \qquad (27)$$

In equation (27), the pressure gradients are assumed specified functions of x and z, and the matrix elements of $\{h^i\}_m$ are the static enthalpy at nodes of R_m, as defined by equations (8) and (9).

Equations (25) through (27) define the finite element solution algorithm for the typical equation over each finite element. The MxN equations (25) are assembled, using Boolean algebra, into the global system which enforces a weighted average adherence to the original partial differential equation. The appearance of the global equation is identical to equation (25) with the subscripts m removed. This equation system is eligible for integration, as a system of ordinary differential equations, written on the global column matrix, $\{Q(x)\}$, by any algorithm. The choice between implicit or explicit essentially reduces to whether or not elements of the [C] matrix, and the $\{Q(x)\}$ vector on the right side of equation (25), are evaluated at the current or the next advanced x station.

An explicit algorithm, (ref. 12), has been used to generate the reported results. For this choice, the elements of the $\{Q(x)\}$ vector are ordered such that those nodes occurring on ∂R, where fixed boundary conditions are applied, are loaded into the bottom partition of $\{Q(x)\}$. The symmetric [C] matrix is partitioned, correspondingly, and the rank (r) of the upper partition equals the number of unknowns in the $\{Q(x)\}$ vector. The lower partition is contracted with the corresponding known (fixed) elements of $\{Q(x)\}$, and subtracted from both sides of equation (25). Premultiplying equation (25) by the inverse of the reduced [C] matrix yields, as the final global solution form for the finite element algorithm, the explicit equation.

$$\{Q\}'_r = [C]_r^{-1} \left(\Sigma_I [KI]_r \{Q\}_r + \Sigma_I \{LI\}_r \right) \qquad (28)$$

The subscripts r in equation (28) indicate that the system is of the reduced rank r, and the contributions stemming from the lower partition operations have been lumped into an additional

$\{LI\}$ vector. The solution of equation (28) yields the values of the dependent variable approximation function q^*, equation (14), at the nodes of the finite element discretization of the solution domain R, including those values at nodes existing on ∂R where gradient boundary conditions have been enforced.

The finite element solution algorithm for global continuity follows a similar development. Equation (3) is strictly initial value on ρv, as a function of y, with x and z appearing as parameters in the form of the corresponding derivatives. Hence, the finite element approximation q^*_m, equation (21), need span only the transverse coordinate direction, as

$$q^*_m = \{1, y, y^2, \ldots, y^n\}^T [\Gamma]_m \{Q(x,z)\}_m \tag{29}$$

and the elements of $\{Q(x,z)\}_m$ are corresponding values (and derivatives) of ρv at nodes of the discretization. These nodal values are functions of both x and z; it is thus required to solve global continuity at successive z locations, for each x station.

The solution of equation (3) by MWR follows the conventional procedure. Identifying the approximation function, q^*_m for the terms in the equation, and selecting a set of weighting functions, W_k, form the weighted residual of equation (3), and integrate over the finite element domain, R_m. This yields

$$\int_{y_o}^{y_1} W_k(y)\, L(q^*_m)\, dy \equiv 0 \qquad k = 1, 2, \ldots, N \tag{30}$$

which is solvable on a subdomain (finite element) basis, since equation (3) is an initial value problem.

Concerning the formation of particular components of equation (30), since the finite element approximation spans the x plane, $(\rho w)_{,z}$ is known from equation (21) written on ρw. However, $(\rho u)_{,x}$ is not available, since this coordinate direction is spanned by finite difference integration. Actually, no streamwise derivatives, equations (3) through (7), are available until the flow field is there known. Since ρv is required to evaluate these derivatives, an estimation is required of the $(n+1)^{st}$ value of $(\rho u)_{,x}$. In keeping with the use of first order accurate methods, and realizing that the required variable is, in the discretized solution, actually equal to $(\rho U)'$ a first-order accurate finite difference approximation formula is adequate, and is of the form

$$(\rho U)'_{n+1} \approx \frac{2}{x_{n+1}-x_n} [(\rho U)_{n+1} - (\rho U)_n] - (\rho U)'_n(\xi) \tag{31}$$

The truncation error in equation (31) equals $0.1667\, h^2\, (\rho U)'''(\xi)$, where h is the x direction step size, and $x_n \leqslant \xi \leqslant x_{n+1}$.

The source term finite element matrices, for each particular identification of q, are

$$q = Y^i: \{L2\}_m \equiv [\Gamma]_m^T \int_{R_m} \{x\} S^i \, d\tau$$

$$q = u: \{L2\}_m \equiv -[\Gamma]_m^T \int_{R_m} \{x\} p_{,x} \, d\tau$$

$$q = w: \{L2\}_m \equiv -[\Gamma]_m^T \int_{R_m} \{x\} p_{,z} \, d\tau$$

$$q = H: \{L2\}_m \equiv [\Gamma]_m^T \int_{R_m} \{x\} \nabla_2 \cdot (1-Pr) \frac{\mu}{Pr} \Big(\{U\}_m^T [\Gamma]_m^T \{x\} \nabla_2 \{x\}^T [\Gamma]_m \{U\}_m + \{W\}_m^T [\Gamma]_m^T \{x\} \nabla_2 \{x\}^T [\Gamma]_m \{W\}_m \Big) \, d\tau$$

$$\{L3\}_m \equiv [\Gamma]_m^T \int_{R_m} \{x\} \nabla_2 \cdot (1-Le) \frac{\mu}{Pr} \sum_i \{h^i\}_m^T [\Gamma]_m^T \{x\} \nabla_2 \{x\}^T [\Gamma]_m \{Y^i\}_m \, d\tau \qquad (27)$$

In equation (27), the pressure gradients are assumed specified functions of x and z, and the matrix elements of $\{h^i\}_m$ are the static enthalpy at nodes of R_m, as defined by equations (8) and (9).

Equations (25) through (27) define the finite element solution algorithm for the typical equation over each finite element. The MxN equations (25) are assembled, using Boolean algebra, into the global system which enforces a weighted average adherence to the original partial differential equation. The appearance of the global equation is identical to equation (25) with the subscripts m removed. This equation system is eligible for integration, as a system of ordinary differential equations, written on the global column matrix, $\{Q(x)\}$, by any algorithm. The choice between implicit or explicit essentially reduces to whether or not elements of the [C] matrix, and the $\{Q(x)\}$ vector on the right side of equation (25), are evaluated at the current or the next advanced x station.

An explicit algorithm, (ref. 12), has been used to generate the reported results. For this choice, the elements of the $\{Q(x)\}$ vector are ordered such that those nodes occurring on ∂R, where fixed boundary conditions are applied, are loaded into the bottom partition of $\{Q(x)\}$. The symmetric [C] matrix is partitioned, correspondingly, and the rank (r) of the upper partition equals the number of unknowns in the $\{Q(x)\}$ vector. The lower partition is contracted with the corresponding known (fixed) elements of $\{Q(x)\}$, and subtracted from both sides of equation (25). Premultiplying equation (25) by the inverse of the reduced [C] matrix yields, as the final global solution form for the finite element algorithm, the explicit equation.

$$\{Q\}'_r = [C]_r^{-1} \left(\sum_I [KI]_r \{Q\}_r + \sum_I \{LI\}_r \right) \qquad (28)$$

The subscripts r in equation (28) indicate that the system is of the reduced rank r, and the contributions stemming from the lower partition operations have been lumped into an additional

COMOC COMPUTER PROGRAM

The COMOC (Computational Continuum Mechanics) general purpose finite element computer program system is coded entirely in terms of generalized non-dimensional independent and dependent variables. In addition to producing the results to be discussed, it has been exercised for problems in transient heat conduction (ref. 13) and the two-dimensional Navier-Stokes equations (ref. 9, 14, and 15).

The program consists of four basic Modules, as illustrated in figure 4. In the INPUT Module, the desired discretization is formed by specification of the plane coordinates (y_k, z_k) of the triad of vertex nodes for each finite element. The node numbering sequence is completely arbitrary, as is the selection of a particular discretization, and both may be chosen for output convenience. In particular, nodes are first placed where output information is desired. The remainder of the solution domain is then discretized to avoid finite elements with aspect ratios greater than about 100:1. The closure of the solution domain is recognized as the counterclockwise connection of the first N nodes, with N an input parameter. These node numbers are then automatically loaded into the bottom partition of the global unknown vectors, $\{Q(x)\}$.

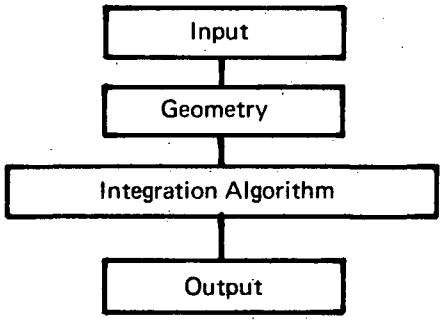

Figure 4. COMOC Computer Program Organization

The appropriate non-vanishing element boundary condition coefficients a_{mi}, equation (13), are included as element information for each dependent variable to be solved, since in general the different Q's have individual specifications. The input phase is completed by reading non-dimensionalizing factors, various control parameters, information regarding initial conditions for the dependent variable vectors, $\{Q(x_o)\}$, and the desired output control parameters.

The next two Modules, figure 4, are basically DO loops on the finite elements of the discretization. In the GEOMETRY Module, the element coefficient matrix, $[\Gamma]_m$, is formed. Sequential passes through two subroutines generate and assemble the required moment distributions over areas and lines, and establish the various required finite element matrices, equations (26) and (27).

The INTEGRATION Module embodies the finite difference integration algorithm for the system of ordinary differential equations. The basic element operation is formation of equation (25) at a given x station, and the assembly of the element matrices into the global representation, equation (28). In this procedure, the required order of equation (28) is automatically determined, and the matrix $[C]_r^{-1}$ obtained. At user-selected points, the OUTPUT Module is called to record the arrays within the dependent variable vectors $\{Q(x)\}$ and other desired parameters.

The integration algorithm presently used by COMOC is an explicit, single-step, multi-stage finite difference procedure with a large region of absolute stability (ref. 12). Since it is single-step, the changing of step-size during solution is easily accomplished. The algorithm automatically adjusts current step-size by comparison of a truncation error coefficient to a user-specified parameter related to an allowable local error magnitude. An extensive discussion on the operation of this algorithm is presented by Baker and Manhardt (ref. 13).

RESULTS AND DISCUSSION

The Mechanics and Thermodynamics of Binary, Isoenergetic Turbulent Boundary Layer Mixing

A considerable simplification to the general equation system, equations (3) through (7), can be achieved for analysis of the specific problem of interest, namely two-component, non-reacting cold flow mixing of hydrogen injected into a turbulent supersonic air boundary layer flow on a flat plate (ref. 5 and 6). Pressure gradients in the external flow field are negligible and only one species continuity equation is required. As a first approximation, the flow may be assumed isoenegetic, and the species continuity and energy differential equation descriptions are identical. Hence, their respective solutions can be linearly related as

$$\frac{H-H_\infty}{H_0-H_\infty} = K\left[\frac{Y-Y_\infty}{Y_0-Y_\infty}\right] \tag{32}$$

In equation (32), subscript zero denotes reference conditions at the point of injection, while subscript infinity refers to free stream reference values. For the specific case, Y_∞ vanishes and Y_0 equals unity. The mixture specific heat is a linear function of mass fraction; for this problem, the specific heat is temperature independent to within about ± 5%, in the range 100-300°K. This variation was assumed negligible, and direct solution of equation (32) for static temperature of the mixture at any point in the solution domain is

$$T_s(\vec{x}) = \frac{T_{o_a} + Y\,(rT_{o_h} - T_{o_a}) - \frac{1}{2gJ}\frac{U^2}{c_{p_a}}}{1+Y\,(r-1)} \tag{33}$$

Equation (33) is written on directly measurable reference values of air and hydrogen stagnation temperature at injection (T_{o_a} and T_{o_h}), and the computed local values of longitudinal velocity component (U) and hydrogen mass fraction (Y). The parameters g and J have their usual interpretation, c_{p_a} is the specific heat of air, and r is the (constant) ratio of specific heat of hydrogen to air at the air stagnation temperature. This assumption can be readily replaced by finite element solution of the energy equation (7), with temperature dependent thermophysical problems, for other problems, e.g., reacting flows.

The equation of state of the two-component mixture, equation (10), is readily reduced to the following expression for density, ρ, at any point in the solution domain assuming a constant static pressure distribution.

$$\rho(\vec{x}) = \frac{\rho_\infty T_{s_\infty}}{T_s\,[1+Y\,(m-1)]} \tag{34}$$

COMOC COMPUTER PROGRAM

The COMOC (Computational Continuum Mechanics) general purpose finite element computer program system is coded entirely in terms of generalized non-dimensional independent and dependent variables. In addition to producing the results to be discussed, it has been exercised for problems in transient heat conduction (ref. 13) and the two-dimensional Navier-Stokes equations (ref. 9, 14, and 15).

The program consists of four basic Modules, as illustrated in figure 4. In the INPUT Module, the desired discretization is formed by specification of the plane coordinates (y_k, z_k) of the triad of vertex nodes for each finite element. The node numbering sequence is completely arbitrary, as is the selection of a particular discretization, and both may be chosen for output convenience. In particular, nodes are first placed where output information is desired. The remainder of the solution domain is then discretized to avoid finite elements with aspect ratios greater than about 100:1. The closure of the solution domain is recognized as the counterclockwise connection of the first N nodes, with N an input parameter. These node numbers are then automatically loaded into the bottom partition of the global unknown vectors, $\{Q(x)\}$.

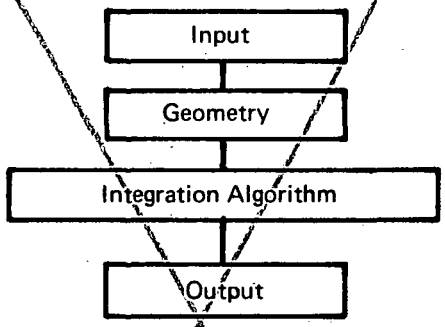

Figure 4. COMOC Computer Program Organization

The appropriate non-vanishing element boundary condition coefficients a_{mi}, equation (13), are included as element information for each dependent variable to be solved, since in general the different Q's have individual specifications. The input phase is completed by reading non-dimensionalizing factors, various control parameters, information regarding initial conditions for the dependent variable vectors, $\{Q(x_o)\}$, and the desired output control parameters.

The next two Modules, figure 4, are basically DO loops on the finite elements of the discretization. In the GEOMETRY Module, the element coefficient matrix, $[\Gamma]_m$, is formed. Sequential passes through two subroutines generate and assemble the required moment distributions over areas and lines, and establish the various required finite element matrices, equations (26) and (27).

The INTEGRATION Module embodies the finite difference integration algorithm for the system of ordinary differential equations. The basic element operation is formation of equation (25) at a given x station, and the assembly of the element matrices into the global representation, equation (28). In this procedure, the required order of equation (28) is automatically determined, and the matrix $[C]_r^{-1}$ obtained. At user-selected points, the OUTPUT Module is called to record the arrays within the dependent variable vectors $\{Q(x)\}$ and other desired parameters.

In equation (34), T_{s_∞} is the freestream (air) static temperature, T_s comes from equation (33), and m is the ratio of air to hydrogen molecular weights.

Finally, for the present problem of flow over a flat plate, w vanishes both at the wall and in the freestream, as well as along the symmetry plane bisecting the injection orifice and parallel to the predominant flow vector. A non-vanishing component may well exist on the remaining segment of the elliptic domain closure. However, since no experimental measurements are available, no plausible alternative exists but to assume w vanishes over the entire closure. The resultant solution to equation (6) is that w vanishes everywhere.

Therefore, the partial differential equation system requiring solution for the subject cold flow binary mixing problem reduces to equations (3) through (5), less the respective source terms, in combination with equations (33) and (34). The theory for turbulent transport of mass and momentum is described in the next section, and the procedure for computation of molecular viscosity for the binary mixture is described in Appendix C.

Model for Turbulent Transport Coefficient Distribution

To date, no work is reported on the modeling of three-dimensional boundary layer flows for the conditions of interest in this investigation (ref. 5, 6). For example, only the incompressible case has been analytically modeled, e.g., Bradshaw (ref. 16), Nash (ref. 17, 18). Therefore, the most direct approach was to develop a prototype three-dimensional model by extending techniques proven successful for planar and axisymmetric flows.

The three dimensional model developed herein reflects, (1) mass flux differences between the main flow and the jet, and (2) the turbulence due to the presence of the wall. Above the jet region, i.e., the region bounded by the wall and the zero concentration contour, (fig. 5) of the concentration profile, mixing is due to the differences in mass flux. Outside the jet and near the wall (large values of $|z|$), the turbulence is due solely to boundary layer phenomena. Within the region of the jet both mechanisms are active.

Shown in figure 6 is an axisymmetric flow configuration which was studied for turbulent transport characterization by Morgenthaler (ref. 19), and is being further studied.* The two flow geometries (figs. 5 and 6) are similar in that they each consider the normal sonic injection of hydrogen into a supersonic air (or nitrogen) stream. Two important differences are three-dimensional versus axisymmetric flow, and that pressure gradients may exert influence on the ducted axisymmetric flow field development. Calculations have since shown that neglecting pressure gradient in the ducted flow case does not significantly affect the predicted hydrogen concentration field. Therefore, the primary difference between the flows shown in figures 5 and 6 is the dimensionality.

Development of the prototype three-dimensional mixing model employed the results of analysis for the axisymmetric configuration. For this flow detailed experimental data were available from which distributions of eddy diffusivity coefficients were calculated using methods reported in reference 19. The objective was to determine whether the determined eddy diffusivity could be modeled using the mass defect concept and mixing length theory; i.e., techniques proven successful in modeling planar boundary layers (ref. 20) and axisymmetric free shear layers (ref. 21, 22).

*Zelazny, S.W.: Modeling of the Eddy Diffusivity of Mass in Supersonic, Axisymmetric, Ducted, Turbulent Flow, IOM 665:72:0320-1:SWZ, Mar. 1972, Bell Aerospace Co., Buffalo, N. Y.

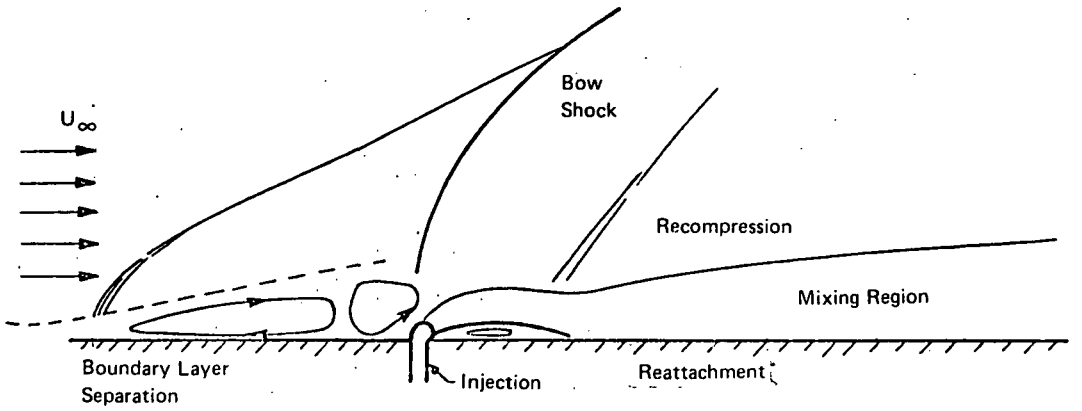

a) Side View

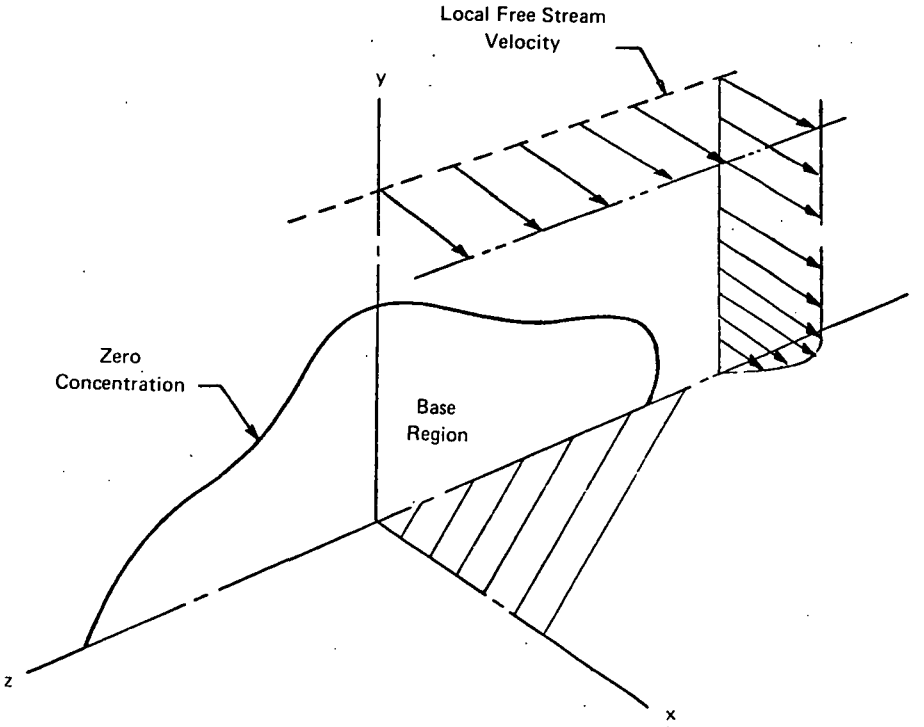

b) Cross Section of Mixing Region

Figure 5. Structure of Three-Dimensional Flow Field and Mixing Region

The mixing region is divided into an inner and outer sub-region as shown in figure 7. In the inner region, mixing length theory is assumed valid; hence, the eddy diffusivity is of the form

$$E_{D_{in}} = \ell^2 \omega \gamma \left|\frac{\partial U}{\partial y}\right| Sc_T^{-1} \quad o < y < y_d \tag{35}$$

where y is displacement from the wall, y_d is height of inner region (defined as that value of y where $E_{D_{in}} > E_{D_{out}}$), U is the mean axial velocity, and ℓ is the mixing length, given by

$$\ell = cy \tag{36}$$

In equation (34), T_{s_∞} is the freestream (air) static temperature, T_s comes from equation (33), and m is the ratio of air to hydrogen molecular weights.

Finally, for the present problem of flow over a flat plate, w vanishes both at the wall and in the freestream, as well as along the symmetry plane bisecting the injection orifice and parallel to the predominant flow vector. A non-vanishing component may well exist on the remaining segment of the elliptic domain closure. However, since no experimental measurements are available, no plausible alternative exists but to assume w vanishes over the entire closure. The resultant solution to equation (6) is that w vanishes everywhere.

Therefore, the partial differential equation system requiring solution for the subject cold flow binary mixing problem reduces to equations (3) through (5), less the respective source terms, in combination with equations (33) and (34). The theory for turbulent transport of mass and momentum is described in the next section, and the procedure for computation of molecular viscosity for the binary mixture is described in Appendix C.

Model for Turbulent Transport Coefficient Distribution

To date, no work is reported on the modeling of three-dimensional boundary layer flows for the conditions of interest in this investigation (ref. 5, 6). For example, only the incompressible case has been analytically modeled, e.g., Bradshaw (ref. 16), Nash (ref. 17, 18). Therefore, the most direct approach was to develop a prototype three-dimensional model by extending techniques proven successful for planar and axisymmetric flows.

The three dimensional model developed herein reflects, (1) mass flux differences between the main flow and the jet, and (2) the turbulence due to the presence of the wall. Above the jet region, i.e., the region bounded by the wall and the zero concentration contour, (fig. 5) of the concentration profile, mixing is due to the differences in mass flux. Outside the jet and near the wall (large values of $|z|$), the turbulence is due solely to boundary layer phenomena. Within the region of the jet both mechanisms are active.

Shown in figure 6 is an axisymmetric flow configuration which was studied for turbulent transport characterization by Morgenthaler (ref. 19), and is being further studied.* The two flow geometries (figs. 5 and 6) are similar in that they each consider the normal sonic injection of hydrogen into a supersonic air (or nitrogen) stream. Two important differences are three-dimensional versus axisymmetric flow, and that pressure gradients may exert influence on the ducted axisymmetric flow field development. Calculations have since shown that neglecting pressure gradient in the ducted flow case does not significantly affect the predicted hydrogen concentration field. Therefore, the primary difference between the flows shown in figures 5 and 6 is the dimensionality.

Development of the prototype three-dimensional mixing model employed the results of analysis for the axisymmetric configuration. For this flow detailed experimental data were available from which distributions of eddy diffusivity coefficients were calculated using methods reported in reference 19. The objective was to determine whether the determined eddy diffusivity could be modeled using the mass defect concept and mixing length theory; i.e., techniques proven successful in modeling planar boundary layers (ref. 20) and axisymmetric free shear layers (ref. 21, 22).

*Zelazny, S.W.: Modeling of the Eddy Diffusivity of Mass in Supersonic, Axisymmetric, Ducted, Turbulent Flow, IOM 665:72:0320-1:SWZ, Mar. 1972, Bell Aerospace Co., Buffalo, N. Y.

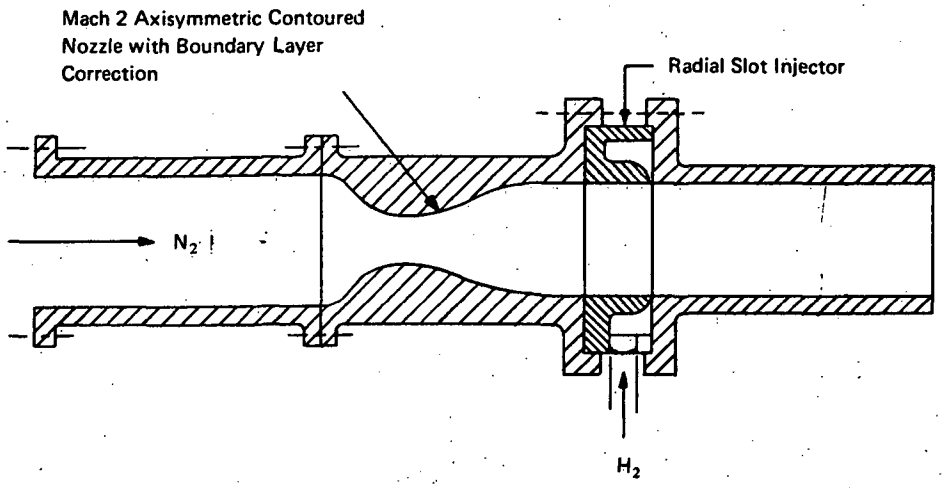

Figure 6. Schematic of Axisymmetric Ducted Supersonic Mixing Experimental Apparatus

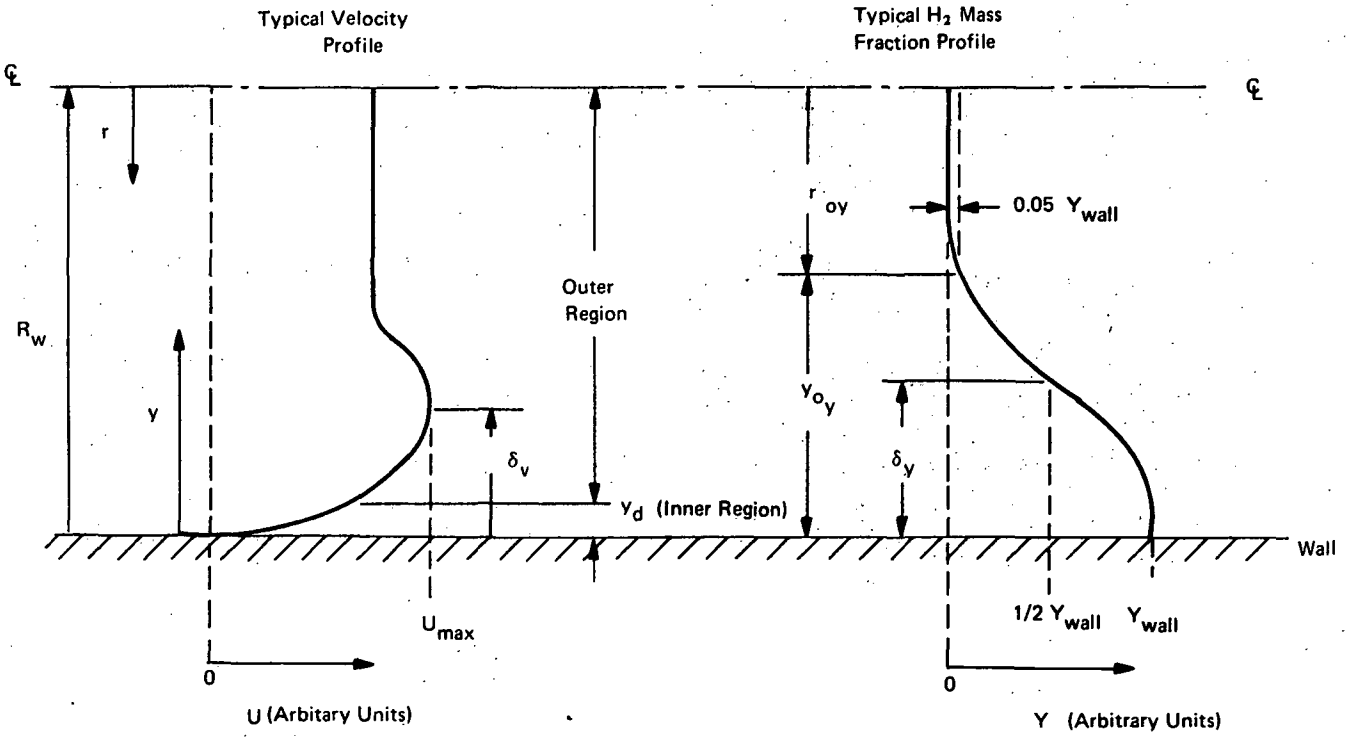

Figure 7 Typical Velocity and Mass Fraction Profiles Downstream of Sonic Injection of H_2 from a Circumferential Wall Slot (See Fig. 6)

The constant c, equation (36), has been found from boundary layer data to be equal to 0.4, whereas the turbulent Schmidt number was assumed equal to 0.7, consistent with both boundary layer and free shear layer data.

von Driest's (ref. 23) damping factor, ω, requires the eddy diffusivity to vanish at the wall, and is given by

$$\omega = (1 - e^{-y/A})^2 \tag{37}$$

where A is an empirically determined length scale expressed in terms of the wall values of shear stress τ_w and density ρ_w.

$$A = 26\nu/\sqrt{\tau_w/\rho_w} \tag{38}$$

The intermittency factor, γ, has been empirically modeled in a number of ways (ref. 24). In this study, it was found that

$$\gamma = \frac{1}{1+.01\zeta^9} \tag{39}$$

gave a fair representation of the data where $\zeta = y/\delta_y$, and δ_y is the value of y where the hydrogen mass fraction is one-half its wall value.

In the outer region, the eddy diffusivity of mass is assumed directly proportional to the mass defect (or excess) of the concentration layer and inversely proportional to the width of the concentration layer; hence

$$\rho E_{D_{out}} \approx \int_{r_{oy}}^{R_w} |\rho U - \rho_c U_c| \, dr/L \tag{40}$$

where R_w is the wall radius, r_{oy} is the distance from the centerline to the point where Y equals 0.05 Y_{WALL}, ρ_c is the density on the centerline, U_c is the axial velocity on the centerline, Y is the mass fraction of hydrogen, and Y_{WALL} is the mass fraction of hydrogen at the wall. Also,

$$L = R_w - r_{oy} \tag{41}$$

Accounting for intermittency at the outer region, the complete expression for E_D is given by

$$E_D = K\gamma \frac{\int_{r_{oy}}^{R_w} |\rho U - \rho_c U_c| \, dr}{\rho L} \qquad y_d < y < R_w \tag{42}$$

where K is an empirical constant determined from analysis of data and found to equal 0.0072 for a case with reliable mass balances ($\dot{m}_{H_2}$ = 0.06 lbm/sec, 90° injection from a 0.03 in. circumferential wall slot). Thus the E_D model was completely specified in the inner and outer regions. The eddy diffusivity of momentum was defined by the relation,

$$E_M \equiv (E_D)(Sc_T) \tag{43}$$

Comparisons of the predicted E_D profiles with the experimental values led to the following conclusion for the wall slot injector geometry:

(1) The eddy diffusivities of mass, E_D, in the region away from the wall (approximately 80 percent of the duct radius) are predicted with acceptable accuracy (maximum difference of 28 percent) using the mass defect as a correlating parameter.

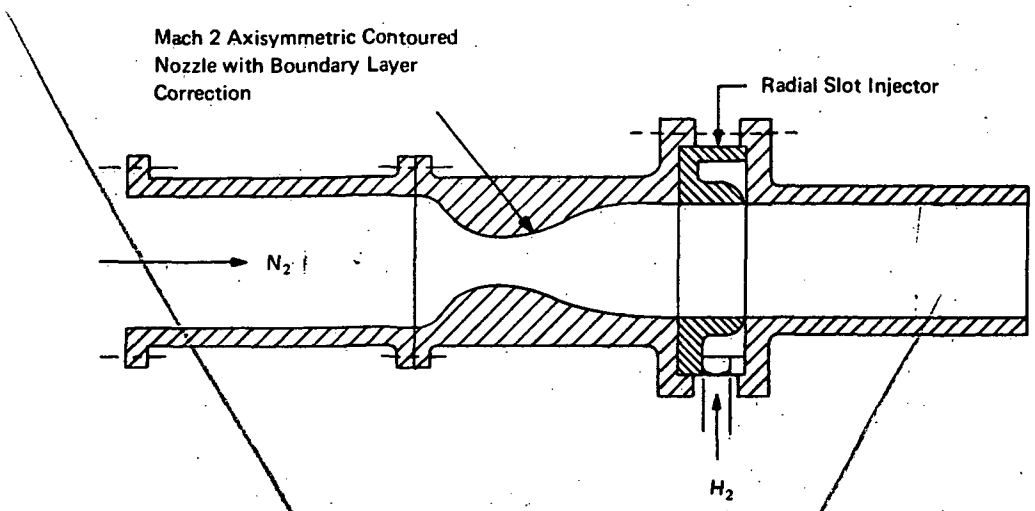

Figure 6. Schematic of Axisymmetric Ducted Supersonic Mixing Experimental Apparatus

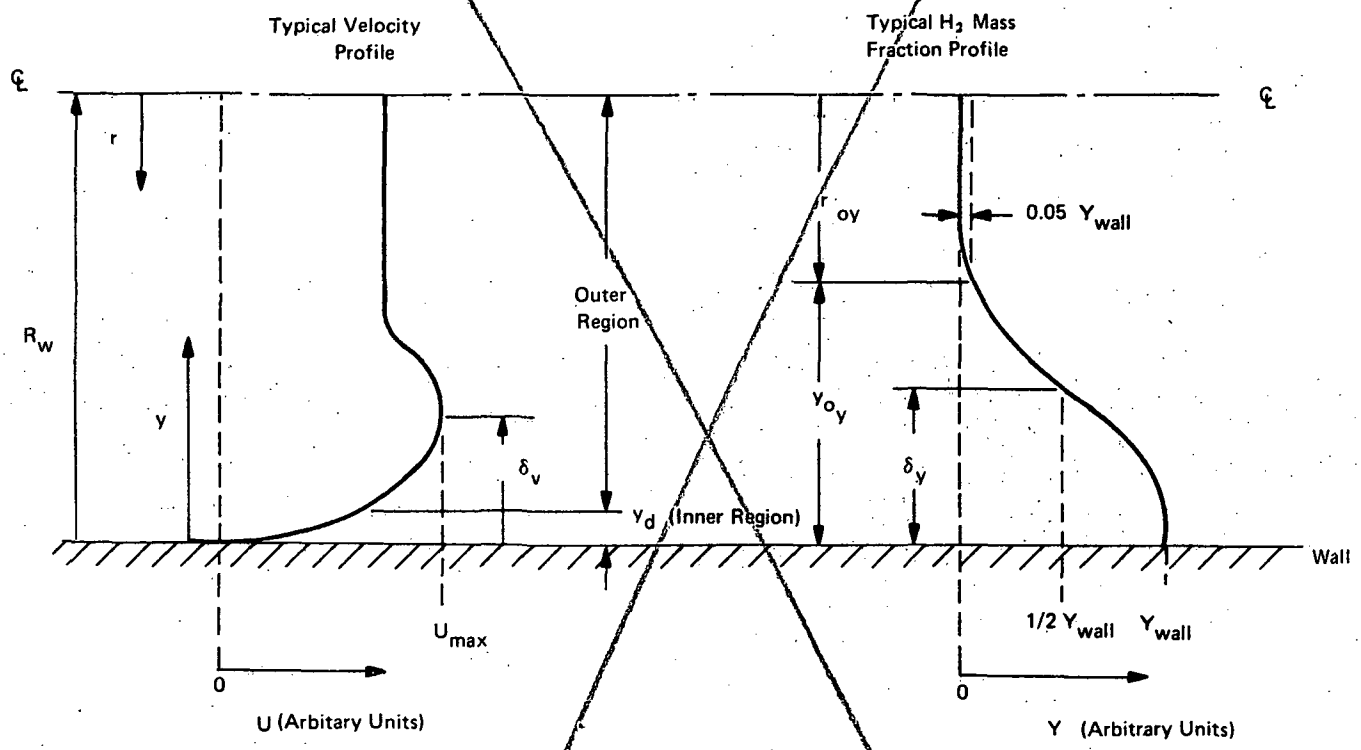

Figure 7 Typical Velocity and Mass Fraction Profiles Downstream of Sonic Injection of H_2 from a Circumferential Wall Slot (See Fig. 6)

The constant c, equation (36), has been found from boundary layer data to be equal to 0.4, whereas the turbulent Schmidt number was assumed equal to 0.7, consistent with both boundary layer and free shear layer data.

von Driest's (ref. 23) damping factor, ω, requires the eddy diffusivity to vanish at the wall, and is given by

$$\omega = (1 - e^{-y/A})^2 \qquad (37)$$

(2) Results were inconclusive regarding suitability of mixing length theory in the inner region to model E_D. Additional analysis can determine whether the differences between predicted (using mixing length theory) and experimental E_D's have a significant effect on the predicted hydrogen concentration.

For calculating the transport coefficients in the outer region of the three-dimensional flow field, equation (42) was replaced by equation (44).

$$E_D = K'\gamma' I/\rho L' \tag{44}$$

where K' is an empirical constant determined from data analysis, γ' is the intermitancy factor, equation (39), but with an argument of y/δ, L' is a characteristic length of the mixing region defined as the half height of the mixing layer on the centerplane, δ, and I is the mass defect in the three-dimensional field. The evaluation of mass defect in the three-dimensional flow field requires integration over the elliptic solution domain of the form

$$I(x) \equiv \int_R |\rho U - \rho_\infty U_\infty| d\tau \tag{45}$$

where the subscripts infinity refer to local free stream reference values. Within the concepts of finite element formalisms, an entirely equivalent form, using the appropriate approximation function description, equation (19), and summation over the finite elements of the discretization is

$$I(x) \equiv \sum_m I_m(x) = \sum_m \int_{R_m} |\rho U_m^* - \rho_\infty U_\infty| dydz \tag{46}$$

The form of ρU_m^* is known and $\rho_\infty U_\infty$ is a local scalar constant. Hence, using equation (21), the mass defect computation becomes

$$I(x) = \sum_m I_m(x) = \sum_m \left[\left\{RHOU\right\}_m^T [\Gamma]_m^T \int_{R_m} \left\{x\right\} d\tau - \rho_\infty U_\infty A_m \right] \tag{47}$$

where A_m is the plane area of the m^{th} finite element. Since both $\left\{RHOU\right\}_m$ and $\rho_\infty U_\infty$ may be functions of x, evaluation of equation (47) is required at each longitudinal computational station. Shown in Figure 8 is a typical COMOC computed turbulent mass mixing coefficient, E_D, distribution through the boundary layer, using equations (35) and (44) for the multiple-jet configuration of Rogers (ref. 6).

The turbulent mixing coefficient distribution used for prediction of momentum transport, E_m, at any point in the flow field requires specification of a turbulent Schmidt number, Sc_T. As with all transport coefficients, COMOC can accept multiple methods of specification for such distributions. Initial studies employed a uniform constant Sc_T, equal to 0.7, which neglected the three-dimensionality of the flow field and consistently predicted over-diffusion of momentum near the wall. Considerable

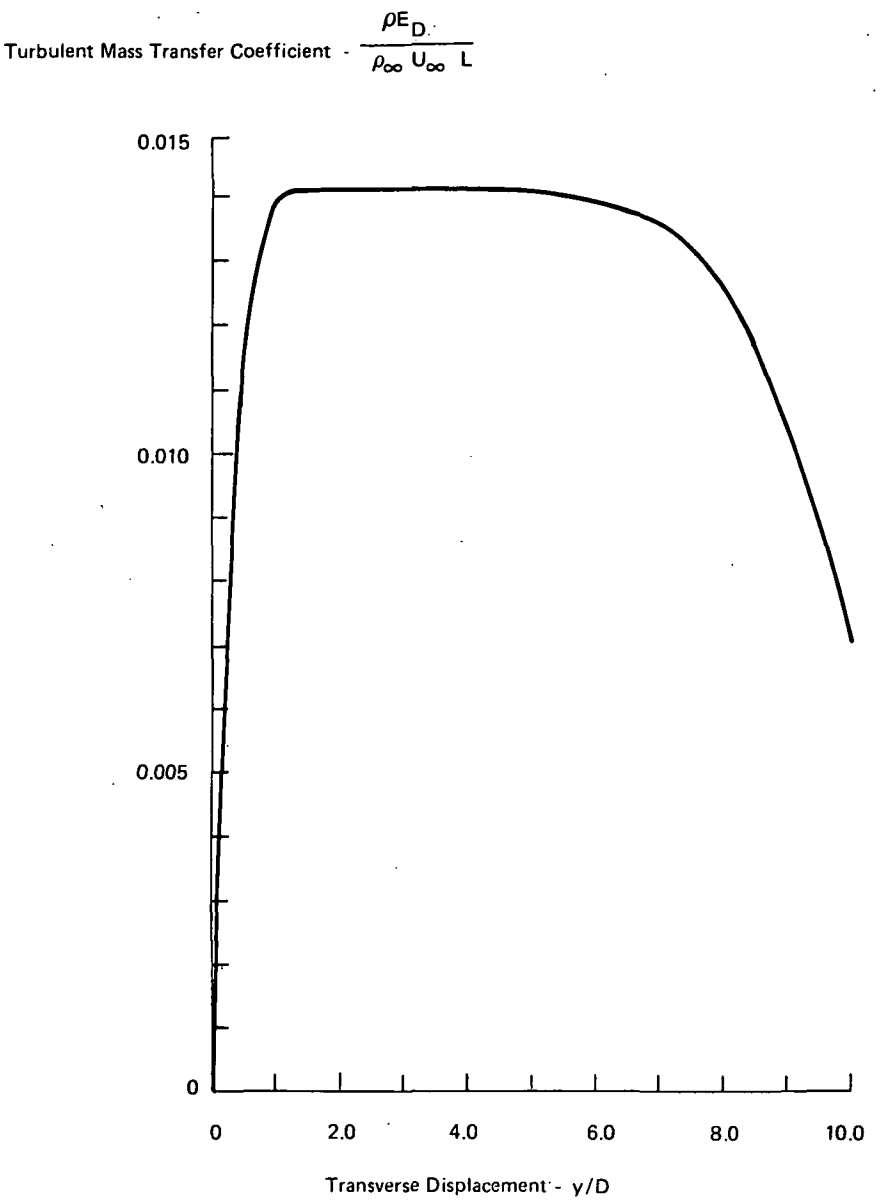

Figure 8. Computed Turbulent Mass Transfer Coefficient Profile on Centerplane (z/D = 0.0) of Multiple-Jet Geometry, q_r = 1.0, x/D = 120

experimentation led to an empirical relationship for a geometric Schmidt number distribution, that enhanced agreement with data, of the form

$$Sc_T \equiv 1. - \frac{r(\theta)}{R(\theta)} \qquad r \leqslant R \qquad (48)$$

In equation (48), $R(\theta)$ describes an ellipse with major axis parallel to the plate and normal to the predominant flow direction, whose center is located at the approximate centroid of the imbedded hydrogen jet (fig. 2). The ellipse selected for the present studies was specified independent of downstream station and established by equation (49).

$$\left(\frac{y/D - 2.5}{2.5}\right)^2 + \left(\frac{z/D}{6.0}\right)^2 = 1 \qquad (49)$$

(2) Results were inconclusive regarding suitability of mixing length theory in the inner region to model E_D. Additional analysis can determine whether the differences between predicted (using mixing length theory) and experimental E_D's have a significant effect on the predicted hydrogen concentration.

For calculating the transport coefficients in the outer region of the three-dimensional flow field, equation (42) was replaced by equation (44).

$$E_D = K'\gamma' I/\rho L' \tag{44}$$

where K' is an empirical constant determined from data analysis, γ' is the intermitancy factor, equation (39), but with an argument of y/δ, L' is a characteristic length of the mixing region defined as the half height of the mixing layer on the centerplane, δ, and I is the mass defect in the three-dimensional field. The evaluation of mass defect in the three-dimensional flow field requires integration over the elliptic solution domain of the form

$$I(x) \equiv \int_R |\rho U - \rho_\infty U_\infty| d\tau \tag{45}$$

where the subscripts infinity refer to local free stream reference values. Within the concepts of finite element formalisms, an entirely equivalent form, using the appropriate approximation function description, equation (19), and summation over the finite elements of the discretization is

$$I(x) \equiv \sum_m I_m(x) = \sum_m \int_{R_m} |\rho U_m^* - \rho_\infty U_\infty| dydz \tag{46}$$

The form of ρU_m^* is known and $\rho_\infty U_\infty$ is a local scalar constant. Hence, using equation (21), the mass defect computation becomes

$$I(x) = \sum_m I_m(x) = \sum_m \left[\left\{RHOU\right\}_m^T [\Gamma]_m^T \int_{R_m} \left\{x\right\} d\tau - \rho_\infty U_\infty A_m \right] \tag{47}$$

where A_m is the plane area of the m^{th} finite element. Since both $\left\{RHOU\right\}_m$ and $\rho_\infty U_\infty$ may be functions of x, evaluation of equation (47) is required at each longitudinal computational station. Shown in Figure 8 is a typical COMOC computed turbulent mass mixing coefficient, E_D, distribution through the boundary layer, using equations (35) and (44) for the multiple-jet configuration of Rogers (ref. 6).

The turbulent mixing coefficient distribution used for prediction of momentum transport, E_m, at any point in the flow field requires specification of a turbulent Schmidt number, Sc_T. As with all transport coefficients, COMOC can accept multiple methods of specification for such distributions. Initial studies employed a uniform constant Sc_T, equal to 0.7, which neglected the three-dimensionality of the flow field and consistently predicted over-diffusion of momentum near the wall. Considerable

Additionally, $r(\theta)$ is the magnitude of a position vector to any point within the ellipse and aligned parallel to $R(\theta)$, and determined as

$$r(\theta) = \sqrt{(y/D - 2.5)^2 + (z/D)^2} \tag{50}$$

Along the plate surface, the Schmidt number was uniformly set equal to 0.7. Elsewhere outside the ellipse, the Schmidt number distribution was held constant at those values used in the initial studies that determined equation (48).

Prediction of Mass and Momentum Transport Following Transverse Injection of Hydrogen from a Single Orifice

At some location downstream from transverse injection, as a function of the dynamic pressure ratio q_r, boundary layer reattachment occurs, (fig. 5a), and the three-dimensional elliptic boundary layer equations become valid. For the configuration of Rogers (ref. 5), reattachment should occur by station x/D=30, where D is the injection orifice diameter. Therefore, evaluation of the prototype three-dimensional turbulent mixing model was performed in the downstream region $30 \leqslant x/D \leqslant 120$.

It is necessary to establish initial conditions for the planar distribution of all dependent variables at x/D=30. The original raw data of Rogers (ref. 5) consisted of pitot-static and hydrogen sampling data points on four traverses in the (y, z) plane (fig. 2). The vertical traverse, in the streamwise plane through the injection orifice and parallel to the y axis, determined the y locations where hydrogen concentration was maximum, $(y/D)_{max}$, and where it vanished, i.e., the freestream boundary. Three horizontal data traverses were then made parallel to the plate surface, at y locations corresponding to $(y/D)_{max}$, and at a location each side of $(y/D)_{max}$ approximately bisecting the respective domains. Shown in figure 9 are the horizontal traverse data at x/D=30 for q_r=1.0. The curves appear of Gaussian shape; an apparent symmetry plane exists which is displaced from the geometric plane of symmetry, i.e., z=0, as Rogers observed.

Although the entire flow field could be computed numerically, the strong appearance of a data symmetry plane suggests establishing a corresponding solution domain. Therefore, these data were input to a cubic spline interpolation computer program that established the z location of the data symmetry plane via a minimization criteria. For the data of figure 9, the symmetry plane was located at z/D=-0.7, in agreement with folding the data manually and matching the "wings" of the Gaussian shaped curves. Having thus established the symmetry plane, the spline package curve fit both the Y and u displaced data, and evaluated the interpolation polynomials at node points of the finite element discretization of the elliptic solution domain (fig. 10). A number of different discretizations were evaluated; in each case, the spline package provided appropriate initial data.

Shown in figure 11, for planes z=constant of the discretization of figure 10, are the spline-computed data fits compared to the span of the measured raw data, and the subsequent data range for the "best symmetry plane" determination. Data symmetry occurs to within about ±0.2% of the maximum hydrogen deviation, and computations were performed using only the half-plane discretization of figure 10. These same manipulation operations were performed on Rogers data at stations x/D=60 and 120 to establish comparison bases. Shown in figure 12 is the corresponding, and more familiar (see ref. 5) contour distribution of hydrogen mass fraction at x/D=30, as computed by the symmetrized spline function interpolation of the data. In both figures 11 and 12, note that the contours do not penetrate to the plate surface, since no data are available below the lowest horizontal data survey except on the geometry symmetry plane.

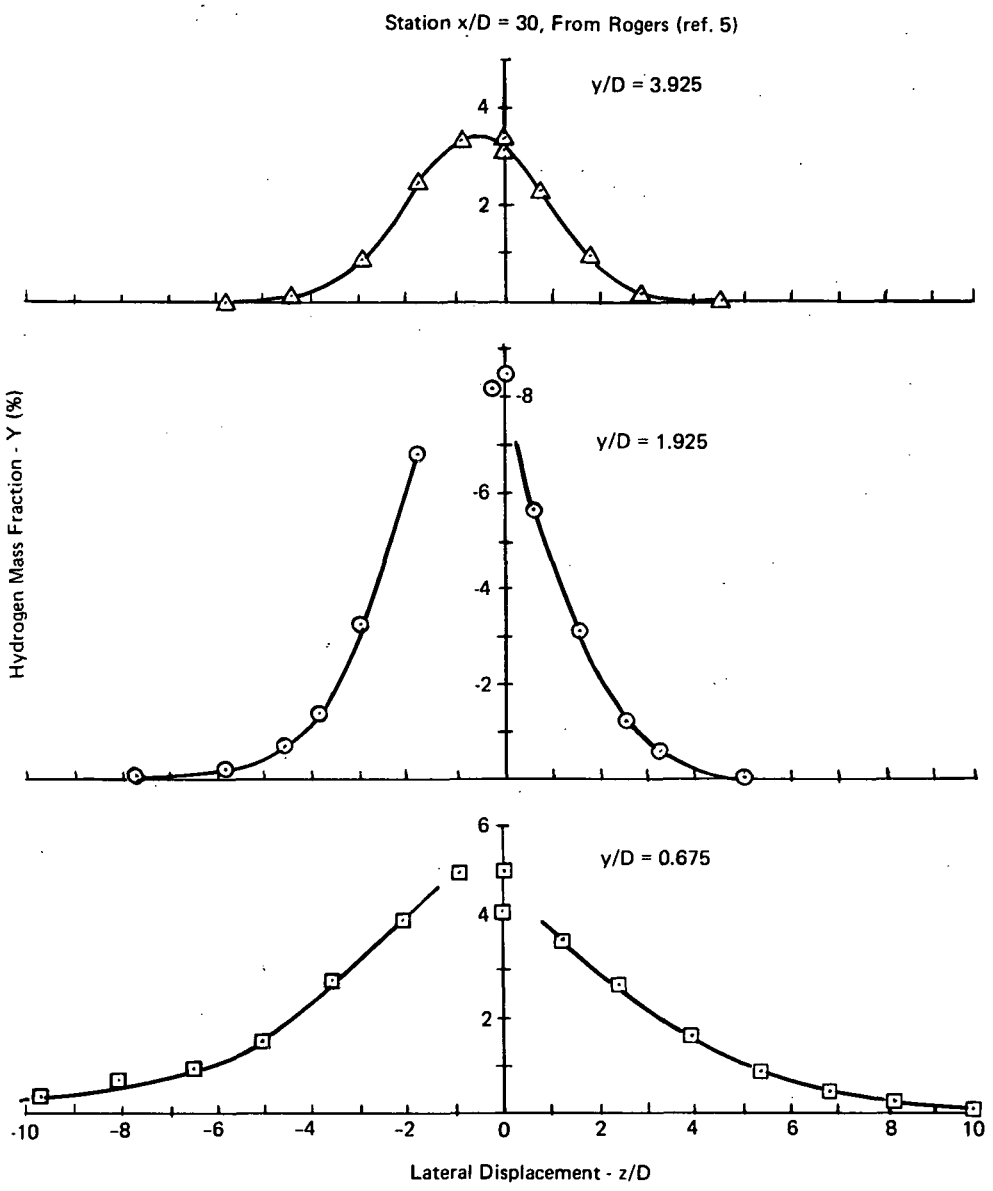

Figure 9. Experimentally Measured Mass Fraction for Injection from a Single Orifice

Shown in figure 13 is the COMOC computed hydrogen mass fraction contour distribution at station x/D=60. Superimposed for comparison purposes are the (spread of) data as spline-interpolated for the best symmetry plane fit. Agreement of the results along the symmetry plane, z = 0., is excellent. These results were achieved for the turbulent mixing model previously described for K '= 0.1 (equation 44). Transition from mixing length to mass defect modeling occurred between 0.6 and 1.0 injection diameters above the plate, across the entire pattern. The lateral spreading of the jet (parallel to z axis) is predicted accurately near the wall, but excessive concentration levels are predicted in the middle region of the pattern.

The transition from the initial distribution, and significant detail on solution accuracy, are presented in figure 14, which contains data and computed concentration profiles along planes z=constant at x/D=60. The indicated disagreement between data and computations, figure 13, may be directly

Additionally, $r(\theta)$ is the magnitude of a position vector to any point within the ellipse and aligned parallel to $R(\theta)$, and determined as

$$r(\theta) = \sqrt{(y/D - 2.5)^2 + (z/D)^2} \tag{50}$$

Along the plate surface, the Schmidt number was uniformly set equal to 0.7. Elsewhere outside the ellipse, the Schmidt number distribution was held constant at those values used in the initial studies that determined equation (48).

Prediction of Mass and Momentum Transport Following Transverse Injection of Hydrogen from a Single Orifice

At some location downstream from transverse injection, as a function of the dynamic pressure ratio q_r, boundary layer reattachment occurs, (fig. 5a), and the three-dimensional elliptic boundary layer equations become valid. For the configuration of Rogers (ref. 5), reattachment should occur by station x/D=30, where D is the injection orifice diameter. Therefore, evaluation of the prototype three-dimensional turbulent mixing model was performed in the downstream region $30 \leqslant x/D \leqslant 120$.

It is necessary to establish initial conditions for the planar distribution of all dependent variables at x/D=30. The original raw data of Rogers (ref. 5) consisted of pitot-static and hydrogen sampling data points on four traverses in the (y, z) plane (fig. 2). The vertical traverse, in the streamwise plane through the injection orifice and parallel to the y axis, determined the y locations where hydrogen concentration was maximum, $(y/D)_{max}$, and where it vanished, i.e., the freestream boundary. Three horizontal data traverses were then made parallel to the plate surface, at y locations corresponding to $(y/D)_{max}$, and at a location each side of $(y/D)_{max}$ approximately bisecting the respective domains. Shown in figure 9 are the horizontal traverse data at x/D=30 for q_r=1.0. The curves appear of Gaussian shape; an apparent symmetry plane exists which is displaced from the geometric plane of symmetry, i.e., z=0, as Rogers observed.

Although the entire flow field could be computed numerically, the strong appearance of a data symmetry plane suggests establishing a corresponding solution domain. Therefore, these data were input to a cubic spline interpolation computer program that established the z location of the data symmetry plane via a minimization criteria. For the data of figure 9, the symmetry plane was located at z/D=-0.7, in agreement with folding the data manually and matching the "wings" of the Gaussian shaped curves. Having thus established the symmetry plane, the spline package curve fit both the Y and u displaced data, and evaluated the interpolation polynomials at node points of the finite element discretization of the elliptic solution domain (fig. 10). A number of different discretizations were evaluated; in each case, the spline package provided appropriate initial data.

Shown in figure 11, for planes z=constant of the discretization of figure 10, are the spline-computed data fits compared to the span of the measured raw data, and the subsequent data range for the "best symmetry plane" determination. Data symmetry occurs to within about ±0.2% of the maximum hydrogen deviation, and computations were performed using only the half-plane discretization of figure 10. These same manipulation operations were performed on Rogers data at stations x/D=60 and 120 to establish comparison bases. Shown in figure 12 is the corresponding, and more familiar (see ref. 5) contour distribution of hydrogen mass fraction at x/D=30, as computed by the symmetrized spline function interpolation of the data. In both figures 11 and 12, note that the contours do not penetrate to the plate surface, since no data are available below the lowest horizontal data survey except on the geometry symmetry plane.

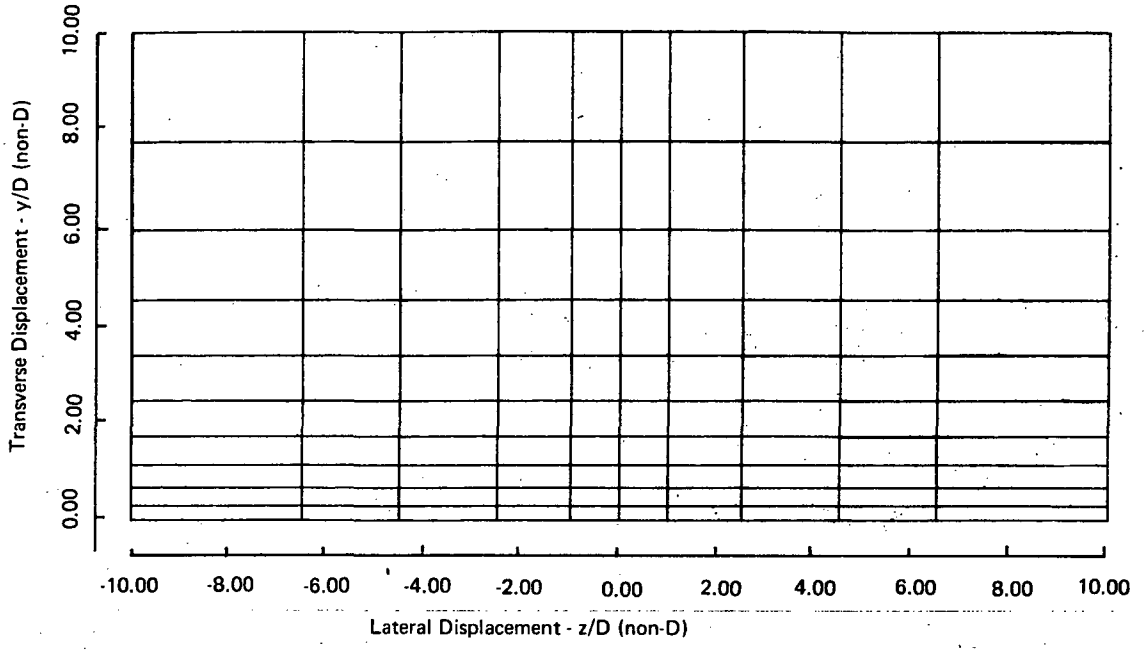

Figure 10. Finite Element Discretion of Elliptic Solution Domain for Single-Jet Injection Analyses

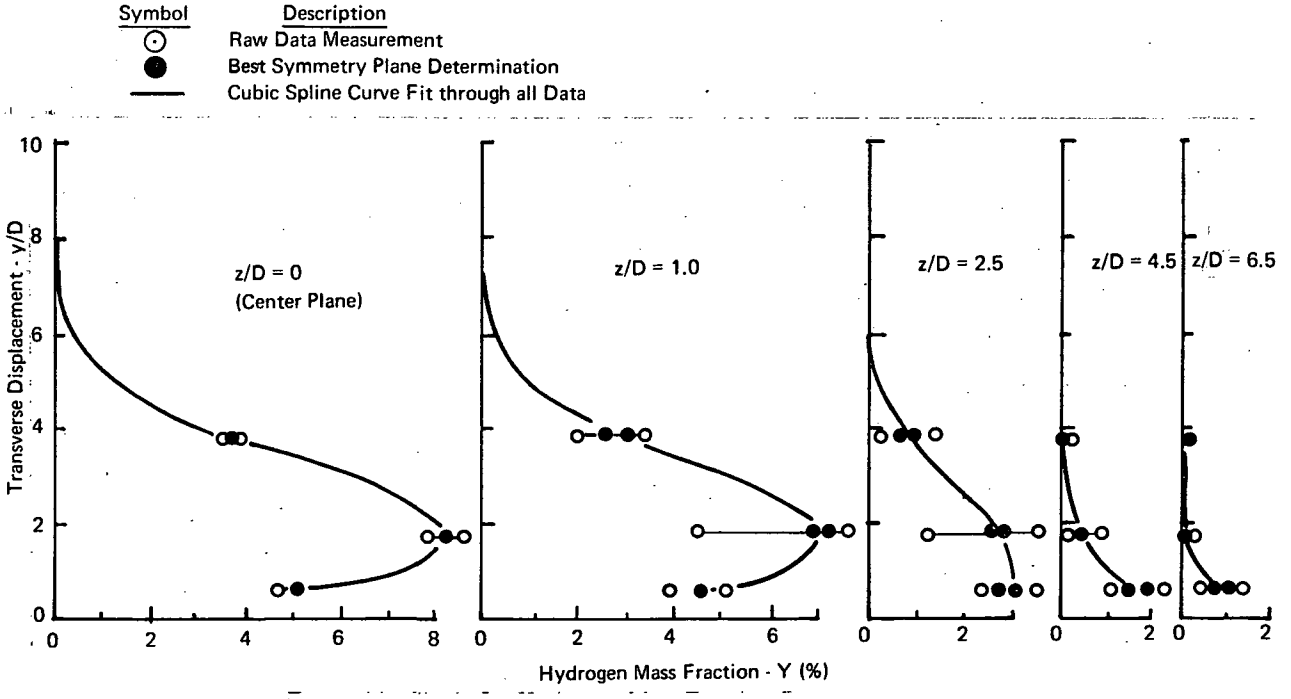

Figure 11. Single-Jet Hydrogen Mass Fraction Distributions at Station x/D = 30, q_r = 1.0, After Rogers (Ref. 5)

assessed as lack of hydrogen diffusion from the core region in the lateral direction. Since the turbulent transport model is an extension of two-dimensional concepts, it is insensitive to variable gradients parallel to the z-axis. However, the experimental data show that in this region, $u_{,y}$ and $u_{,z}$ are of about equal magnitude. This is readily observed in figure 15, which is a three-dimensional surface plot of the

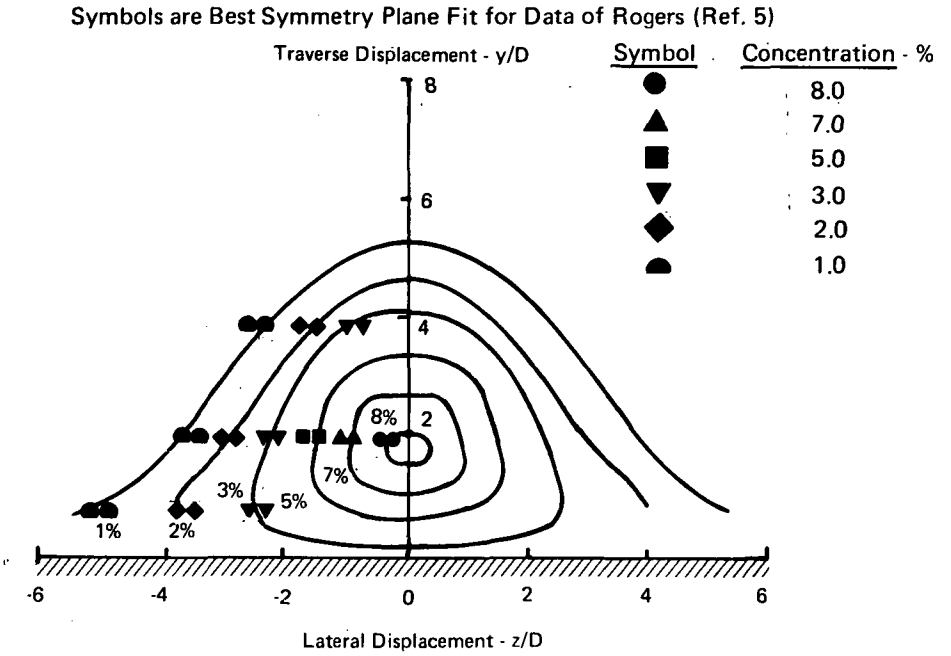

Figure 12. Cubic Spline Interpolated Hydrogen Mass Fraction Contours for Single-Jet, $q_r = 1.0$, $x/D = 30$.

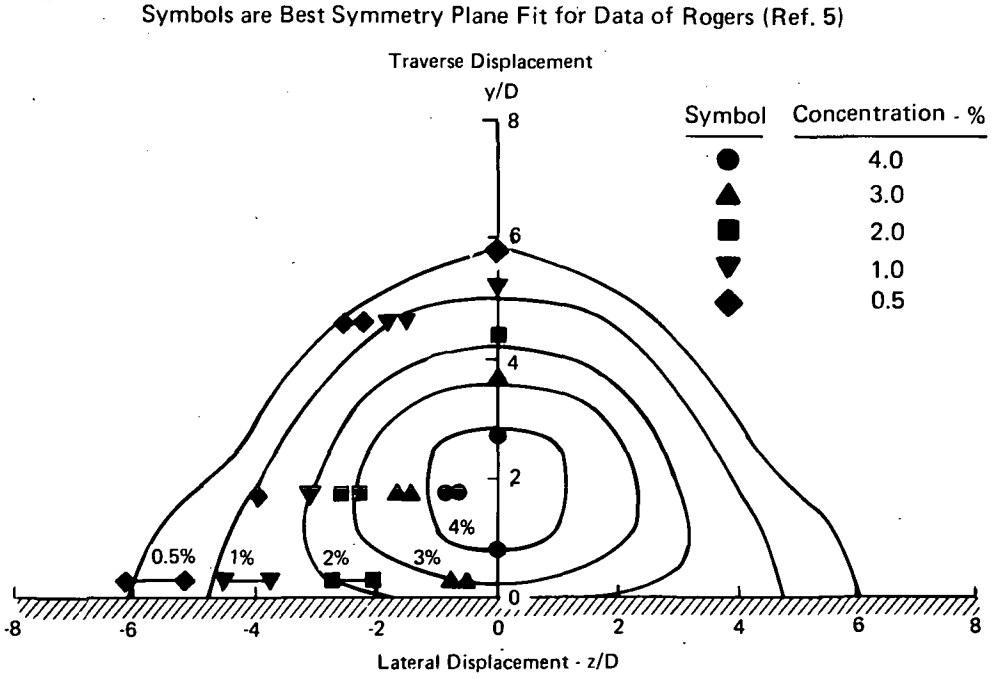

Figure 13. Comparison Between COMOC Computed Hydrogen Mass Fraction Contours and Experimental Data for Single - Jet, $q_r = 1.0$, $x/D = 60$.

velocity distribution at x/D=30, as observed from a viewpoint beneath the plate surface. The superimposed grid coincides with the finite element discretization (fig. 10) and the hydrogen jet is imbedded within the centroidal indentation. Obviously, these three-dimensional effects are important, and should form an integral part of future development studies. The lack of data and subsequent neglect of lateral velocity (w) would also exert an influence on spreading.

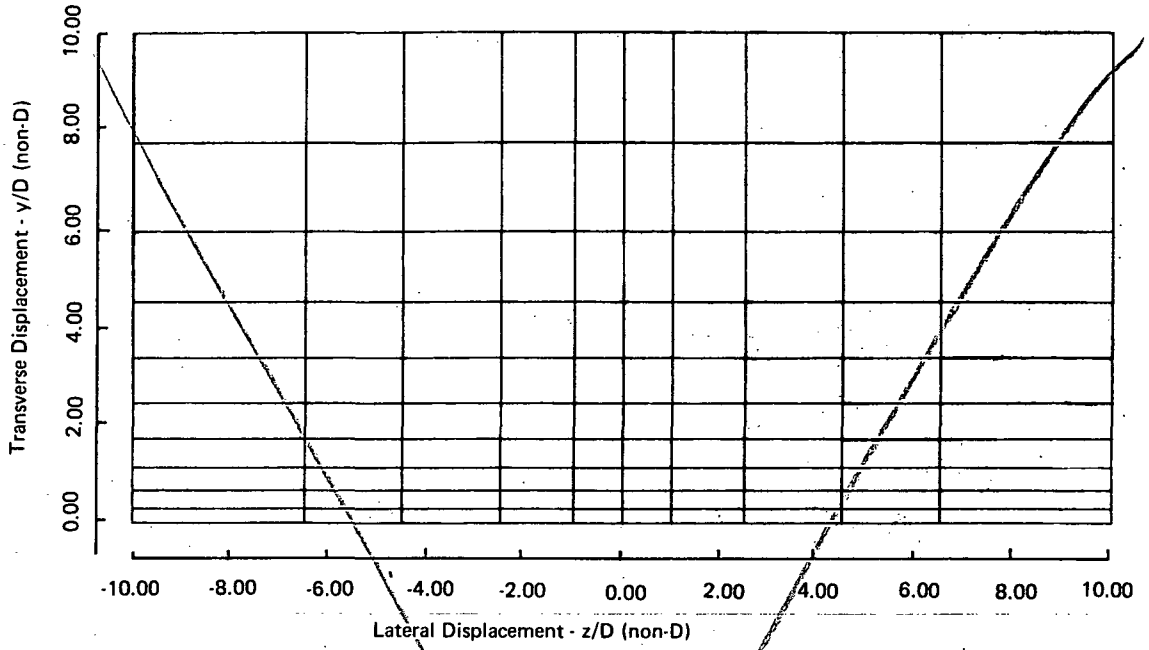

Figure 10. Finite Element Discretion of Elliptic Solution Domain for Single-Jet Injection Analyses

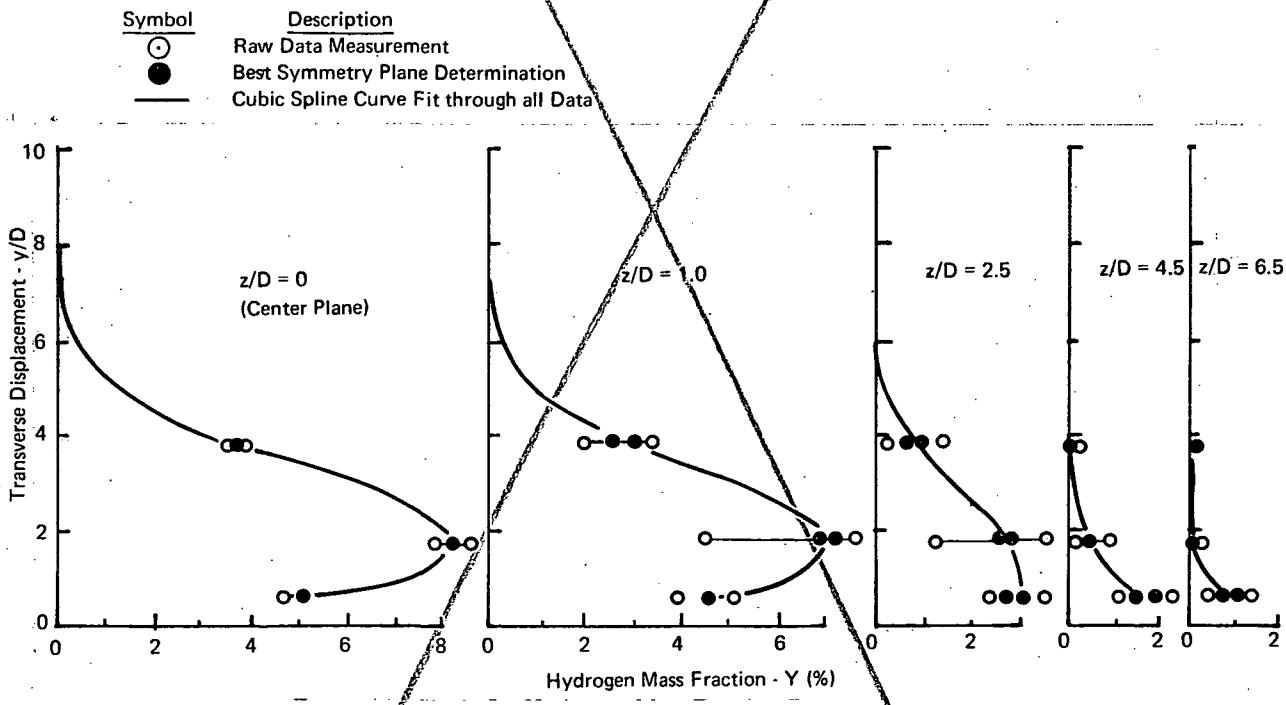

Figure 11. Single-Jet Hydrogen Mass Fraction Distributions at Station x/D = 30, q_r = 1.0, After Rogers (Ref. 5)

assessed as lack of hydrogen diffusion from the core region in the lateral direction. Since the turbulent transport model is an extension of two-dimensional concepts, it is insensitive to variable gradients parallel to the z-axis. However, the experimental data show that in this region, $u_{,y}$ and $u_{,z}$ are of about equal magnitude. This is readily observed in figure 15, which is a three-dimensional surface plot of the

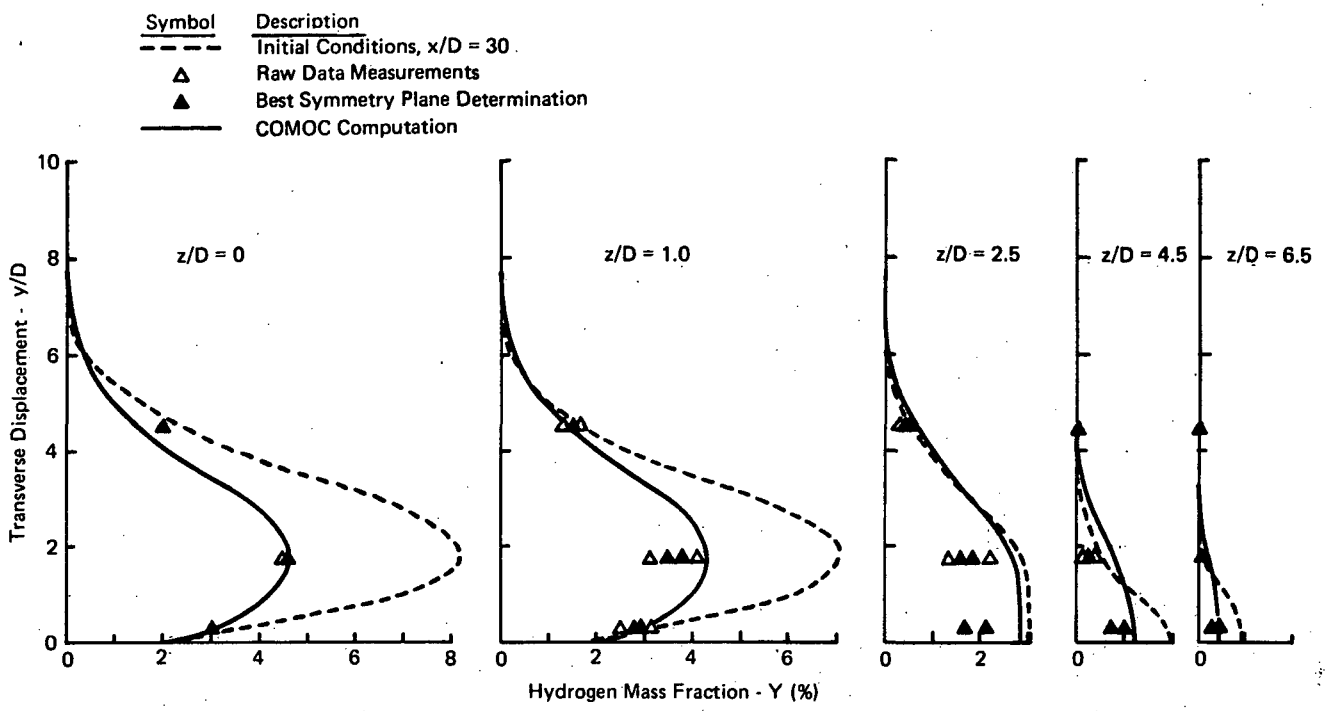

Figure 14. Computed Single-Jet Hydrogen Mass Fraction Distribution at Station x/D = 60, $q_r = 1.0$

Note also in figure 14, that the initial data profiles (dashed lines) have been extrapolated to the plate surface, as is required to establish initial conditions for hydrogen mass fraction, Y. Only after considerable scrutinizing of the data, and extensive numerical experimentation with boundary conditions for Y on the plate surface, were the illustrated results achieved. Referring to figure 11, considerable option exists for extrapolating the data at planes z=0. and z=1.0. It appears that the hydrogen jet is held off the wall in this region by some mechanism, while the Y contours for larger z quite obviously will intersect the wall in an approximately normal fashion. Employing a vanishing gradient boundary condition for Y across the entire plate surface always resulted in the maximum local hydrogen concentration sinking to the wall by, or shortly after, station 60. This result suggested that alternate wall boundary conditions be considered. Looking at experimental data for stations 30, 60, and 120 (fig. 16), one might conclude that the wall concentration of hydrogen never exceeds about 2% directly underneath the injection pattern, and that a local maximum may well exist off-axis, i.e., $z \neq 0$. The computational solutions, leading to the results shown in figures 14 and 16, numerically "froze" the concentration of hydrogen at 2% at the wall nodes, located at z/D=0. and z/D=1.0, while enforcing a vanishing normal gradient at the remaining wall nodes, i.e., z/D>1.0. For these conditions, the indicated good agreement near the centerplane was achieved.

It is instructive to note that these observations, and the versatility of the numerical experimentation capability to routinely change boundary conditions and test theories, may exert considerable impact upon design. In figure 5, reattachment of the boundary layer is estimated to occur at some point downstream of injection. This has been largely confirmed; however, the physics of the reattachment appear to isolate the peak hydrogen concentration from the plate. The impact of this phenomenon on actual combustion, and wall cooling requirements, could be rather important for actual combustor design.

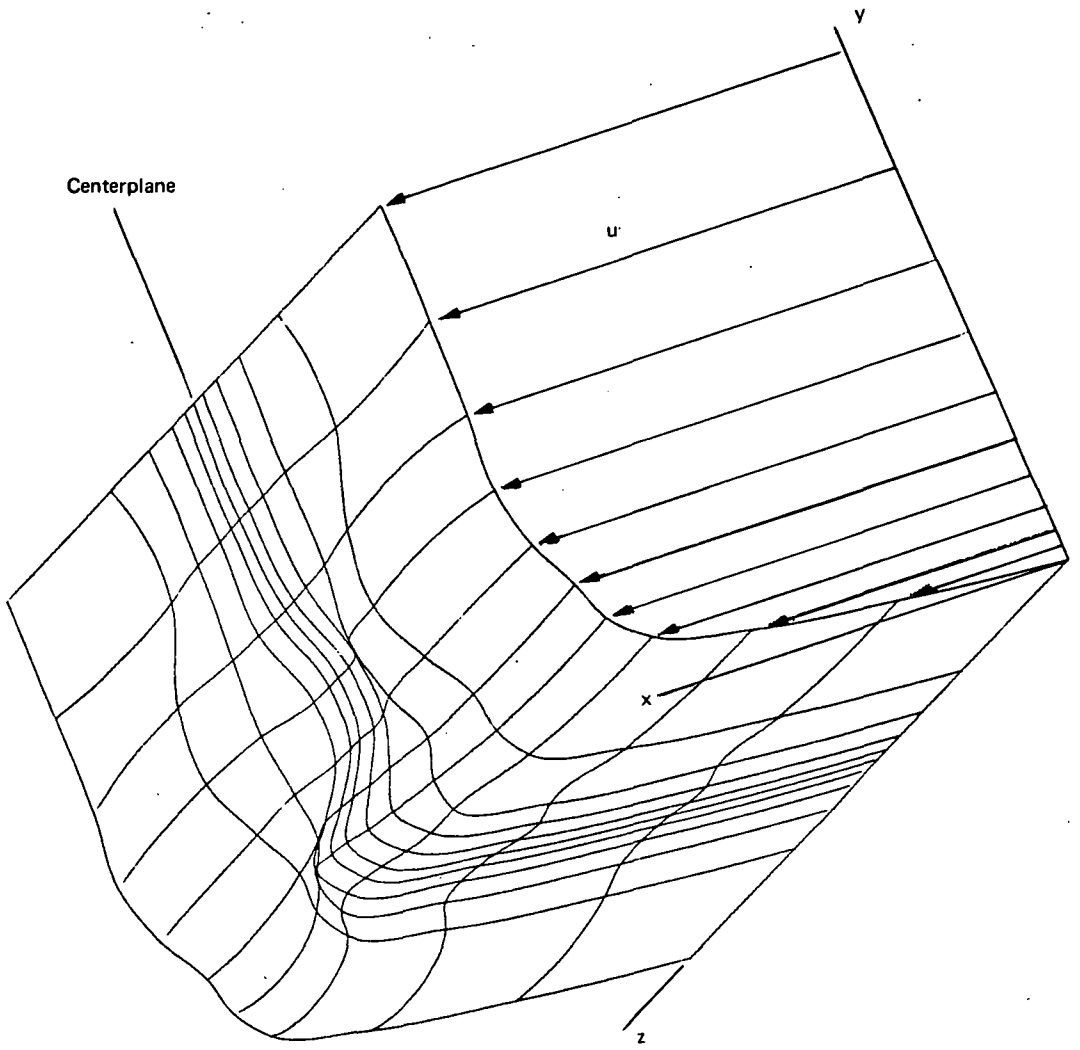

Figure 15. Isometric View of Three-Dimensional Velocity Surface for Single-Jet Configuration, x/D = 30, After Rogers (Ref. 5)

Figures 17 and 18 compare the computed solutions for longitudinal velocity distribution to data at stations x/D=60 and 120 as well as the initial distributions. Agreement is generally good. The experimental data are quite sparse; the apparent acceleration of flow near the plat surface between x/D=30 and 60 was computationally encouraged by the Schmidt number distribution described by equation (48). The CPU execution time on the IBM 360/65 digital computer, including all turbulence computations and detailed output was 1070 seconds with all operations performed using single precision arithmetic.

Prediction of Mass and Momentum Transport Following Transverse Injection From Multiple Orifices

The computational study described for the single-jet configuration was repeated for data of Rogers (ref. 6) obtained for transverse injection (at q_r=1.0 into a Mach 4 airstream) from a row of orifices, aligned perpendicular to the main flow vector with a uniform separation distance of 12.5

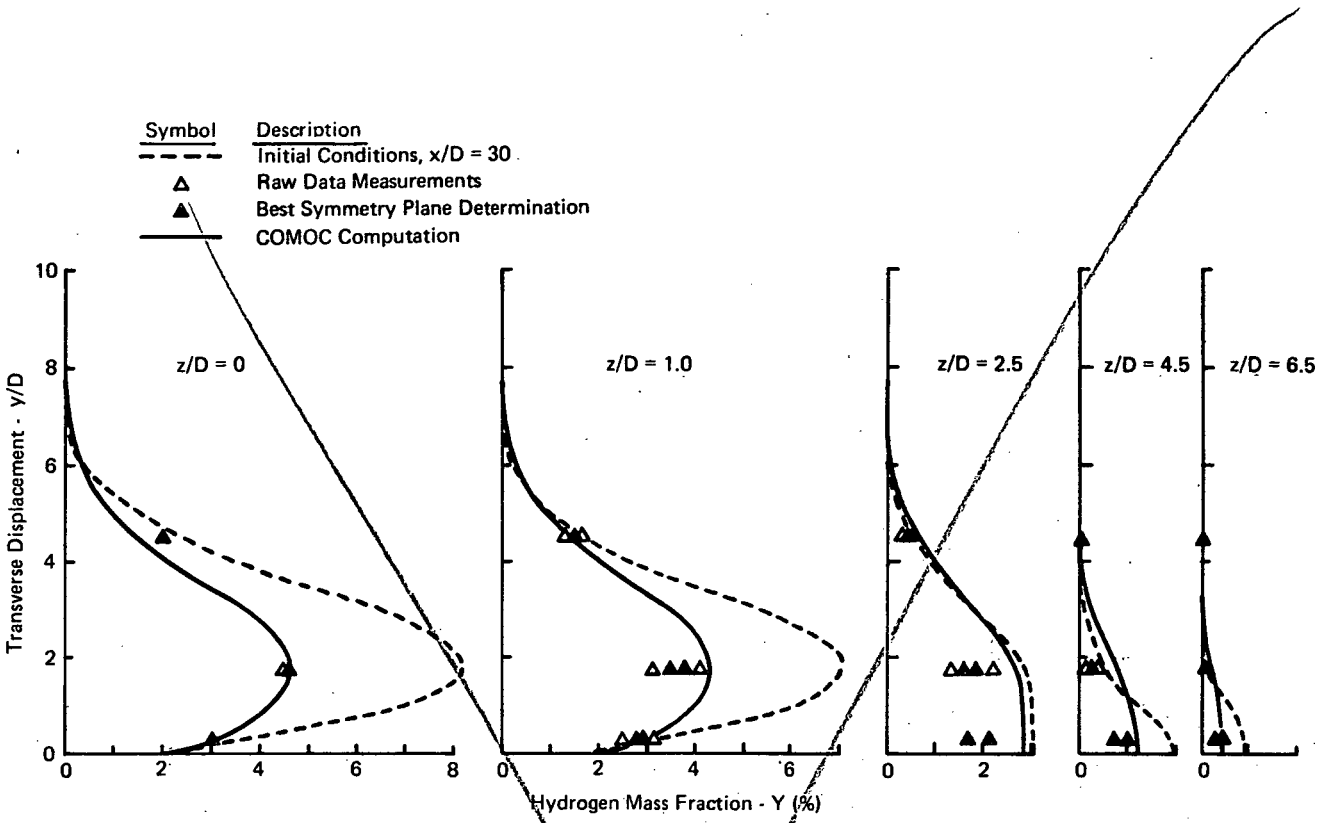

Figure 14. Computed Single-Jet Hydrogen Mass Fraction Distribution at Station x/D = 60, $q_r = 1.0$

Note also in figure 14, that the initial data profiles (dashed lines) have been extrapolated to the plate surface, as is required to establish initial conditions for hydrogen mass fraction, Y. Only after considerable scrutinizing of the data, and extensive numerical experimentation with boundary conditions for Y on the plate surface, were the illustrated results achieved. Referring to figure 11, considerable option exists for extrapolating the data at planes z=0. and z=1.0. It appears that the hydrogen jet is held off the wall in this region by some mechanism, while the Y contours for larger z quite obviously will intersect the wall in an approximately normal fashion. Employing a vanishing gradient boundary condition for Y across the entire plate surface always resulted in the maximum local hydrogen concentration sinking to the wall by, or shortly after, station 60. This result suggested that alternate wall boundary conditions be considered. Looking at experimental data for stations 30, 60, and 120 (fig. 16), one might conclude that the wall concentration of hydrogen never exceeds about 2% directly underneath the injection pattern, and that a local maximum may well exist off-axis, i.e., $z \neq 0$. The computational solutions, leading to the results shown in figures 14 and 16, numerically "froze" the concentration of hydrogen at 2% at the wall nodes, located at z/D=0. and z/D=1.0, while enforcing a vanishing normal gradient at the remaining wall nodes, i.e., z/D>1.0. For these conditions, the indicated good agreement near the centerplane was achieved.

It is instructive to note that these observations, and the versatility of the numerical experimentation capability to routinely change boundary conditions and test theories, may exert considerable impact upon design. In figure 5, reattachment of the boundary layer is estimated to occur at some point downstream of injection. This has been largely confirmed; however, the physics of the reattachment appear to isolate the peak hydrogen concentration from the plate. The impact of this phenomenon on actual combustion, and wall cooling requirements, could be rather important for actual combustor design.

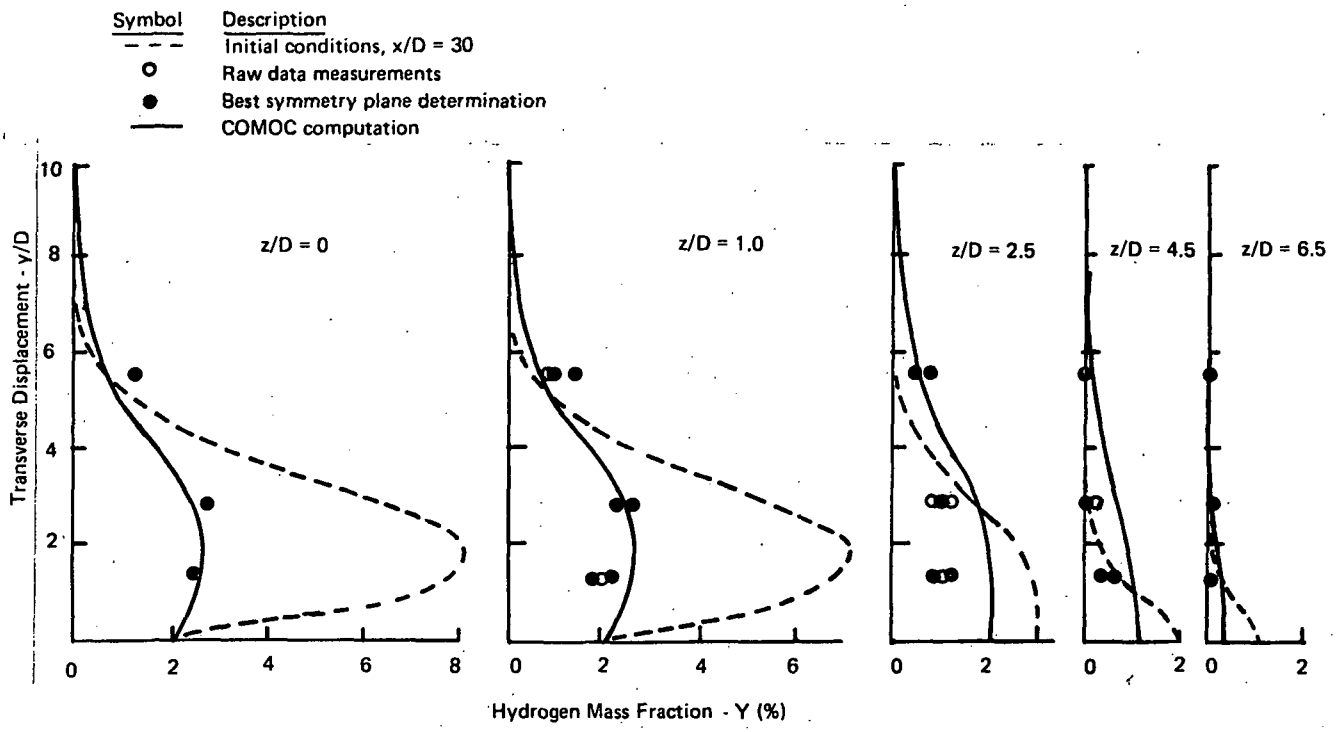

Figure 16. Computed Single-Jet Hydrogen Mass Fraction Distribution at Station x/D = 120, q_r= 1

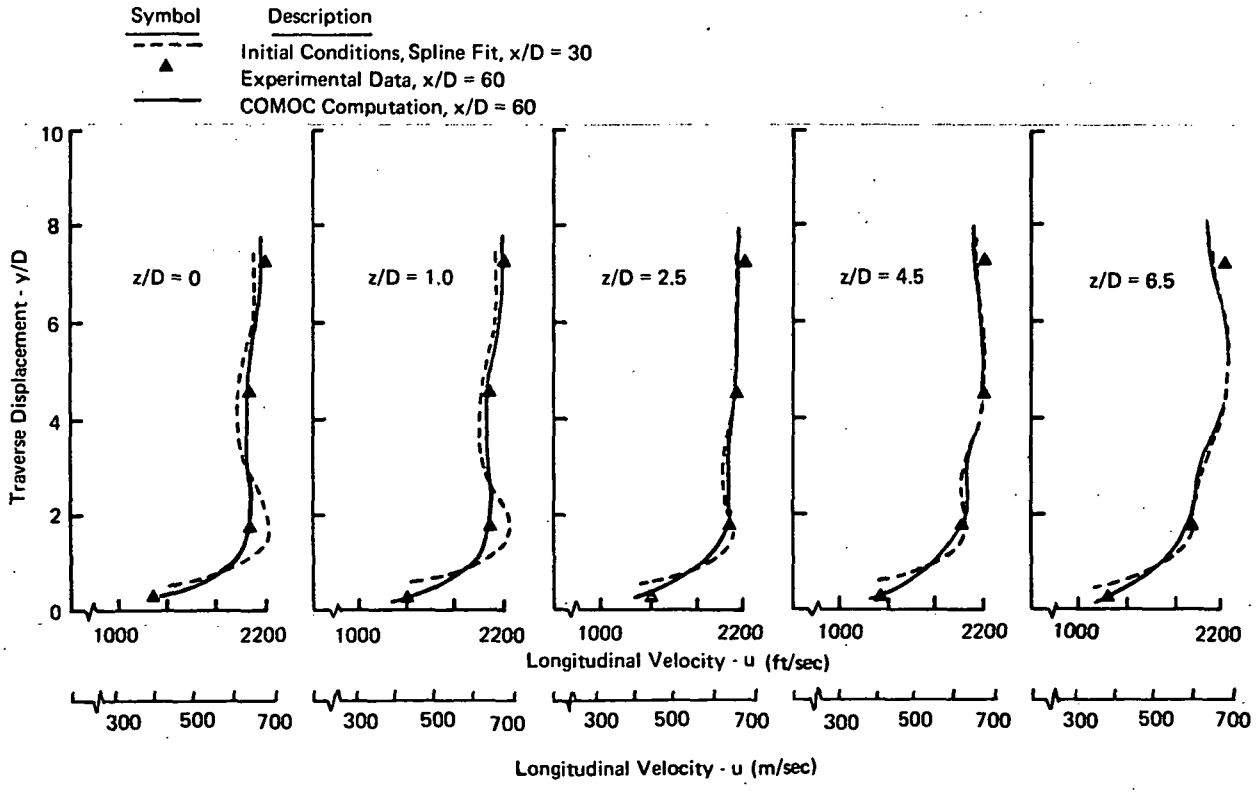

Figure 17. Computed Single-Jet Longitudinal Velocity Distribution at Station x/D = 60, q_r = 1

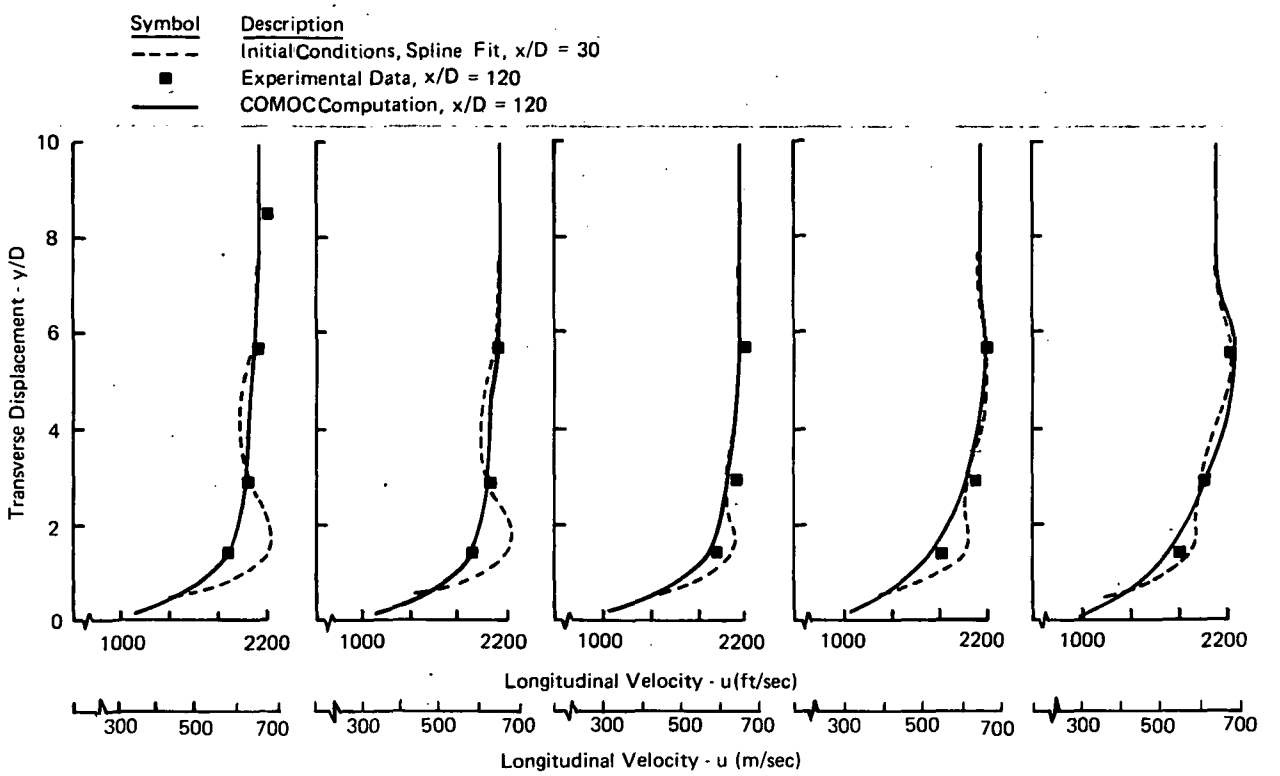

Figure 18. Computed Single-Jet Longitudinal Velocity Distribution at Station x/D = 120, q_r = 1.0

orifice diameters (D). Discretization of the finite element domain parallel to the y axis, figure 10, remained the same. The discretization in the lateral direction was refined such that the node columns spanned $-6.25 \leq z/D \leq 6.25$, i.e., the half-width of orifice separation.

The raw data were again analyzed using the cubic-spline interpolation package. A data symmetry plane was established by the minimization procedure. Shown in figure 19 are the spline-interpolated data profiles on planes z=constant at station x/D=30, as well as the best symmetry plane data spread. Therefore, as with the single-jet study, a half-plane computational domain was sufficient. Vanishing gradient boundary conditions were then applied along both lateral planes to simulate multiple injectors.

Shown in figures 20 and 21 are the COMOC computed hydrogen mass fraction profile distributions at stations x/D=60 and x/D=120, and figure 22 displays the more familiar contour plot of the hydrogen distribution at x/D=120. These results were obtained using the identical mixing model of the single jet, i.e., K=0.1 (equation 44) with transition from mixing length to mass defect occurring in the region $0.6 \leq y/D \leq 1.1$. Figure 20 indicates that the center plane diffusion is somewhat over-predicted, while a considerable improvement between data and computations has occurred in the lateral region; i.e., $z/D \geq 2.0$, using the same "frozen" hydrogen boundary condition at the plate surface underneath the jet centroid (only). These same conclusions hold at x/D=120 (fig. 21) and figure 22 illustrates how the contour patterns merge between jets for the multiple injector configuration. Agreement between computed and measured velocity distributions at both downstream stations was good.

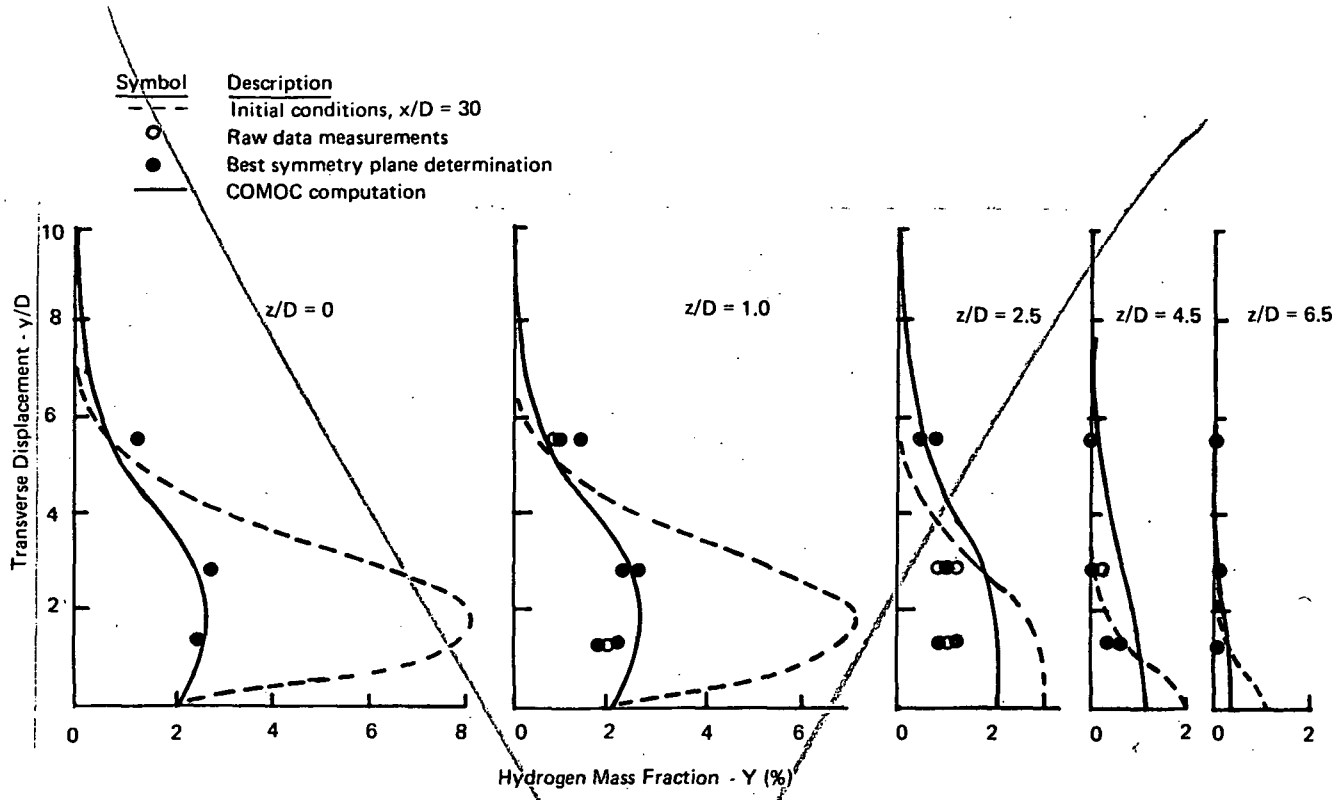

Figure 16. Computed Single-Jet Hydrogen Mass Fraction Distribution at Station x/D = 120, q_r = 1

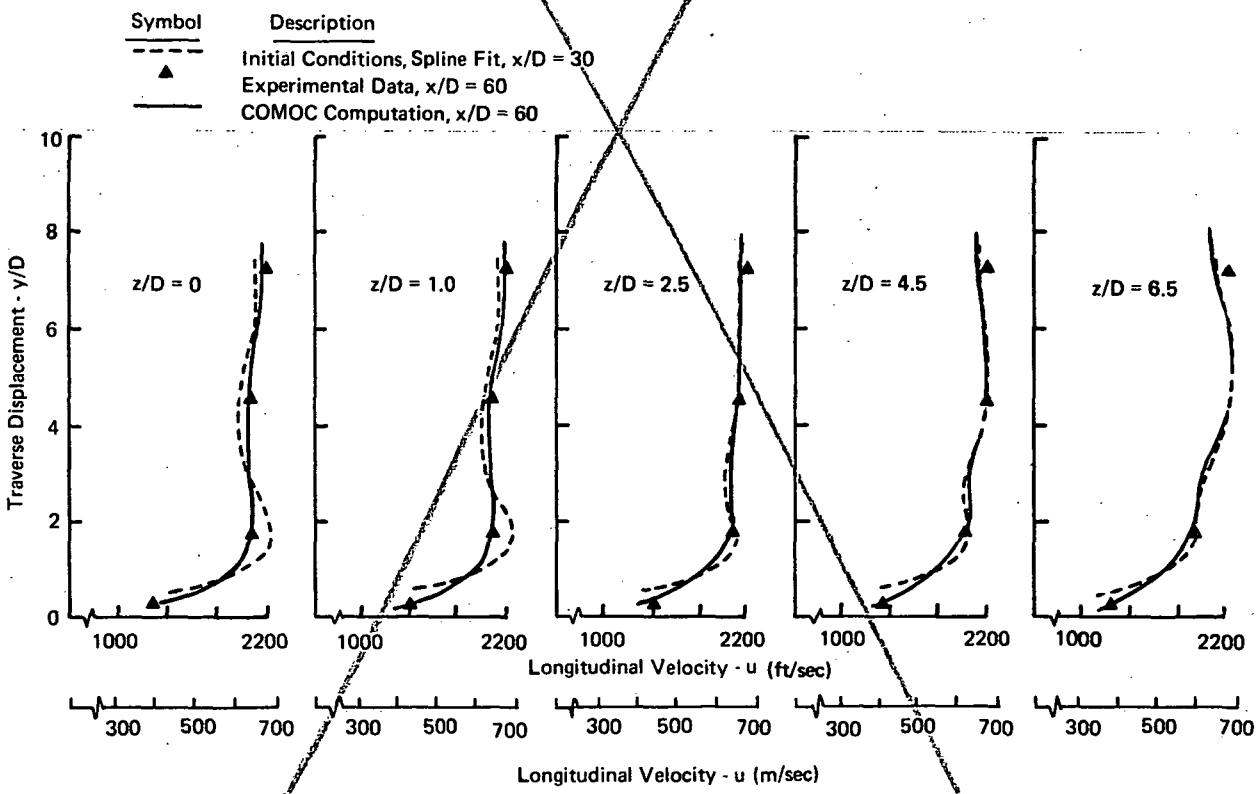

Figure 17. Computed Single-Jet Longitudinal Velocity Distribution at Station x/D = 60, q_r = 1

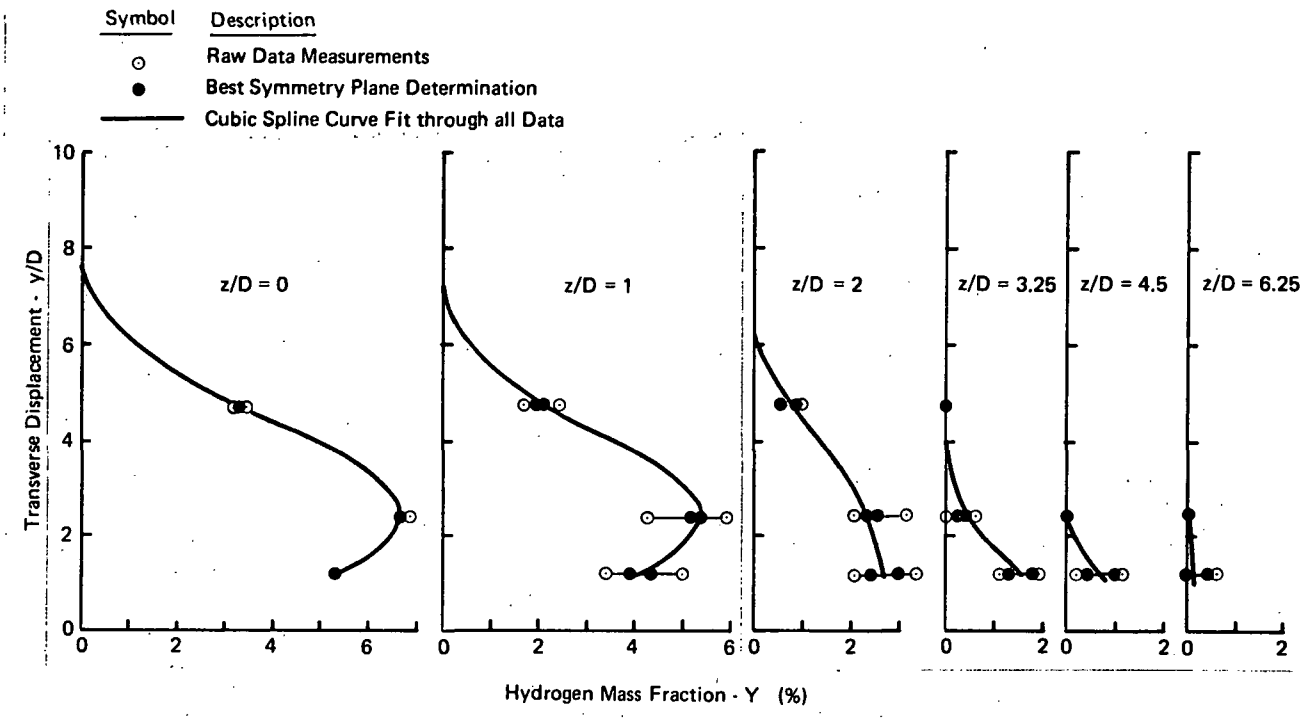

Figure 19. Multi-Jet Hydrogen Mass Fraction Distributions at Station x/D = 30, q_r = 1.0, After Rogers (Ref. 6)

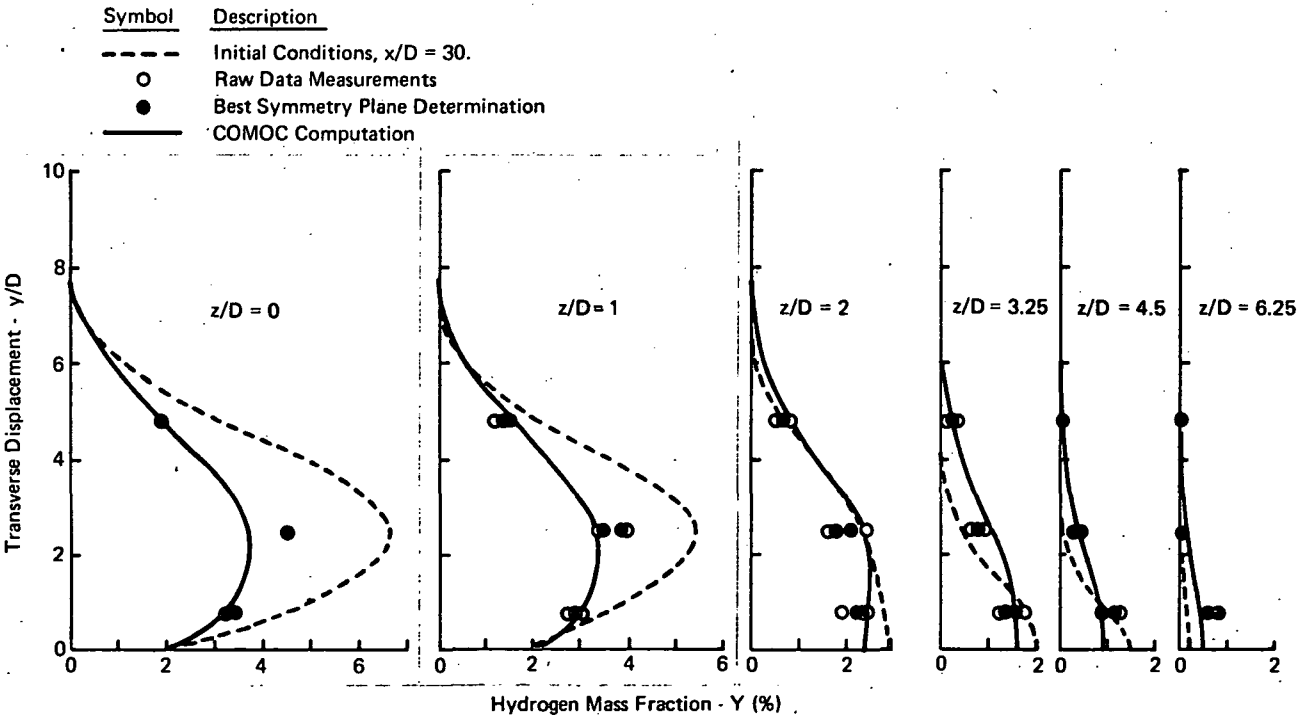

Figure 20. Computed Multi-Jet Hydrogen Mass Fraction Comparison Distribution at Station x/D = 60, q_r = 1

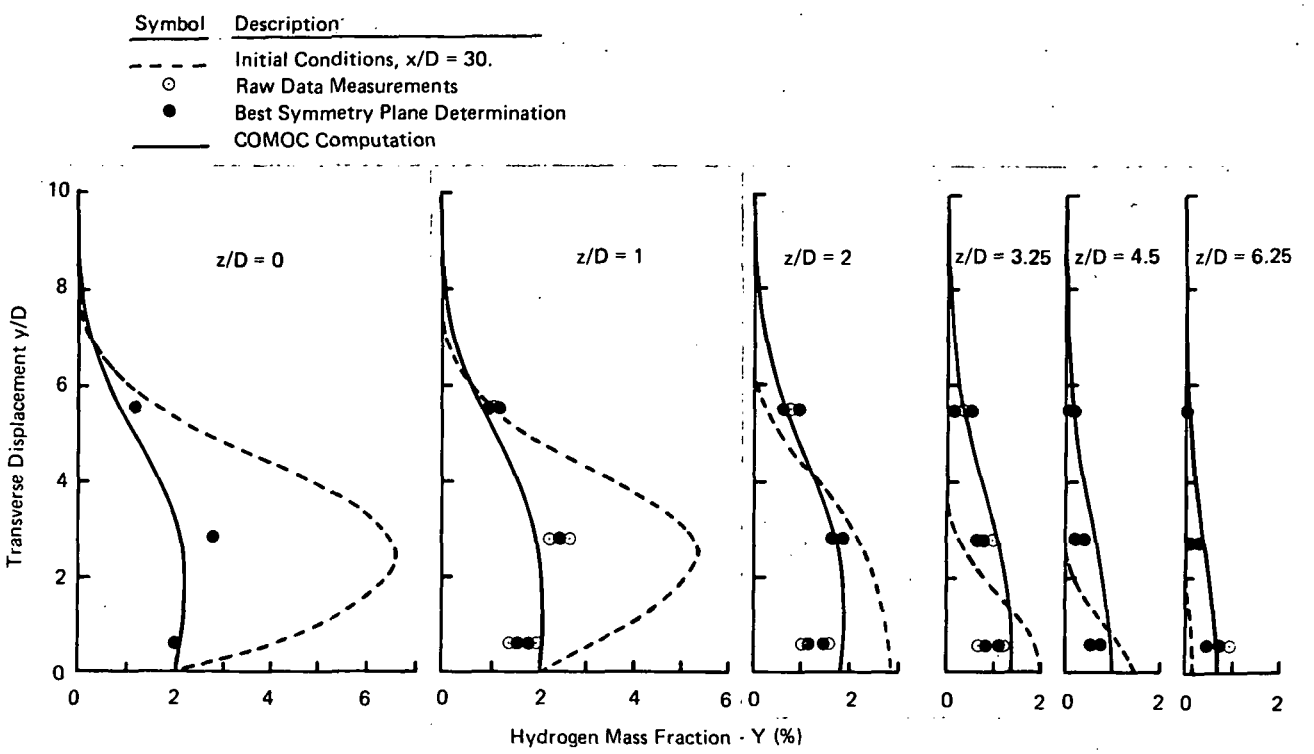

Figure 21. Computed Multi-Jet Hydrogen Mass Fraction Comparison Distribution at Station x/D = 120, q_r= 1

The apparent over-diffusion within the core of the multi-jet configuration may be a reflection of the overall lower hydrogen levels used as initial data. Shown in figure 23 are comparisons of predicted and measured decay of the maximum local hydrogen concentration as a function of x/D for the single- and multiple-jet geometries. The computational curves are essentially parallel; the multiple-jet data are coincident with the single-jet except at x/D=30 where initial conditions were established. The decay of the single jet was accurately predicted by COMOC. The indicated lack of agreement for the multiple jet is perhaps a reflection of differences in initial conditions.

Computational solutions can produce incredible volumes of output data, and integral parameters are often times useful to establish trends. Since the performance prediction of combustion systems is one ultimate goal of design studies, COMOC was adapted to compute the integral "mixing efficiency" parameter, η of reference 6, defined as the percentage of hydrogen that could completely react in a given concentration and velocity distribution within an air boundary layer. For the three-dimensional flow fields considered, η is a point function of longitudinal displacement, x/D. In plane regions that are locally fuel-lean, all the hydrogen could potentially react. In fuel-rich regions,stoichiometry limits the reaction. The "mixing efficiency" is, therefore, the sum of these terms, divided by the total hydrogen available, i.e.,

$$\eta(x) \equiv \frac{\int_{R_I} \rho u Y dy dz + \int_{R_{II}} \rho u R_s (1-Y) dy dz}{\int_{R_I + R_{II}} \rho u Y dy dz} \qquad (51)$$

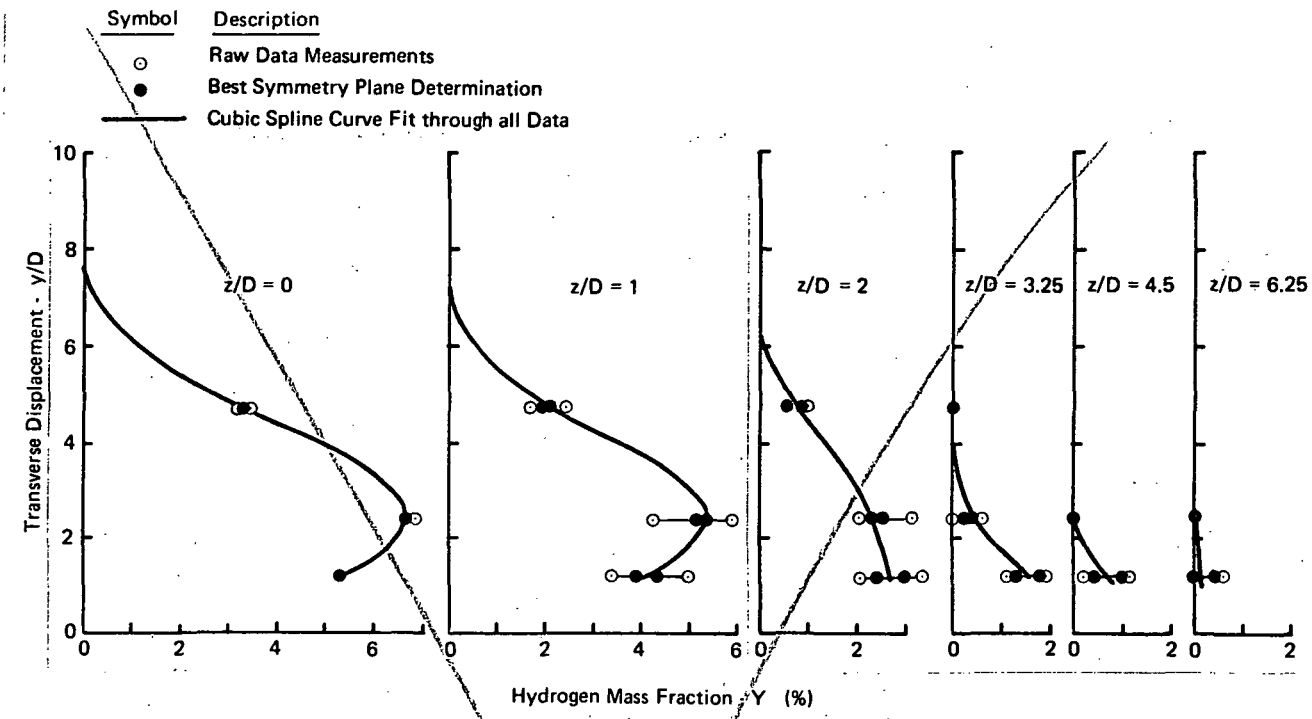

Figure 19. Multi-Jet Hydrogen Mass Fraction Distributions at Station x/D = 30, q_r = 1.0, After Rogers (Ref. 6)

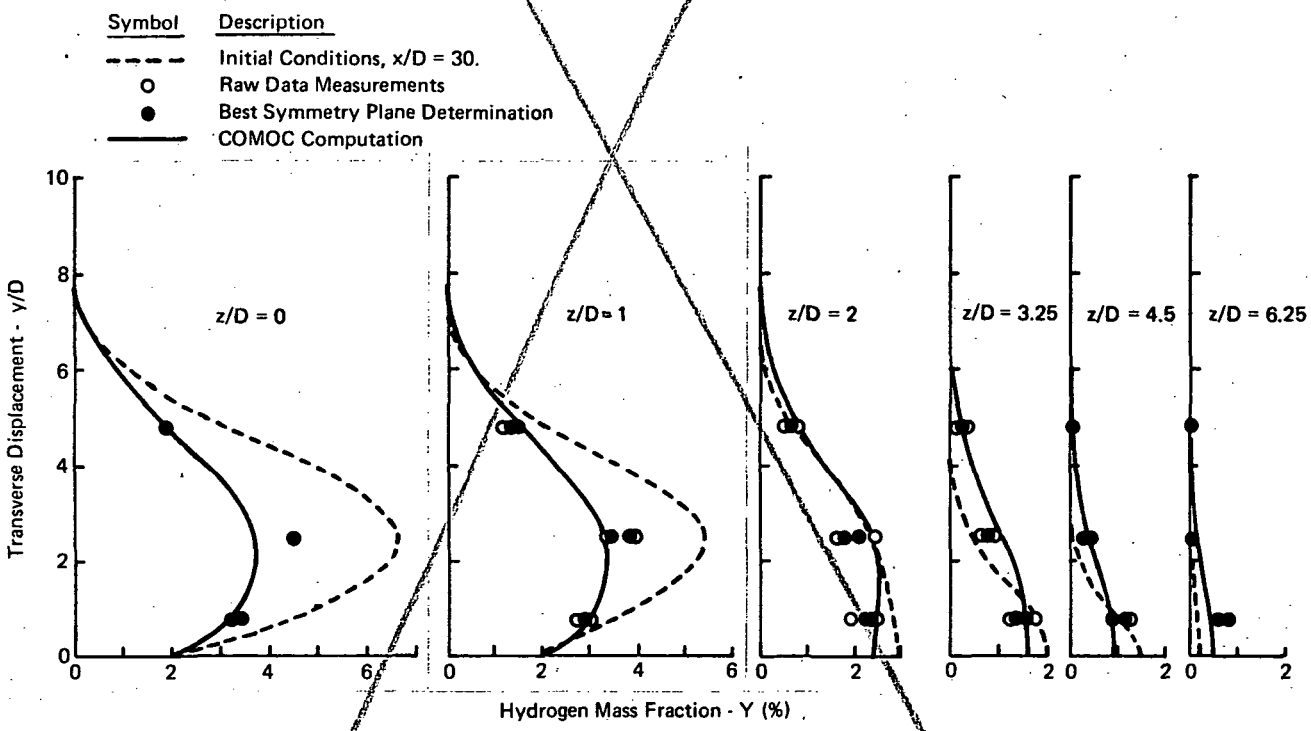

Figure 20. Computed Multi-Jet Hydrogen Mass Fraction Comparison Distribution at Station x/D = 60, q_r = 1

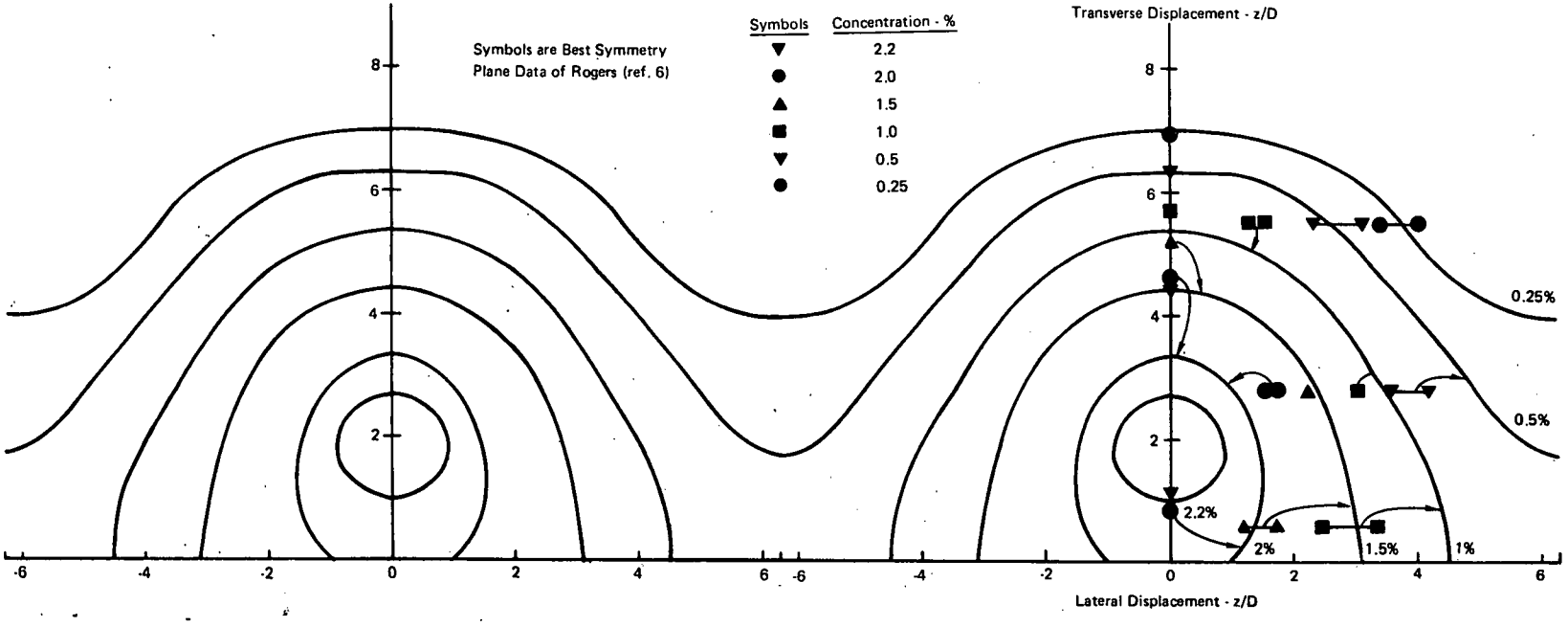

Figure 22. Comparison between COMOC-Computed Mass Fraction Contours and Experimental Data for Multiple-Jet, x/D = 120, q_r = 1.0

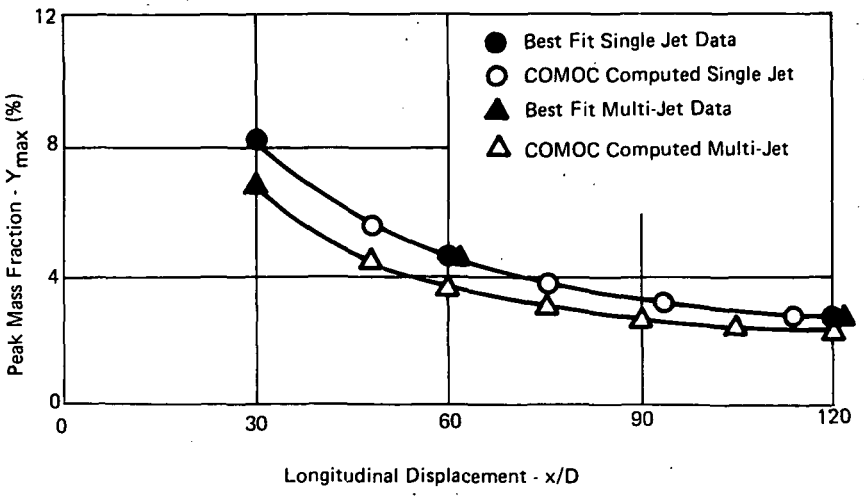

Figure 23. Downstream Decay of Maximum Hydrogen Concentration for Single and Multiple-Jet Transverse Injection

Regions I and II are respectively fuel-lean and fuel-rich, and R_S (=0.029) is the stoichiometric mixture ratio for the hydrogen/air system. Note that the denominator of equation (51) represents total hydrogen flow rate, evaluation of which is discussed in detail in Appendix A. Equation (51) is readily evaluated as a summation over the finite elements of the discretization, as

$$\eta(x) = \sum_{m=1}^{M} \eta_m(x) \tag{52}$$

Determination of region I or II dependence is made on an averaged Y concentration basis within each finite element.

COMOC evaluates equation (52) at each output station. Shown in figure 24 are computed mixing efficiency distributions for the single- and multiple-jet configuration. The multiple-jet efficiency lies uniformly higher than the single jet, as a direct consequence at least of overall lower hydrogen concentration levels starting with the data for initial conditions (see fig. 23). The indicated 15% relative mixing improvement of the multiple jet by station x/D=85 may also be influenced by discretization and initial condition differences. The "virtual source" studies, discussed in the next section, circumvent these difficulties by providing a uniform basis for relative comparison.

Since equation (51) is a relative measure, it should be rather insensitive to computed conservation phenomena. For both cases, the numerical evaluation of the denominator of equation (51) indicated about an 8% computational hydrogen flow loss by x/D=60, with an additional 10% loss accruing by x/D=120. As discussed in Appendix A, these apparent losses appear acceptable in terms of computed solution accuracy for the present study. They may likely become unacceptable for assessing more accurate mixing model hypotheses. A finer solution domain discretization, proven to increase solution accuracy (see Appendix A) should then be used.

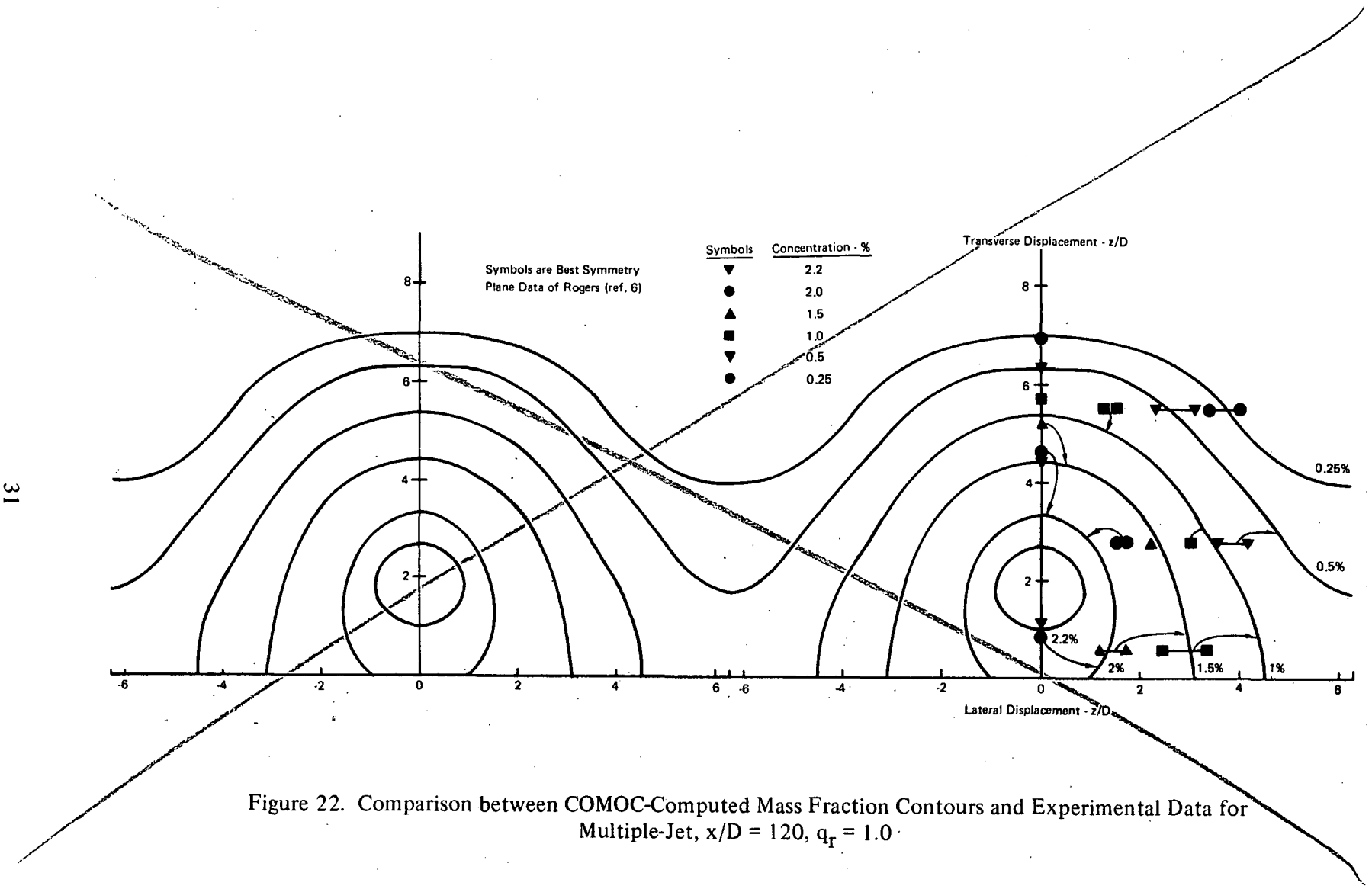

Figure 22. Comparison between COMOC-Computed Mass Fraction Contours and Experimental Data for Multiple-Jet, x/D = 120, q_r = 1.0

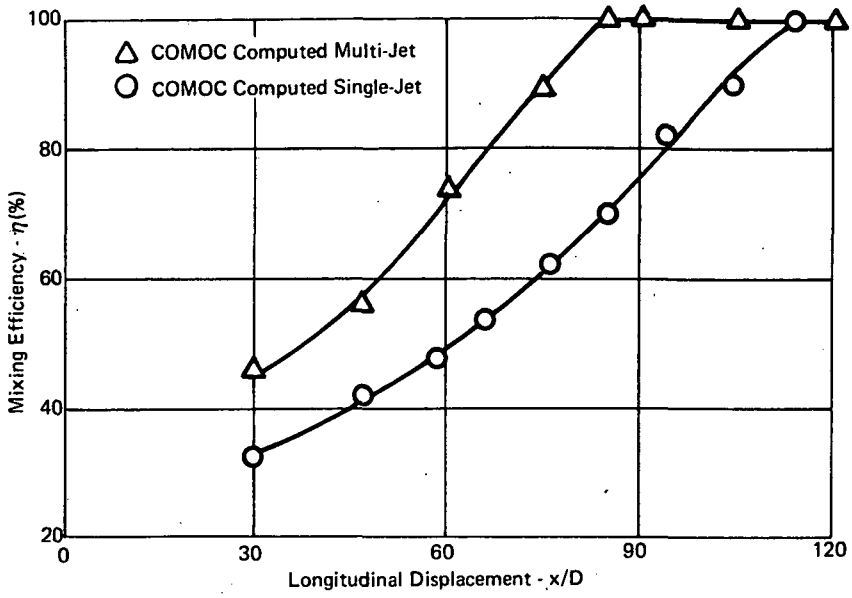

Figure 24. Computed Mixing Efficiency for Single and Multiple Transverse Injection

Evaluation of a "Virtual Source" Concept

The discussed results for single- and multiple-jet injection geometries indicate that the prototype turbulence model has captured at least the essential character of binary mixing within this three-dimensional boundary layer flow. However, it is equally evident that initial conditions do exert a strong influence on computed results for each distinct configuration. Starting computational solutions from a "similarity" condition is an alternative to use of initial data, and one candidate method for the present study is a "virtual source". Within this concept, the complex transverse injection phenomena is computationally replaced by a hydrogen jet imbedded within the air boundary layer flow, the distinguishing features of which are solely dependent upon freestream and injectant parameters. Exploratory results for a subsonic configuration, similar to the single-jet geometry, are discussed in reference 29.

A theoretical model for establishing initial conditions for a virtual source was derived. The model captures the essence of the barrel shock-Mach disk hypothesis for injectant-freestream equilibration, (e.g., ref. 25), and the details are discussed in Appendix B. For the present study, the virtual source was established in the plane of injection, i.e., x/D = 0.0, and was assumed to be of elliptical cross-sectional shape and composed of 100% hydrogen. The virtual source mass flow through the ellipse computationally coincided with the hydrogen mass flow rates of Rogers (ref. 5 and 6), for each dynamic pressure ratio q_r. The velocity of the virtual source injectant was uniformly assumed equal to that velocity (1500 ft/sec or 457 m/sec) computed to occur immediately downstream of the Mach disk, and was independent of dynamic pressure ratio. Everywhere exterior to the ellipse, the hydrogen concentration identically vanished. Except for directly above the ellipse, the virtual source was assumed imbedded within the turbulent boundary layer developing in the absence of injection. Above the ellipse, to account for displacement effects of the barrel shock, the air velocity was assumed initially uniform at the freestream value.

Figure 25 is a three-dimensional representation of the initial station velocity surface; the unity hydrogen concentration is imbedded within the centroidal depression. As before, the superimposed grid is the finite element mesh, only one-half of which was computationally required (from symmetry). Shown in figure 26 is the corresponding planar view of the discretization for the multiple-jet configuration (ref. 6). Three dynamic pressure ratios (q_r = 0.5, 1.0, 1.5) were analyzed; the ellipse corresponding to q_r = 1.5 is shown in figure 26. For q_r = 1.0, the reduced size of the injectant region excluded the encircled nodes (fig. 26) while both the encircled and crossed node points were exterior to the virtual source ellipse for the case q_r = 0.5.

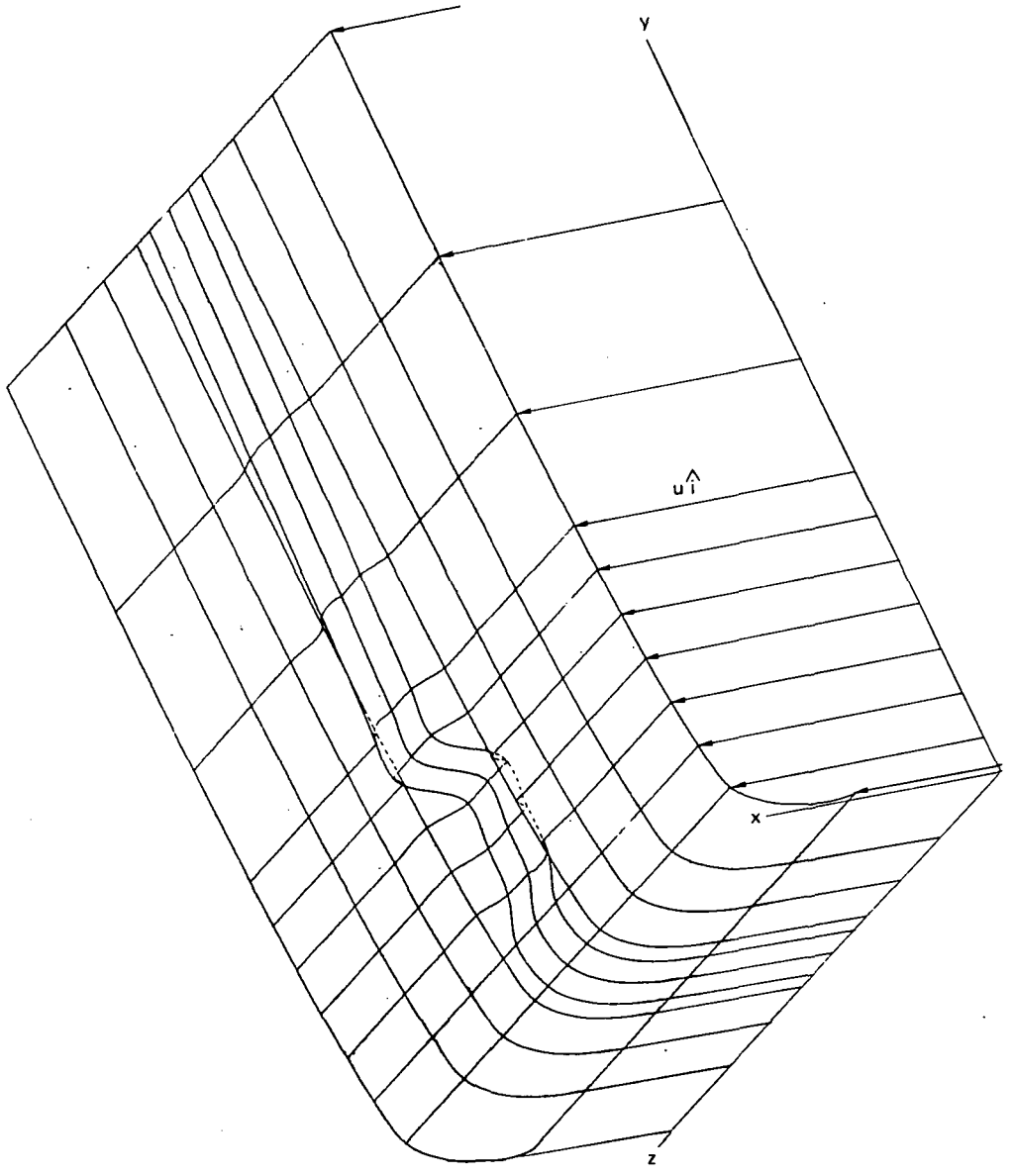

Figure 25. Initial Condition Velocity Surface for Virtual Source Simulation of Transverse Injection

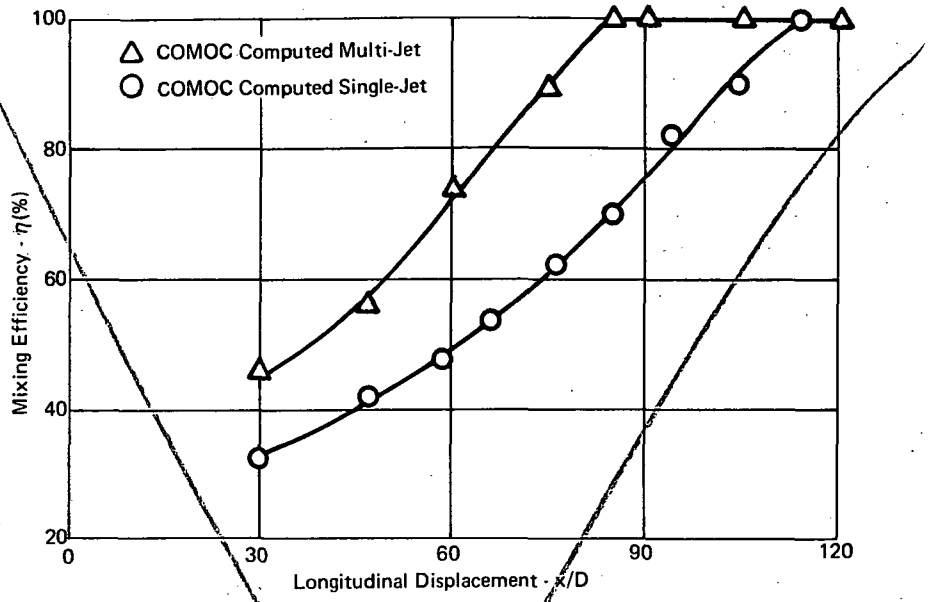

Figure 24. Computed Mixing Efficiency for Single and Multiple Transverse Injection

Evaluation of a "Virtual Source" Concept

The discussed results for single- and multiple-jet injection geometries indicate that the prototype turbulence model has captured at least the essential character of binary mixing within this three-dimensional boundary layer flow. However, it is equally evident that initial conditions do exert a strong influence on computed results for each distinct configuration. Starting computational solutions from a "similarity" condition is an alternative to use of initial data, and one candidate method for the present study is a "virtual source". Within this concept, the complex transverse injection phenomena is computationally replaced by a hydrogen jet imbedded within the air boundary layer flow, the distinguishing features of which are solely dependent upon freestream and injectant parameters. Exploratory results for a subsonic configuration, similar to the single-jet geometry, are discussed in reference 29.

A theoretical model for establishing initial conditions for a virtual source was derived. The model captures the essence of the barrel shock-Mach disk hypothesis for injectant-freestream equilibration, (e.g., ref. 25), and the details are discussed in Appendix B. For the present study, the virtual source was established in the plane of injection, i.e., x/D = 0.0, and was assumed to be of elliptical cross-sectional shape and composed of 100% hydrogen. The virtual source mass flow through the ellipse computationally coincided with the hydrogen mass flow rates of Rogers (ref. 5 and 6), for each dynamic pressure ratio q_r. The velocity of the virtual source injectant was uniformly assumed equal to that velocity (1500 ft/sec or 457 m/sec) computed to occur immediately downstream of the Mach disk, and was independent of dynamic pressure ratio. Everywhere exterior to the ellipse, the hydrogen concentration identically vanished. Except for directly above the ellipse, the virtual source was assumed imbedded within the turbulent boundary layer developing in the absence of injection. Above the ellipse, to account for displacement effects of the barrel shock, the air velocity was assumed initially uniform at the freestream value.

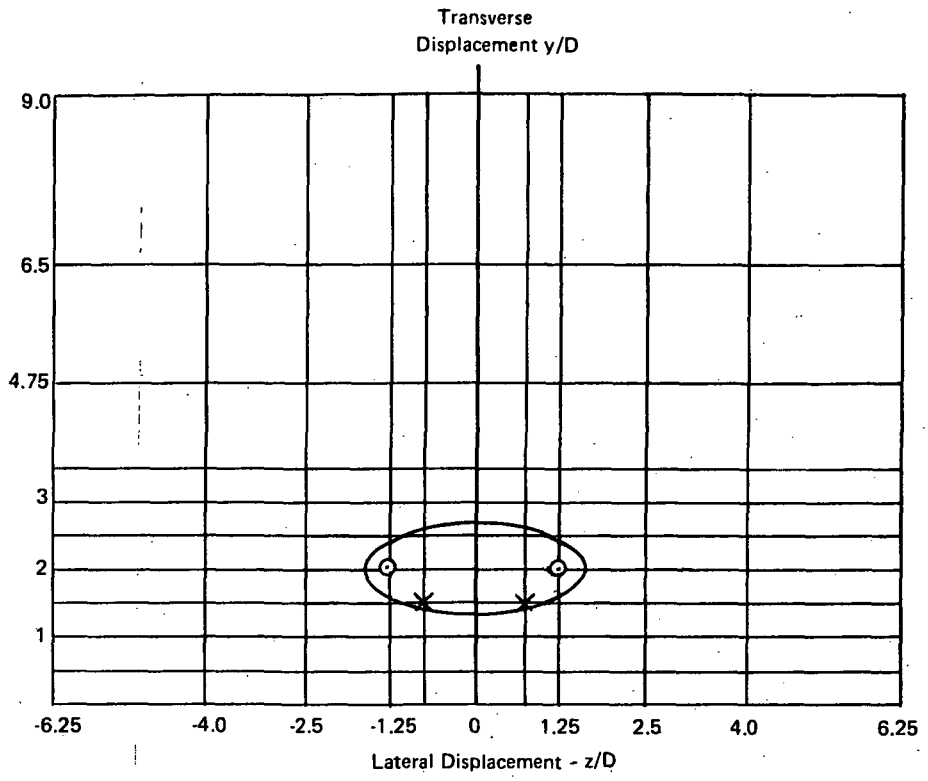

Figure 26 Solution Domain Finite Element Discretization for Virtual Source Studies

The turbulence transport model used for the virtual source study was identical to that previously described, except for minor variations. The mixing length hypothesis was uniformly enforced in the initial region until the minimum velocity in the virtual source depression accelerated to within ~2% of the corresponding velocity without injection. This occurred within 3 to 4 diameters downstream of the injection plane for all q_r. Downstream of x/D = 4, transition from mixing length to mass defect occurred between 0.5 and 1.0 diameters above the plate surface. Due to the relatively small density within the virtual source, the computed mass defect, equation (45), was quite large in the initial downstream region. From extensive experimentation, a smaller constant (K = 0.01, equation (44)) was found to be effective for all three dynamic pressure ratios studied. The turbulent Schmidt number distribution coincided with that of the single- and multiple-jet studies discussed.

Shown in figures 27 through 29 are the results of the virtual source computational simulation of the multiple injection configuration of ref. 6 for dynamic pressure ratios (q_r) of 0.5, 1.0, and 1.5, respectively. Superimposed are appropriate single-jet data from ref. 5, as well as the multiple-jet data. The computational results are compared, in the region of $0 \leqslant x/D \leqslant 60$, on the multiple bases of:

(a) maximum concentration level of hydrogen at x/D

(b) trajectory of the maximum hydrogen concentration level (i.e., transverse displacement above the plate of the local maximum hydrogen level)

(c) lateral spreading of the jet as determined by the z/D coordinate of the hydrogen concentration equal to 10% of the local maximum level.

The computed mixing efficiency parameter η, equation (48), completes each data set. Listed in table 3 are the parameters pertinent to each solution, the downstream integration station at which COMOC automatically switched from the mixing length to mass defect model within the jet region, and the total CPU execution time for the IBM 360/65 computer.

TABLE 3
PARAMETERS FOR THE VIRTUAL SOURCE COMPUTATIONS,
$M_\infty = 4.57$

Dynamic Pressure Ratio, q_r	Virtual Source Flow Area (Square Orifice Diameters)		Downstream Station, x/D, for Core Region Mass Defect [3]	CPU Time Seconds [4]
	Ref. 5 [1]	COMOC [2]		
0.5	2.28	2.22	4.13	916.
1.0	2.72	2.94	3.53	943.
1.5	4.08	3.48	4.04	1111.

[1] Initial elliptical cross sectional area required to match test injection conditions of reference 5.

[2] Numerical approximation to conditions of reference 5.

[3] Automatically established at first integration station past a user-specified value of x/D.

[4] Single precision on IBM 360/65 computer.

The agreement of the computed solutions with data, for $q_r = 0.5$ and 1.0, is quite good (maximum deviation $\sim$ 20%) on all comparison bases. Poorer (40% deviation) agreement with the data occurs at $q_r = 1.5$, (fig. 29) on both trajectory and lateral spreading. This dynamic pressure ratio produces a "stiffer" jet, the influence of which is especially noticeable within the region $0 \leqslant x/D \leqslant 30$, for the illustrated solution differences on both trajectory and maximum concentration. The lateral spreading disagreement may result primarily from the relatively undersized initial condition ellipse, (table 3). This could have been readily corrected by initial condition and discretization changes, but the uniform comparison basis of the computations for the three values of q_r would then have been disturbed.

Agreement between the COMOC virtual source computations and experimental data indicates a potential value for practical design studies. In providing such support, it is significantly important that arbitraty parameters were set uniformly constant for each q_r case, as distinct from fine tuning each computation to match specific data sets. It is thus possible to directly compare the results of computation without significant interpretation. As opposed to scrutiny of comparative flow field details, the valuable design criteria may well be the mixing efficiency comparison previously shown in figure 1. Since combustion systems are of ultimate interest, and if the reaction is fast (hence diffusion controlled), the computation of mixing efficiency on a cold flow basis may provide some degree of design guidance for hardware development. These reported results are representative of an initial theoretical study; certainly, with the refinements that are possible in modeling and the significant versatility of the developing COMOC system, analytical support to design optimization appears practical.

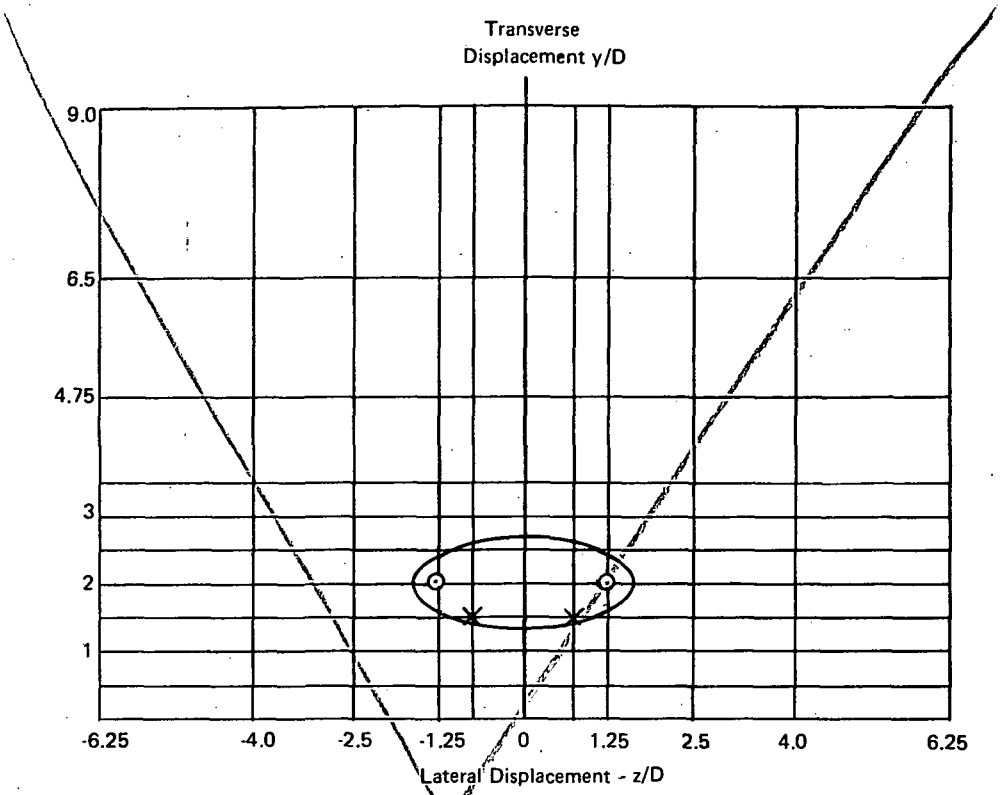

Figure 26 Solution Domain Finite Element Discretization for Virtual Source Studies

The turbulence transport model used for the virtual source study was identical to that previously described, except for minor variations. The mixing length hypothesis was uniformly enforced in the initial region until the minimum velocity in the virtual source depression accelerated to within ~2% of the corresponding velocity without injection. This occurred within 3 to 4 diameters downstream of the injection plane for all q_r. Downstream of x/D = 4, transition from mixing length to mass defect occurred between 0.5 and 1.0 diameters above the plate surface. Due to the relatively small density within the virtual source, the computed mass defect, equation (45), was quite large in the initial downstream region. From extensive experimentation, a smaller constant (K = 0.01, equation (44)) was found to be effective for all three dynamic pressure ratios studied. The turbulent Schmidt number distribution coincided with that of the single- and multiple-jet studies discussed.

Shown in figures 27 through 29 are the results of the virtual source computational simulation of the multiple injection configuration of ref. 6 for dynamic pressure ratios (q_r) of 0.5, 1.0, and 1.5, respectively. Superimposed are appropriate single-jet data from ref. 5, as well as the multiple-jet data. The computational results are compared, in the region of $0 \leqslant x/D \leqslant 60$, on the multiple bases of:

(a) maximum concentration level of hydrogen at x/D

(b) trajectory of the maximum hydrogen concentration level (i.e., transverse displacement above the plate of the local maximum hydrogen level)

(c) lateral spreading of the jet as determined by the z/D coordinate of the hydrogen concentration equal to 10% of the local maximum level.

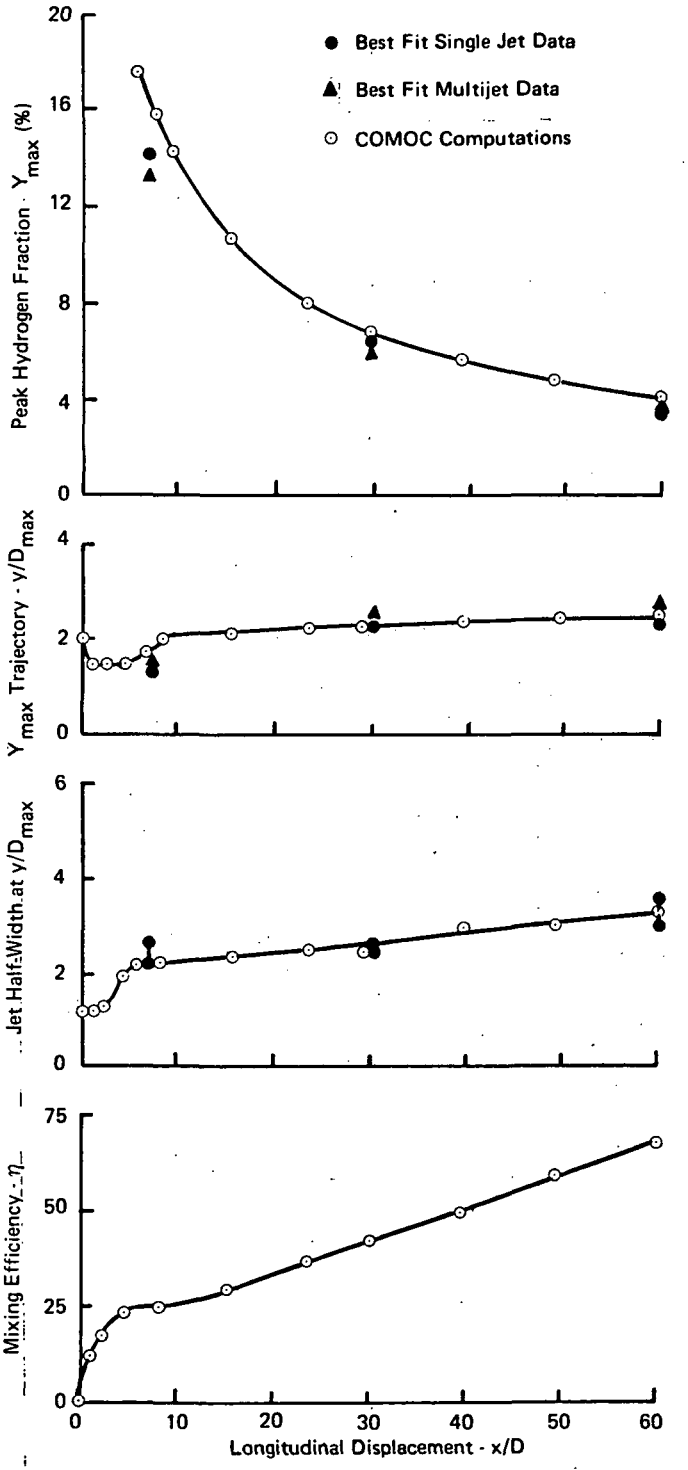

Figure 27. COMOC Predictions for Virtual Source, $q_r = 0.5$

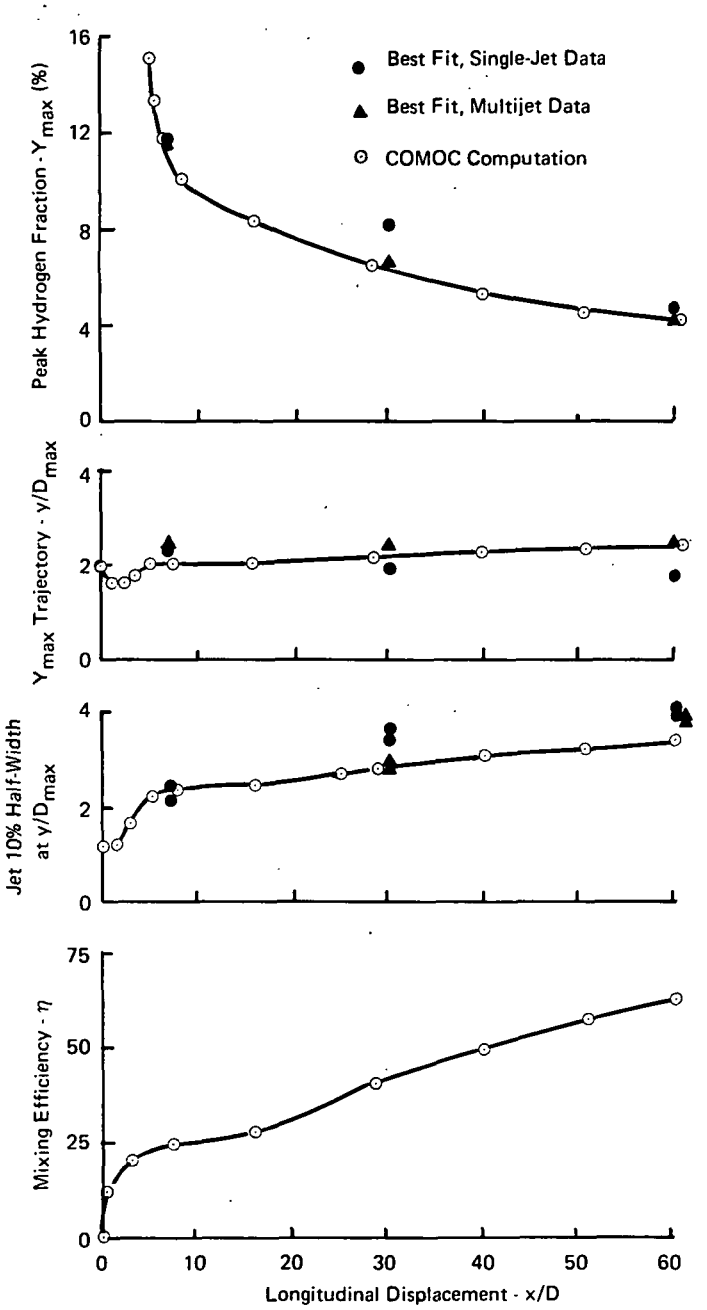

Figure 28 COMOC Predictions for Virtual Source, $q_r = 1$

Scramjet combustor systems that may not be predominantly diffusion controlled are certainly conceivable. For practical design studies it then becomes necessary to perform computations for finite rate or equilibrium controlled combustion systems to establish a data base, as well as to validate the usefulness of mixing efficiency computations from cold flow studies. The COMOC program system is readily extensible to analysis of combustion systems by addition of state-of-the-art kinetics packages, in the same direct manner that the turbulent transport subroutine was adapted from an operational two-dimensional finite difference computer program. This program (NUMINT) was extensively utilized as well, for the accuracy and convergence determination of COMOC solutions, using the single-jet centerplane data of Rogers (ref. 5) as an initial condition (refer to Appendix A).

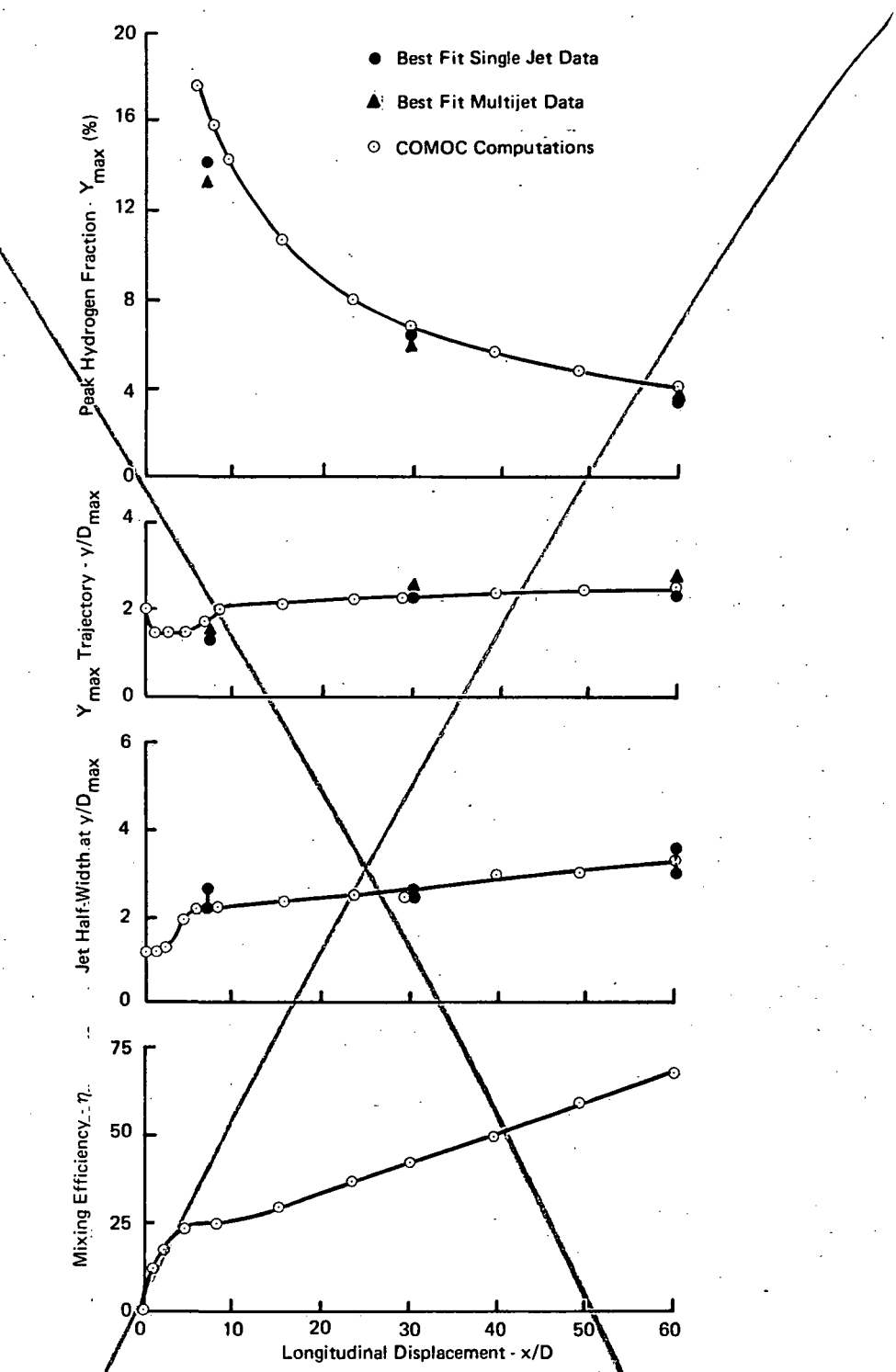

Figure 27. COMOC Predictions for Virtual Source, $q_r = 0.5$

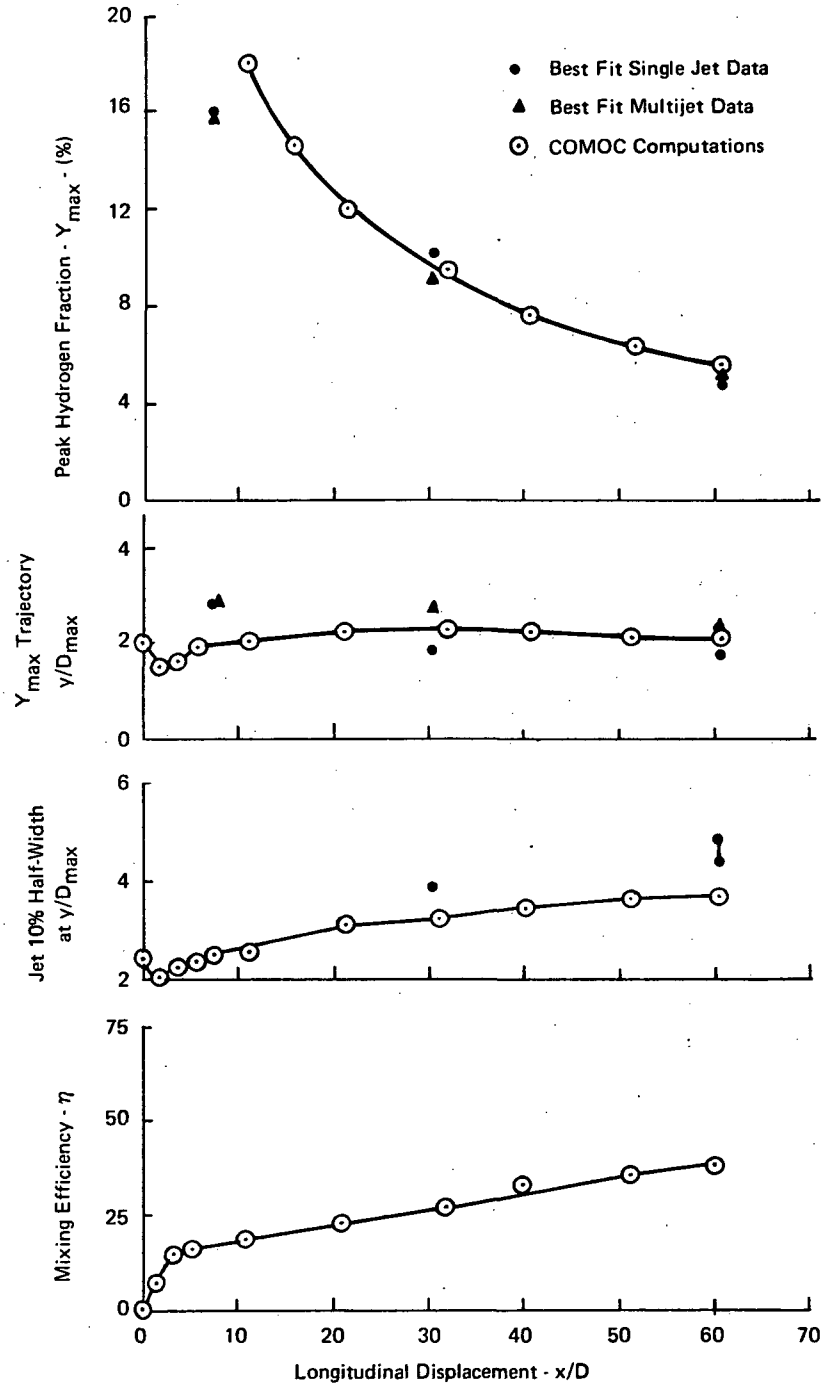

Figure 29. COMOC Predictions for Virtual Source, q_r= 1.5

To illustrate the near term potential of a practical combustion calculation capability, the temperature of these same initial data was elevated to autoignition, and the centerplane run repeated with finite rate combustion occurring. Shown in figure 30 are the computed hydrogen mass fraction distributions at x/D = 30 for the chemically reacting system and a comparison frozen flow computation as well as the initial distribution at x/D = 7.

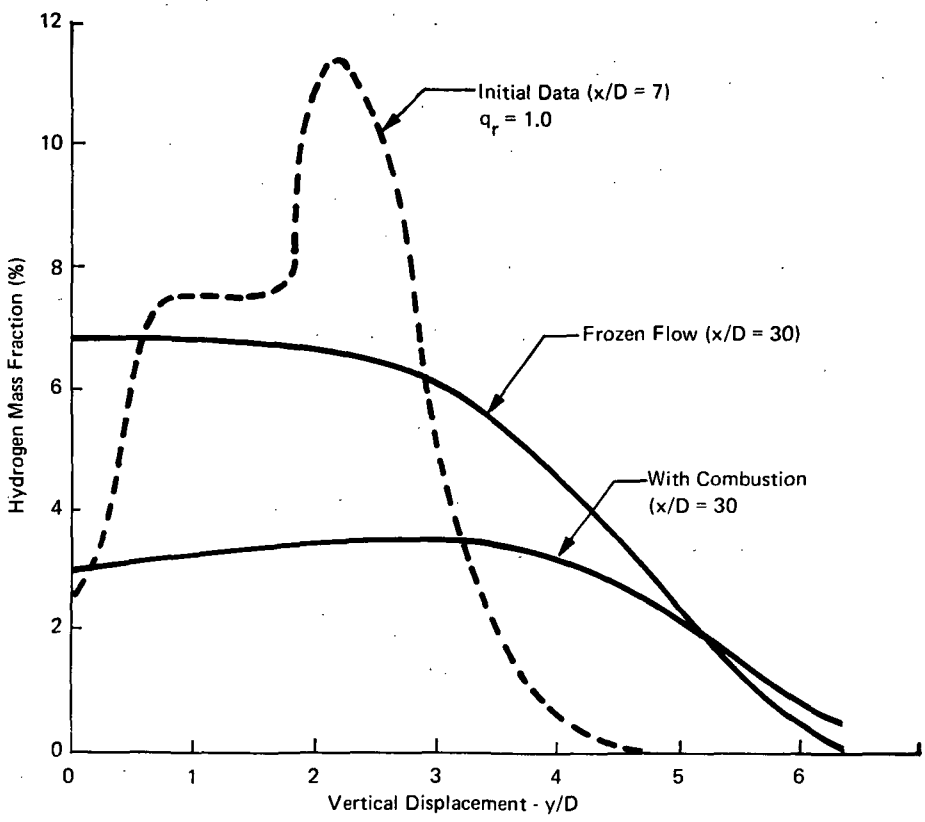

Figure 30. Predicted Hydrogen Mass Fraction Distributions at x/D = 30 Using Experimental Centerplane Initial Data of Rogers (ref.5)

These computations serve to illustrate the operational capability for numerical analysis in chemically reacting systems. Since subroutines are easily adapted for use by COMOC (as a consequence of its modular structure), a combustion calculation capability for practical three-dimensional flow fields could be readily established by borrowing from the state of the art. The prospect for practical design guidance of complex combustors thus appears achievable in the near term, and COMOC would benefit directly from accrued pertinent experience, in particular, the quasi-linearation approach of Morretti (ref. 30), used in conjunction with the implicit integration algorithm of Tyson and Kliegel (ref. 31). These important features are a part of the kinetics analysis capability (ref. 32) producing the example results.

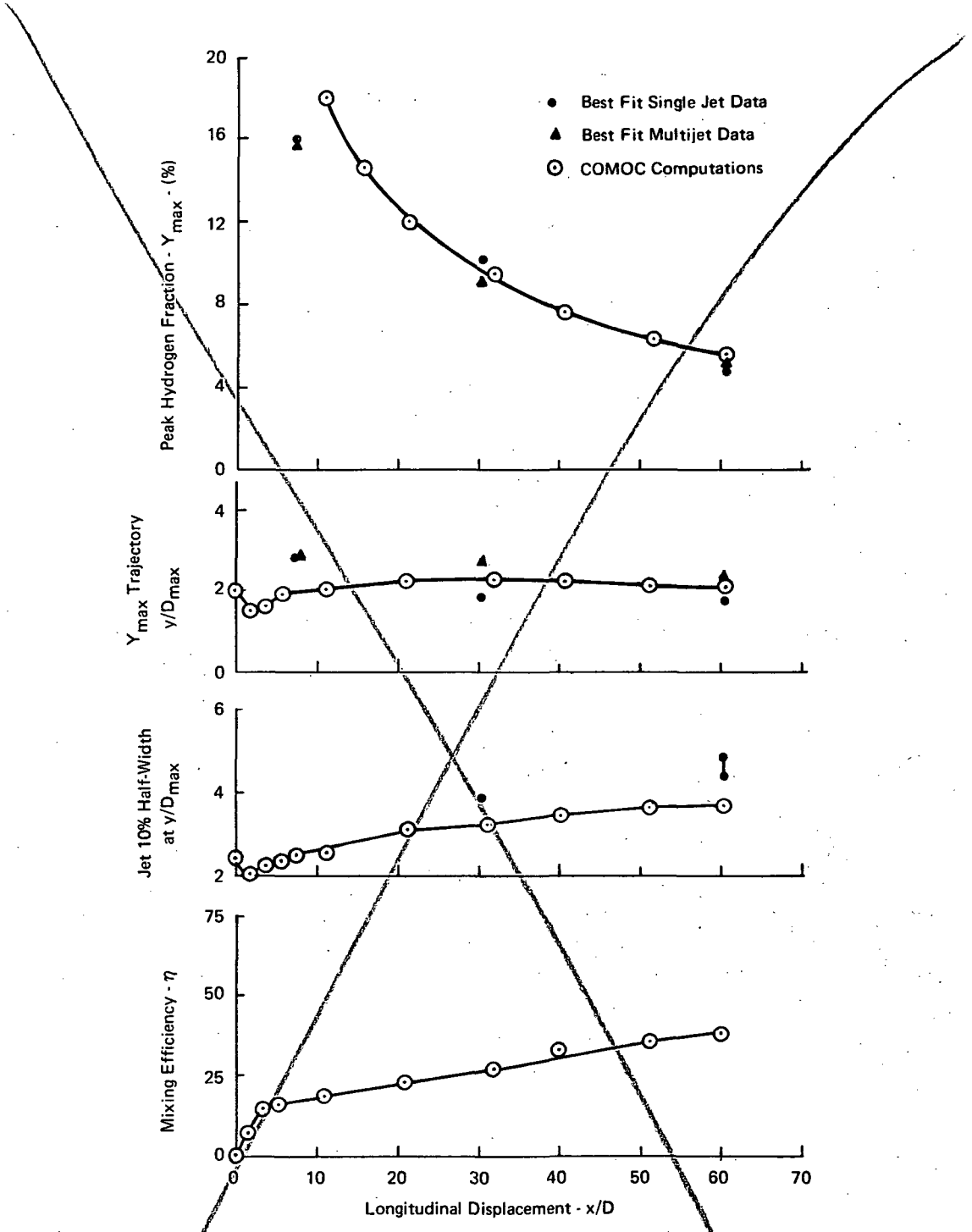

Figure 29. COMOC Predictions for Virtual Source, q_r= 1.5

To illustrate the near term potential of a practical combustion calculation capability, the temperature of these same initial data was elevated to autoignition, and the centerplane run repeated with finite rate combustion occurring. Shown in figure 30 are the computed hydrogen mass fraction distributions at x/D = 30 for the chemically reacting system and a comparison frozen flow computation as well as the initial distribution at x/D = 7.

CONCLUDING REMARKS

A theoretical and analytical study has been made of mixing in the three-dimensional, turbulent boundary layer-type flow field downstream of transverse injection. Numerical solutions of the flow field equations were achieved using a general purpose computer program (COMOC) founded upon a finite element solution algorithm. Computations using a turbulent transport model based on mass defect and mixing length concepts, in conjunction with a geometrically defined turbulent Schmidt number, yielded reasonable comparisons with experimental data for both single and multiple injector geometric configurations. Refinement of the model is certainly required before any generality may be assigned to it.

Detailed characterization of the complex three-dimensional flow field has resulted from this analytical study. The concept of a virtual source was evaluated successfully, and mixing efficiency computations were illustrated as potentially useful for support of engineering design studies. Of major consequence may be the observation that agreement with data occurred only for the locally frozen hydrogen concentration boundary condition directly beneath the jet centroid. This isolation from the wall may well exert great influence on combustor design and operation.

It is clear that the controlling physics of such phenomena cannot be established by numerical observation alone. However, the COMOC computer program system, with its demonstrated flexibility and versatility, may have considerable impact on the bringing together of the present and next generation of digital computers with the engineer and designer. The theoretician will certainly receive guidance in his work using a versatile computational capability as his laboratory, whereas the experimentalist can employ the computer to ascertain flow regions requiring especially detailed measurements by rapid comparison of data and computations.

"Page missing from available version"

APPENDIX A

ACCURACY AND CONVERGENCE OF THE FINITE ELEMENT SOLUTION ALGORITHM IN COMOC

Favorable evaluation of numerical accuracy, and convergence with discretization, of a COMOC-generated finite element solution for the two-dimensional steady Navier-Stokes equations is reported (ref. 15). Accuracy and convergence for the transient intergration of the finite element solution algorithm for heat conduction is proven (ref. 13). This Appendix discusses results which establish a favorable assessment of COMOC-generated solution accuracy and convergence for boundary layer flow of a compressible fluid.

Comparison solutions were generated using an operational finite difference computer program (NUMINT) which integrates the equations governing multi-component mixing and reaction of compressible, two-dimensional and axisymmetric boundary layer flow, cast in the von Mises coordinate system. The use of derived variables in NUMINT, as distinct from the physical variables of COMOC, renders available two completely independent methods for solution of the governing equation system. NUMINT has been extensively evaluated, and is in everyday use for prediction of practical mixing and reacting compressible boundary layer flow fields.

The symmetry plane, parallel to the freestream velocity vector and bisecting the injection orifice, figure 2 was selected as the sample comparison solution domain, since NUMINT is constrained to two-dimensional problems. The three-dimensional capability of COMOC was numerically reduced to two by enforcing vanishing gradient boundary conditions on all dependent variables on two planes, z = ± constant, and prescribing initial conditions that were independent of z, i.e., uniform across the discretization. By this procedure, COMOC was independently assessed to preserve two-dimensionality within about ±2% by application only of this non-rigid boundary condition statement.

The single jet centerplane data of Rogers (ref. 5), for $q_r = 1.0$ and at Station x/D = 7, was selected as the initial condition for longitudinal velocity, u, and hydrogen mass fraction, Y. The cross flow velocity, w, was set uniformly to zero, and COMOC started computations for transverse mass flow ρv after sufficient data were generated to allow approximation of $\{\rho U\}'$, equation (31). Vanishing normal gradient boundary conditions were applied on the closure of the elliptic domain except for enforcing no-slip at the plate surface. Computations were carried to Station x/D = 30, and to stimulate strong mixing and to control parameter variation, a constant turbulent eddy mass mixing coefficient was specified, and the Schmidt Number was set constant throughout, equal to 0.7.

Shown in figure A.1 are comparison COMOC and NUMINT computed solutions for hydrogen mass fraction distribution through the boundary layer thickness at Station x/D = 30. Extensive diffusion and convection has occurred, as illustrated by comparison to the initial distribution (x/D = 7). A one-to-one-correspondence exists between COMOC data points and the discretization through the boundary layer thickness. The curve is faired through the square COMOC symbols corresponding to the 22 finite element discretization. Agreement with the 100 zone finite difference NUMINT solution is excellent, with only the values of Y near the wall being computed as measureably different. NUMINT employs a four-point finite difference derivative formula to evaluate Y at the wall to enforce the vanishing gradient

boundary condition. COMOC, of course, handles Y at the wall in a fashion identical to interior node points, resulting in simultaneous evaluation of the wall value of Y with the interior solution. The small computed differences might well stem from the distinctly different methods for handling such boundary conditions.

The important proof of convergence with discretization is also illustrated in figure A.1. The open circles correspond to the COMOC solution using a very coarse 13-finite element discretization. Agreement with the 22-element solution is amazingly good, especially when considering that the initial peak Y distribution at Station x/D = 7 was captured at only one node. More importantly, the 13-element solution is observed to depart from the 22-element solution in directions diametrically opposite to that of the 100-zone finite difference solution. A 50-zone finite difference solution, also generated by NUMINT, agreed almost exactly with the 100-zone solution, except at the plate surface, where the inverted triangle data points confirm the identical solution diametric departure trend observed. From the mathematics standpoint, since the finite difference solution algorithm is amply proven to converge with discretization, the same property can be ascribed to the finite element algorithm. From the practical analysis viewpoint, the excellent solution accuracy for the 13-finite element discretization indicates the ability to employ rather coarse discretizations, and yet obtain adequately accurate numerical solutions for practical problems. Additional detail on this subject is presented in reference 13.

The comparison of the computed longitudinal velocity distributions is shown in figure A.2. A strong retardation of the flow is indicated, by comparison to the initial velocity distribution, and negligible differences exist between the COMOC and NUMINT solutions for 22-finite elements and 100-zone finite difference, respectively. The COMOC solution for the 13-element discretization was essentially identical to the 22-element case.

Two versions of a global continuity equation solver are operational in COMOC. The finite element approximation produces polynomials in the y coordinate only, and analytic integration of the solution algorithm, equation (30), is directly obtained. The distinctive feature of the two algorithms is the finite element approximation to the longitudinal mass flux dependent variable derivative vector $\{\rho U\}'$, equation (31). Both running-smoothing polynomial representations, over sequential panels of data, and cubic spline fits over the entire data field have yielded excellent results. Shown in figure A.3 is the comparison between COMOC-generated solutions using quadratic running-smoothing (over three data points) and the cubic spline, for transverse mass flux distribution, ρV, obtained for the axisymmetric companion problem to center plane mixing parallel hydrogen injection into a supersonic air stream. The identical radial distribution of $\{\rho U\}'$ was used for each case, and agreement between the solutions is excellent. Slight underprediction by NUMINT, in the back flow region, just off the flow centerline is indicated. This may result from large truncation errors associated with numerical differentiation of streamline data over a fine discretization near the flow centerline.

An important and independent assessment of computed solution accuracy is numerical evaluation of properties of the flow field that would be rigorously conserved if an analytic solution to the governing differential equation system could be achieved. As an example, the species continuity equation for hydrogen mass fraction, equation (4), can be written in explicit conservation form, using the three-dimensional gradient operator ∇, as

$$\nabla \cdot \left(\rho \vec{U} Y - \frac{\mu Le}{Pr} \nabla_2 Y\right) = 0 \qquad (A.1)$$

APPENDIX A

ACCURACY AND CONVERGENCE OF THE FINITE ELEMENT SOLUTION ALGORITHM IN COMOC

Favorable evaluation of numerical accuracy, and convergence with discretization, of a COMOC-generated finite element solution for the two-dimensional steady Navier-Stokes equations is reported (ref. 15). Accuracy and convergence for the transient intergration of the finite element solution algorithm for heat conduction is proven (ref. 13). This Appendix discusses results which establish a favorable assessment of COMOC-generated solution accuracy and convergence for boundary layer flow of a compressible fluid.

Comparison solutions were generated using an operational finite difference computer program (NUMINT) which integrates the equations governing multi-component mixing and reaction of compressible, two-dimensional and axisymmetric boundary layer flow, cast in the von Mises coordinate system. The use of derived variables in NUMINT, as distinct from the physical variables of COMOC, renders available two completely independent methods for solution of the governing equation system. NUMINT has been extensively evaluated, and is in everyday use for prediction of practical mixing and reacting compressible boundary layer flow fields.

The symmetry plane, parallel to the freestream velocity vector and bisecting the injection orifice, figure 2 was selected as the sample comparison solution domain, since NUMINT is constrained to two-dimensional problems. The three-dimensional capability of COMOC was numerically reduced to two by enforcing vanishing gradient boundary conditions on all dependent variables on two planes, z = ± constant, and prescribing initial conditions that were independent of z, i.e., uniform across the discretization. By this procedure, COMOC was independently assessed to preserve two-dimensionality within about ±2% by application only of this non-rigid boundary condition statement.

The single jet centerplane data of Rogers (ref. 5), for $q_r = 1.0$ and at Station x/D = 7, was selected as the initial condition for longitudinal velocity, u, and hydrogen mass fraction, Y. The cross flow velocity, w, was set uniformly to zero, and COMOC started computations for transverse mass flow ρv after sufficient data were generated to allow approximation of $\{\rho U\}'$, equation (31). Vanishing normal gradient boundary conditions were applied on the closure of the elliptic domain except for enforcing no-slip at the plate surface. Computations were carried to Station x/D = 30, and to stimulate strong mixing and to control parameter variation, a constant turbulent eddy mass mixing coefficient was specified, and the Schmidt Number was set constant throughout, equal to 0.7.

Shown in figure A.1 are comparison COMOC and NUMINT computed solutions for hydrogen mass fraction distribution through the boundary layer thickness at Station x/D = 30. Extensive diffusion and convection has occurred, as illustrated by comparison to the initial distribution (x/D = 7). A one-to-one-correspondence exists between COMOC data points and the discretization through the boundary layer thickness. The curve is faired through the square COMOC symbols corresponding to the 22 finite element discretization. Agreement with the 100 zone finite difference NUMINT solution is excellent, with only the values of Y near the wall being computed as measureably different. NUMINT employs a four-point finite difference derivative formula to evaluate Y at the wall to enforce the vanishing gradient

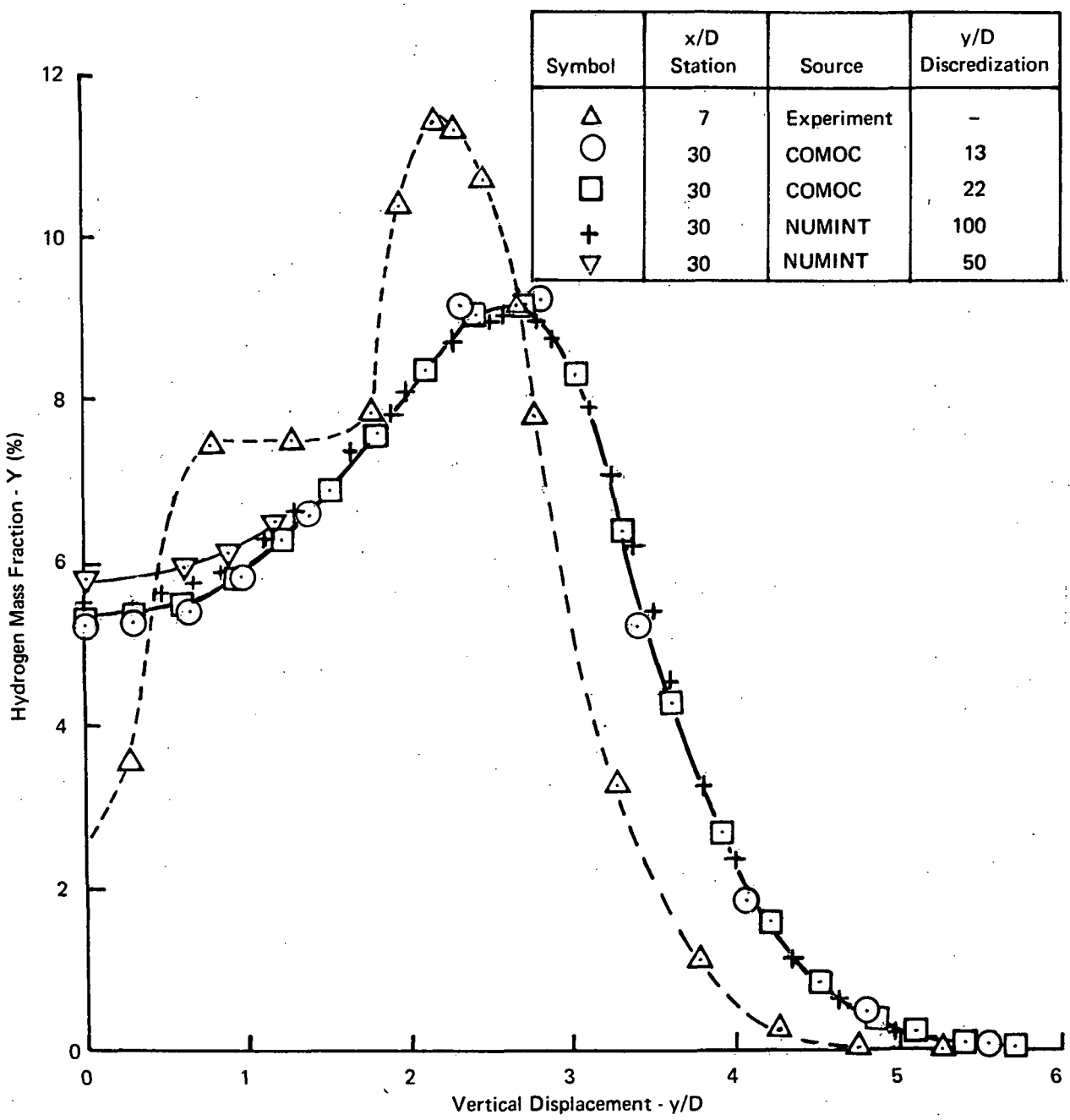

Figure A.1. Comparison Computed Hydrogen Mass Fraction Distributions on Symmetry Centerplane of Mixing Region

Identify a three-dimensional, rectangular parallelepiped control volume, figure A.4, with sides normal to coordinate directions. Employ Gauss' theorem to recast equation (A.1) as a surface integral over this control volume:

$$\oiint [\rho \vec{U} Y - \frac{\mu Le}{Pr} \nabla_2 Y] \cdot \hat{n} d\sigma = 0 \qquad (A.2)$$

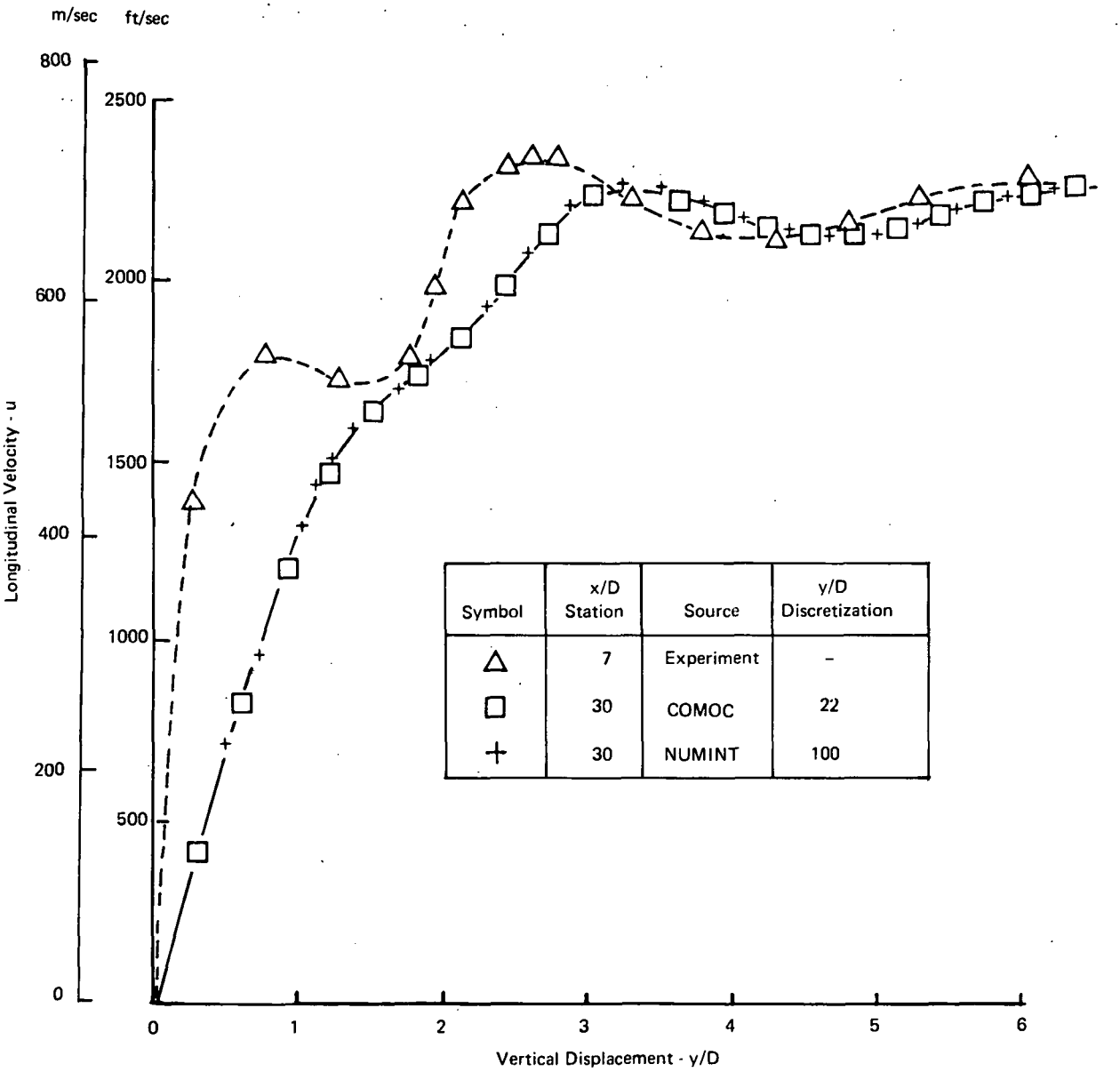

Figure A.2. Comparison Computed Longitudinal Velocity Distributions on Symmetry Centerplane of Mixing Region

Integrand evaluation over the subject control volume yields, alternatively,

$$\int_B \rho u Y d\sigma - \int_A \rho u Y d\sigma + \int_D \rho v Y d\sigma$$

$$- \left[\int_C \frac{\mu Le}{Pr} Y_{,z} d\sigma + \int_D \frac{\mu Le}{Pr} Y_{,y} d\sigma + \int_F \frac{\mu Le}{Pr} Y_{,y} d\sigma \right] = 0 \qquad (A.3)$$

In equation (A.3), the integral subscripts identify control volume surfaces, and the symmetry properties on face E and the no slip wall have been accounted for.

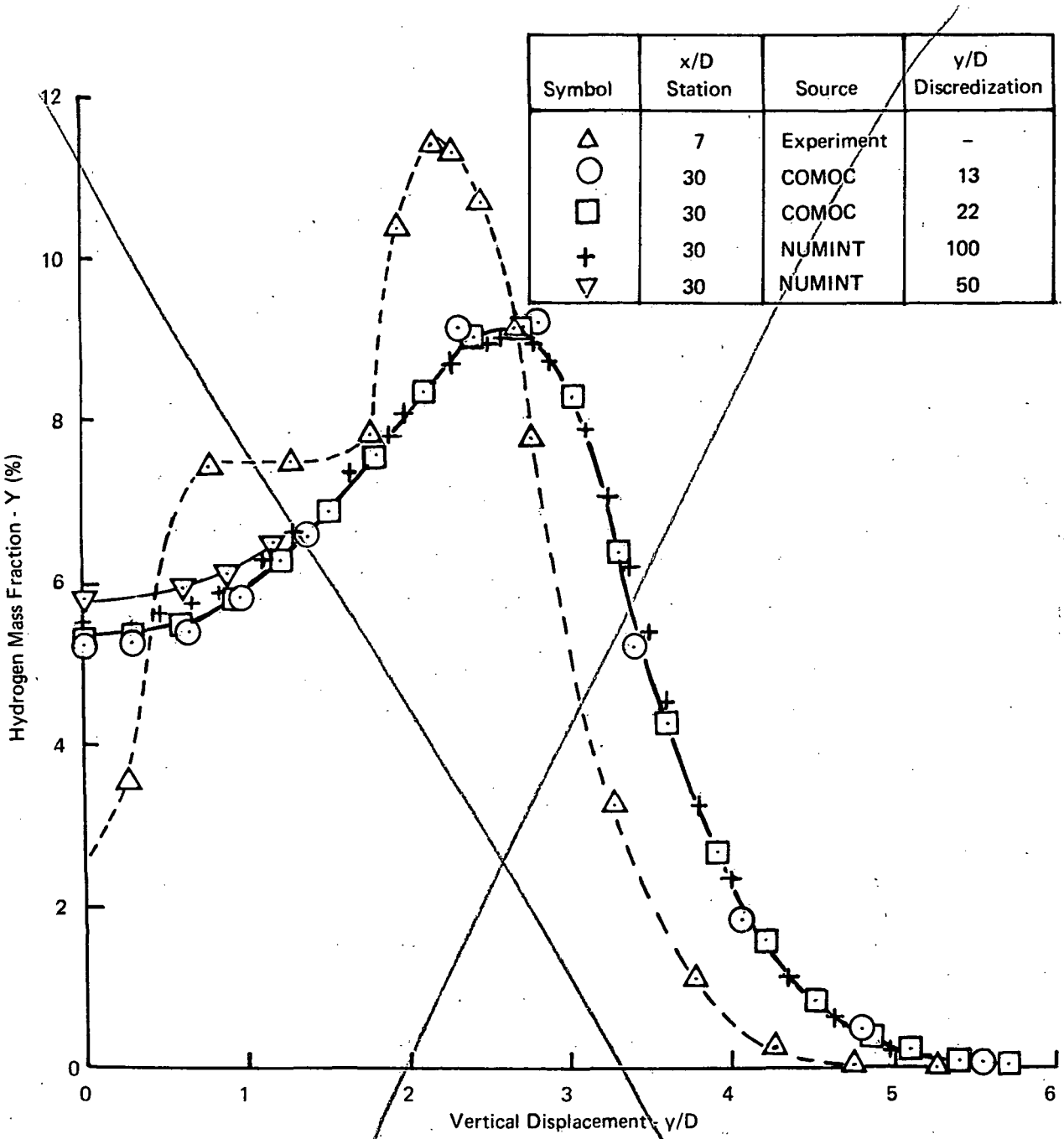

Figure A.1. Comparison Computed Hydrogen Mass Fraction Distributions on Symmetry Centerplane of Mixing Region

Identify a three-dimensional, rectangular parallelepiped control volume, figure A.4, with sides normal to coordinate directions. Employ Gauss' theorem to recast equation (A.1) as a surface integral over this control volume:

$$\oiint [\rho \vec{U} Y - \frac{\mu Le}{Pr} \nabla_2 Y] \cdot \hat{n} d\sigma = 0 \qquad (A.2)$$

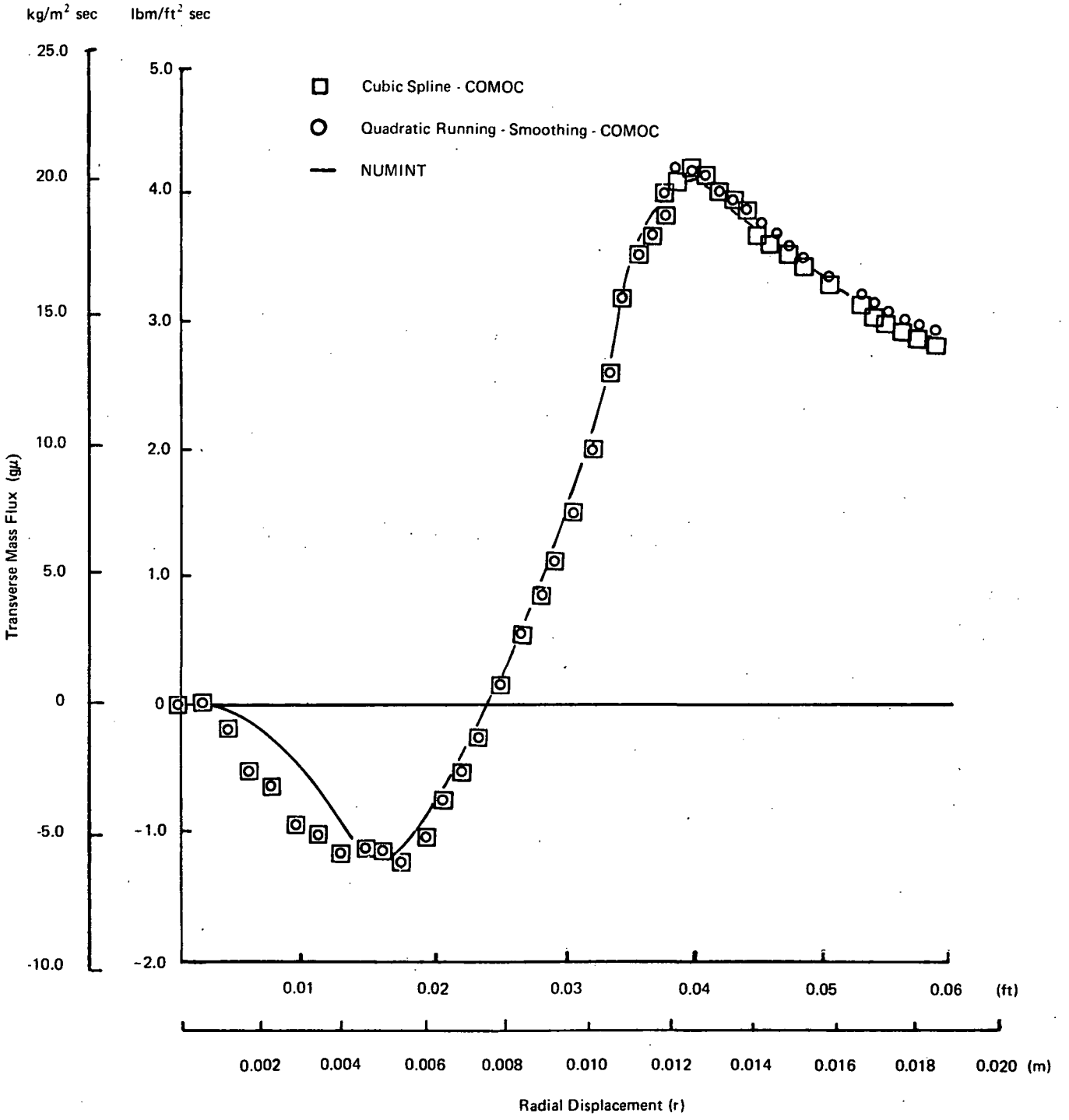

Figure A.3. Computed Transverse Mass Flux Distribution Comparison for COMOC and NUMINT Solutions

For all computations reported herein, the hydrogen mass fraction vanishes on face D. Selective terms may vanish from within the square bracket, equation (A.3), dependent upon applied boundary conditions, e.g., $Y_{,z}$ vanishes on surface C for the multijet, virtual source and centerplane computations, while $Y_{,y}$ essentially vanishes on surface D for all computations, since the solution domain extends well into the freestream.

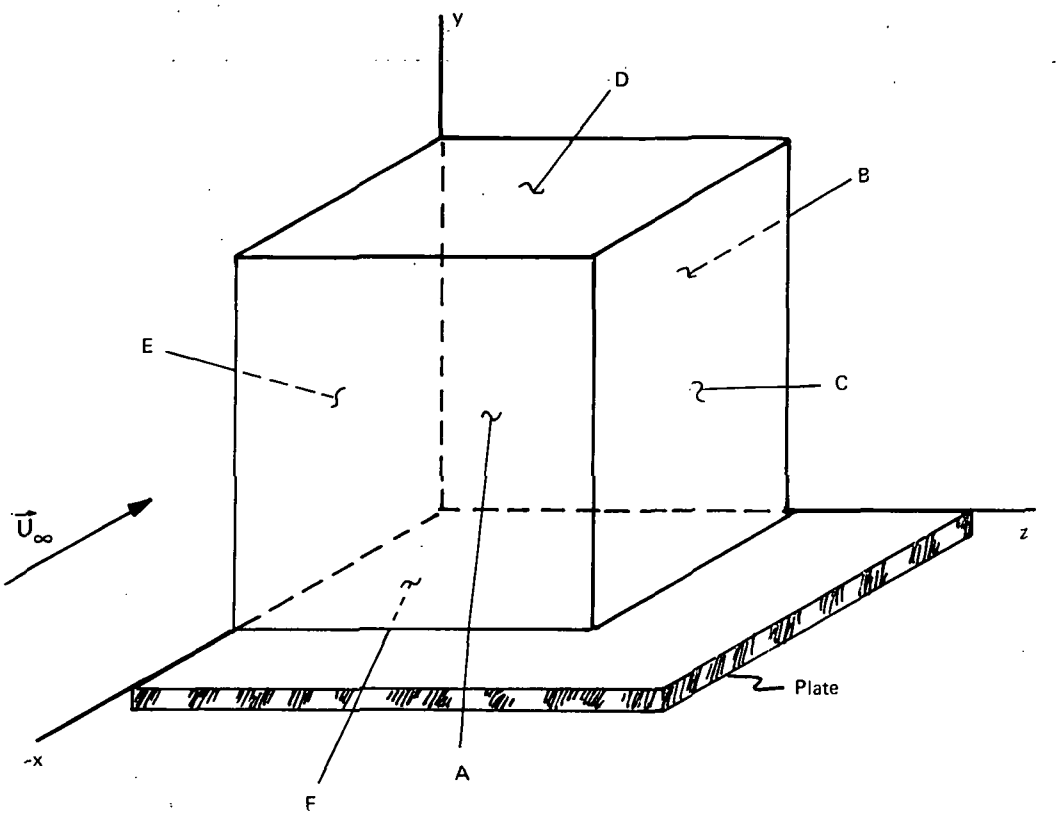

Figure A-4. Control Volume for Numerical Evaluation of Conservation Properties of Three-Dimensional Flow Fields Computations by COMOC.

If vanishing normal gradient boundary conditions are enforced at the plate surface as well, the conservation expression reduces to the familiar form

$$\int_A \rho u Y d\sigma = \text{constant} \tag{A.4}$$

which states that the hydrogen mass fraction flux is analytically constant in every plane with normal parallel to the predominant flow direction. The approximate adherence of computed solutions to equation (A.4) is considered important for verification of the proper operation of a computer program.

The finite element solution algorithm provides a mathematically consistent and readily obtained numerical approximation to equation (A.4). From equation (21), written on both ρu and Y, obtain the following approximation to equation (A.4) within a finite element.

$$FLOW_m = \{RHOU\}_m^T [\Gamma]_m \int_{R_m} \{x\}\{x\}^T d\sigma \, [\Gamma]_m \{Y\}_m \tag{A.5}$$

The integral in equation (A.5) is readily evaluated. A simple DO loop over the finite elements of the discretization sums M terms of this form to yield a numerical approximation to equation (A.4) which contains the details of the computed distribution of both ρu and Y.

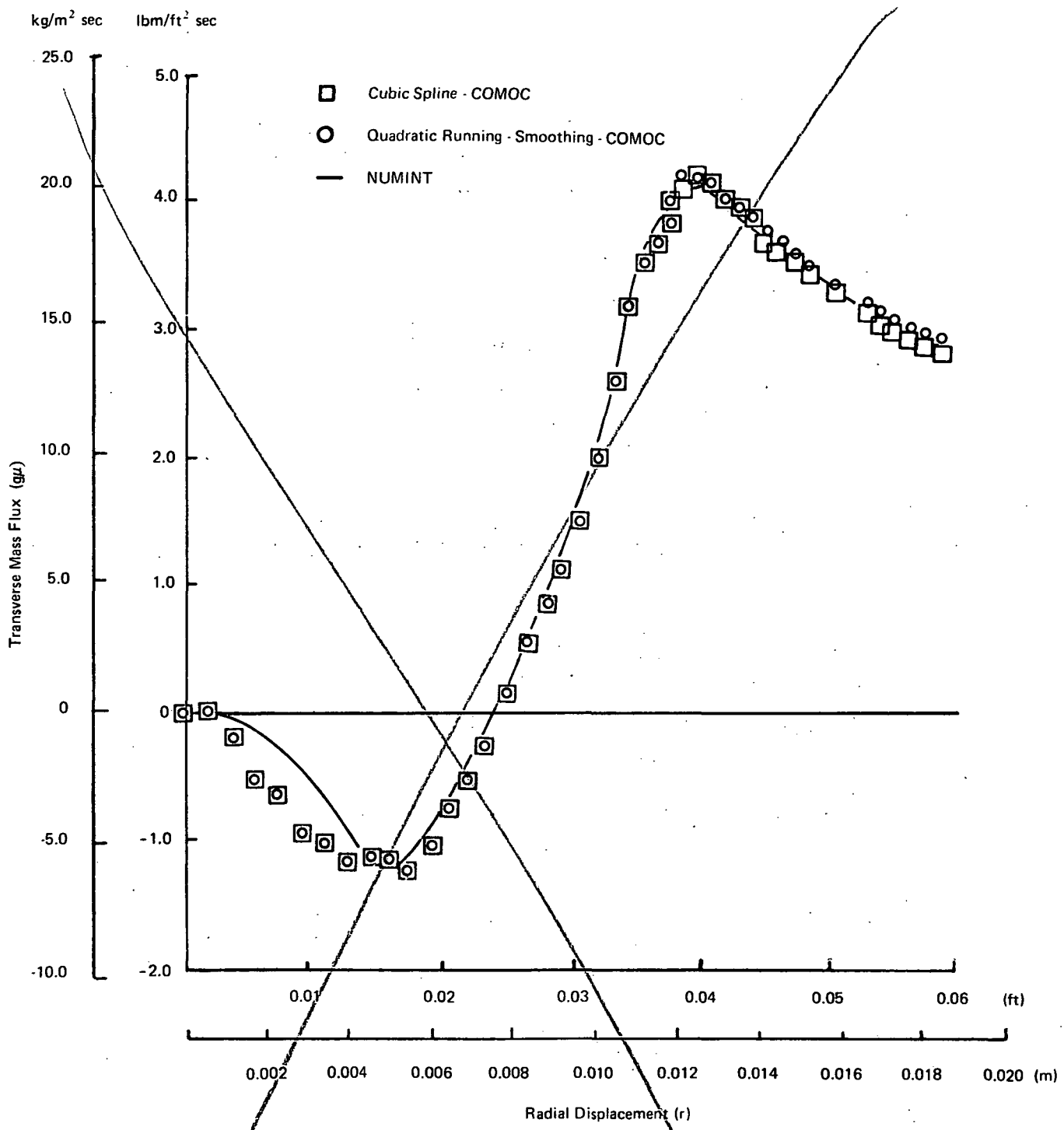

Figure A.3. Computed Transverse Mass Flux Distribution Comparison for COMOC and NUMINT Solutions

For all computations reported herein, the hydrogen mass fraction vanishes on face D. Selective terms may vanish from within the square bracket, equation (A.3), dependent upon applied boundary conditions, e.g., $Y_{,z}$ vanishes on surface C for the multijet, virtual source and centerplane computations, while $Y_{,y}$ essentially vanishes on surface D for all computations, since the solution domain extends well into the freestream.

COMOC computes the sum of equation (A.5) at every output station. Excluding a gross programming error or inconsistent theory, discretization exerts the predominant influence on the sum. In actuality, solution surfaces are complexly curved; equation (A.5) performs a piecewise planar interpolation of the surface, yielding a multi-faceted approximation to the true surface.

The previously discussed centerplane computations employ the correct boundary condition distribution for equation (A.4) to be rigorously valid. Shown in figure A.5 are COMOC-computed deviations from absolute hydrogen flow conservation for the 13- and 22-finite element solutions of the centerplane problem. The comparison data base in both tests was total computed hydrogen flow at Station x/D = 7. The 22-element COMOC solution numerically conserves total hydrogen flow to within ±1.5 percent. There is a computed continual loss of hydrogen mass flow for the 13-element solution, amounting to about 10 percent of the original computed flow at Station x/D = 30. Referring to figure A.1, this computed hydrogen flow loss corresponds to a maximum solution deviation for hydrogen mass fraction of about 3 percent, occurring at the peak of the initial input distribution, to about –4 percent, occurring at the plate surface, and near freestream. Considerable additional experimentation is, of source, required to establish a firm correspondence between computed hydrogen flow conservation and actual solution accuracy. At this juncture, a 10 percent computed loss appears as an acceptable indication of adequate solution accuracy.

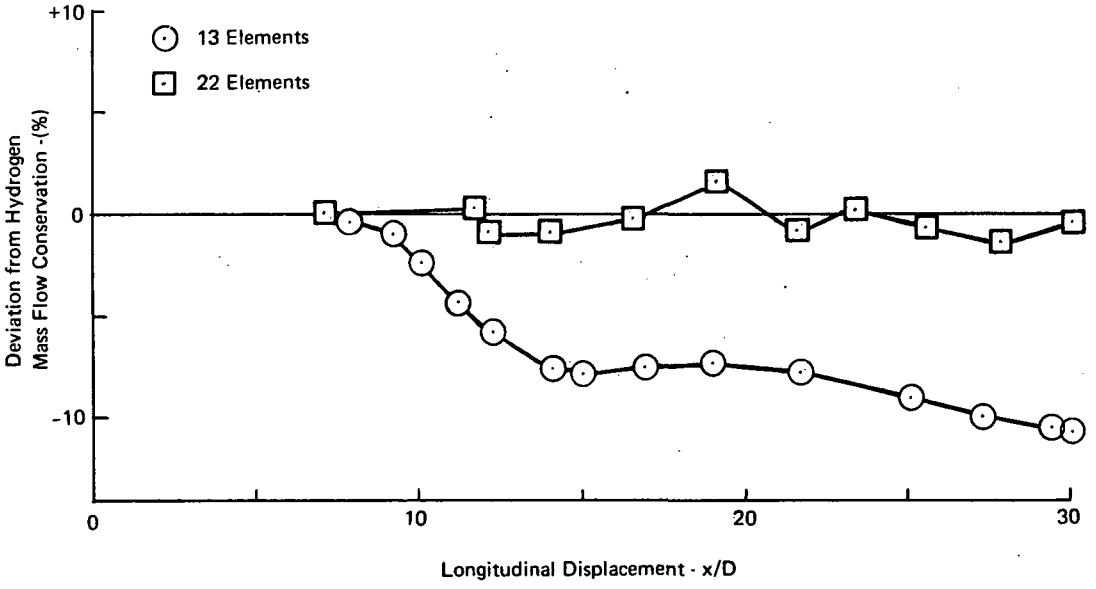

Figure A.5. COMOC Computed Deviations from Hydrogen Flow Conservation for Different Discretizations

The centerplane tests were repeated with hydrogen mass fraction held constant at the initial value at the wall, for $7 \leqslant x/D \leqslant 30$. The maximum computed deviation from hydrogen conservation was +0, –2 percent. Thus, equation (A.4) is probably reasonably accurate for those cases in the present analysis where the diffusion terms (in square brackets), equation (A.3), do not rigorously vanish by gradient boundary condition statements.

APPENDIX B

VIRTUAL SOURCE INITIAL CONDITIONS

The complexity of flow in the near injection region requires that detailed initial data distributions be known to start computations at a downstream station where the elliptic boundary layer approximation is valid. The alternative is establishment of an analytical and/or empirical model of a numerical "virtual source", as discussed. This approach requires establishing simplified initial conditions at a station upstream of the mixing region as a function (only) of undisturbed freestream and injection parameters.

Injection of a jet from an orifice in a plate into a transverse supersonic air stream has been the subject of a number of investigations (ref. 25 through 28). An important correlating parameter is q_r, defined as the ratio of the dynamic pressure in the jet to the corresponding freestream value. Except for the investigations by Rogers (ref. 5 and 6), available experimental data are typically for large values of q_r, whereby the jet has sufficient momentum to penetrate the boundary layer and produce the complicated separation region and bow shock ahead of the jet. In references 5 and 6, q_r ranges between 0.5 and 1.5. The jet lacks the necessary momentum to penetrate the boundary layer. Therefore, mixing occurs within a turbulent boundary layer velocity profile. Consequently, the referenced empirical models are not directly applicable to analysis of the present data, and other means of characterizing the near injection region were investigated.

The proposed barrel shock model of the turning jet is shown in figure B.1. For large values of q_r, a similar configuration with an interaction bow shock has been considered in reference 25. An analysis based on one-dimensional flow was developed for the present case of small q_r to characterize the turning jet. The parameters for the present model are listed in table B.1.

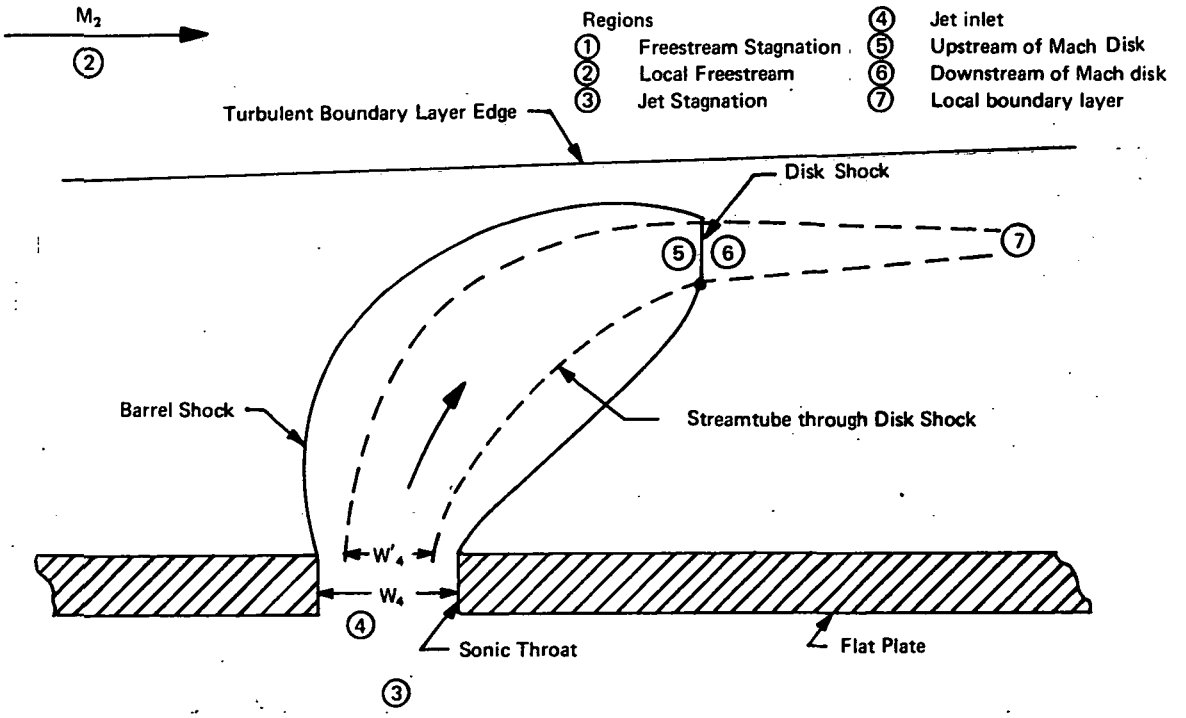

Figure B.1. Transverse Injection into a Turbulent Boundary Layer

TABLE B.1
BARREL SHOCK PARAMETERS

γ	=	specific heat ratio	W_A	=	molecular weight of freestream (air)
M_2	=	local Mach number of region 2	W_H	=	molecular weight of jet (hydrogen)
p_{t1}	=	total pressure in region 1	C_1	=	orifice discharge coefficient
p_{t3}	=	total pressure in region 3	W_4	=	orifice diameter
T_{t1}	=	total temperature in region 1	M_5	=	local Mach number in region 5
T_{t3}	=	total temperature in region 3			

The effective diameter of the stream tube that passes through the Mach disk is described by a discharge coefficient. The isentropic one-dimensional flow relations, and the condition of a sonic jet throat, $M_4 = 1$, are used to determine conditions at stations 3 through 5. The normal shock relations yield the flow quantities in region 6, and the jet is expanded in region 7.

The analysis procedure is an iteration to find the Mach number upstream of the Mach disk, M_5, that allows jet static pressure equilibration with local freestream, i.e., $p_7 = p_2$. From M_5 and the normal shock relations, the velocity immediately downstream of the Mach disk is determined (U_6). Illustrated in figure B.2 is the determination of U_6 for Roger's test conditions of $q_r = 0.5$ and $q_r = 1.0$; assuming $C_1 = 1.0$, i.e., all the injectant passes through the Mach disk. For the virtual source computations discussed, the initial velocity within the hydrogen jet was identified with U_6, as determined by this procedure.

A FORTRAN listing of the barrel shock computer program is included as figure B.3. The required input for a problem is shown in table B.2, and a representative output sample is attached as figure B.4.

TABLE B.2
INPUT SPECIFICATIONS FOR BARREL SHOCK COMPUTER PROGRAM

Card No.	FORTRAN Input Variables*	Format
1	GAMMA, M2, PT1	3F10.5
2	PT3, TT1, TT3	3F10.5
3	WA, WH, C1	3F10.5
4	W4	F10.5
5	XM5	F10.5
6	NCASE	I3

*See Table B.1

APPENDIX B

VIRTUAL SOURCE INITIAL CONDITIONS

The complexity of flow in the near injection region requires that detailed initial data distributions be known to start computations at a downstream station where the elliptic boundary layer approximation is valid. The alternative is establishment of an analytical and/or empirical model of a numerical "virtual source", as discussed. This approach requires establishing simplified initial conditions at a station upstream of the mixing region as a function (only) of undisturbed freestream and injection parameters.

Injection of a jet from an orifice in a plate into a transverse supersonic air stream has been the subject of a number of investigations (ref. 25 through 28). An important correlating parameter is q_r, defined as the ratio of the dynamic pressure in the jet to the corresponding freestream value. Except for the investigations by Rogers (ref. 5 and 6), available experimental data are typically for large values of q_r, whereby the jet has sufficient momentum to penetrate the boundary layer and produce the complicated separation region and bow shock ahead of the jet. In references 5 and 6, q_r ranges between 0.5 and 1.5. The jet lacks the necessary momentum to penetrate the boundary layer. Therefore, mixing occurs within a turbulent boundary layer velocity profile. Consequently, the referenced empirical models are not directly applicable to analysis of the present data, and other means of characterizing the near injection region were investigated.

The proposed barrel shock model of the turning jet is shown in figure B.1. For large values of q_r, a similar configuration with an interaction bow shock has been considered in reference 25. An analysis based on one-dimensional flow was developed for the present case of small q_r to characterize the turning jet. The parameters for the present model are listed in table B.1.

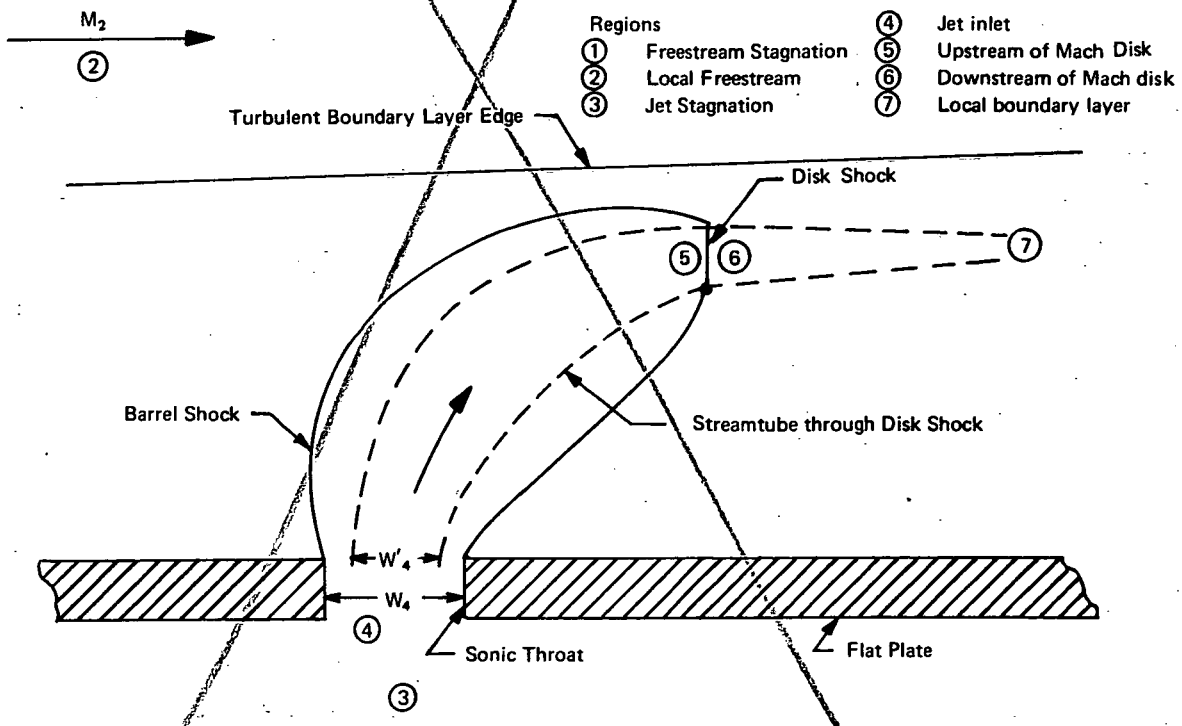

Figure B.1. Transverse Injection into a Turbulent Boundary Layer

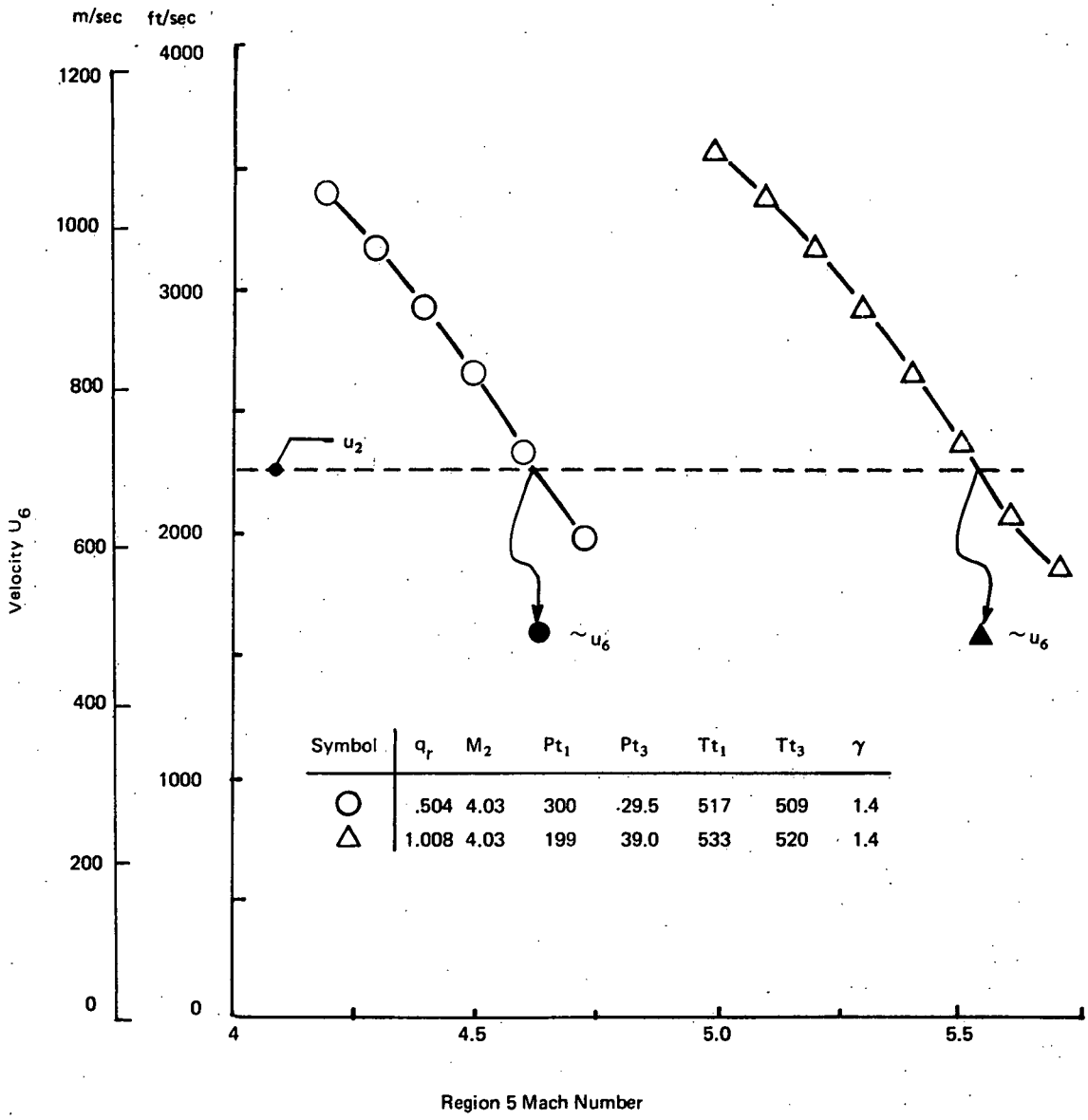

Figure B.2. Determination of Region 5 Mach Number

Figure B.3. Listing of Barrel Shock Computer Program

```
      READ(5,101) G,XM2,PT1,PT3,TT1,TT3,WA,WH,C1,W4
   22 WRITE(6,204)
  204 FORMAT(1H1)
      READ(5,101) XM5
  101 FORMAT(3F10.5)
      READ(5,16) NCASE
   16 FORMAT(I3)
      G1 = G + 1.
      G2 = G - 1.
      G3 = 0.5 * G1
      G4 = 0.5 * G2
      G5 = 2. * G/G1
      XM5S = XM5 * XM5
      EX7 = G3/G2
      EX8 = -EX7
      AS1 = G3 ** EX7
      AS2 = 1. + G4 * XM5S
      AS3 = AS2 ** EX8
      AS4 = AS1 * XM5 * AS3
      S5OS4P = 1./AS4
      XM2S = XM2 * XM2
      RA = 1545./WA
      RH = 1545./WH
      XX = RA * TT1
      DT1 = (144. * PT1)/XX
      DT3 = (144. * PT3)/(RH * TT3)
      Z2 = 1. + G4 * XM2S
      E1 = -1.
      E2 = -G/G2
      E3 = -1./G2
      E4 = -0.5
      XK1 = Z2 **E1
      XK2 = Z2**E2
      XK3 = Z2 ** E3
      XK4 = Z2 ** E4
      TT2 = TT1
      PT2 = PT1
      DT2 = DT1
      AT1S = G * 32.2 * RA * TT1
      AT1 = SQRT(AT1S)
      AT2 = AT1
      AT3S = G * 32.2 * RH * TT3
      AT3 = SQRT(AT3S)
      T2 = TT2 * XK1
      P2 = PT2 * XK2
      D2 = DT2 * XK3
      A2 = AT2 * XK4
      V2 = AT2 * XM2/(SQRT(Z2))
      TT4 = TT3
      PT4 = PT3
      DT4 = DT3
      AT4 = AT3
```

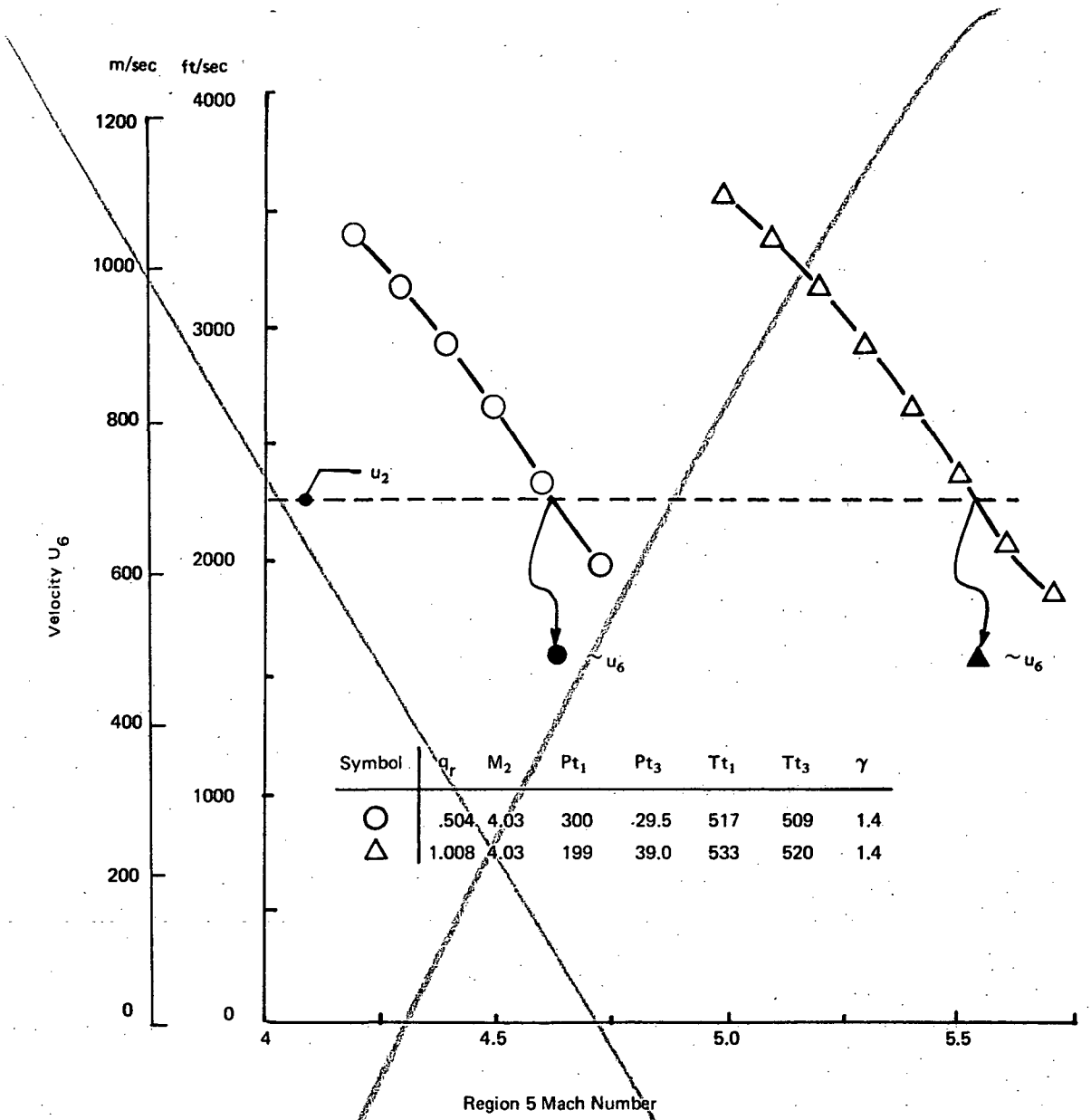

Figure B.2. Determination of Region 5 Mach Number

Figure B.3. –Continued

```
XM4 = 1.
Z4 = 1. + G4 * XM4 * XM4
Q1 = Z4 **E1
Q2 = Z4 ** E2
Q3 = Z4 ** E3
Q4 = Z4 ** E4
T4 = TT4 * Q1
P4 = PT4 * Q2
D4 = DT4 * Q3
A4 = AT4 * Q4
V4 = AT4 * XM4/(SQRT(Z4))
QR = D4 * V4 * V4/(D2 * V2 * V2)
PI = 3.1416
H4 = PI * W4 * W4/(4. * 144.)
F4 = D4 * V4 * H4
F4M = 453.6 * F4
EX1 = G/G2
EX2 = 1./G2
W4P = C1 * W4
CS4 = 4./PI
S4P = W4P * W4P / CS4
S5 = S4P * S5OS4P
W5S = CS4 * S5
W5 = SQRT(W5S)
XM5S = XM5 * XM5
Z5 = 1. + G4 * XM5S
AQ1 = Z5 ** E1
AQ2 = Z5 ** E2
AQ3 = Z5 ** E3
AQ4 = Z5 ** E4
TT5 = TT4
PT5 = PT4
DT5 = DT4
AT5 = AT4
T5 = TT5 * AQ1
P5 = PT5 * AQ2
D5 = DT5 * AQ3
A5 = AT5 * AQ4
V5 = AT5 * XM5/(SQRT(Z5))
P6OP5 = ( 2. * G * XM5S - G2)/G1
D6OD5 = G1 * XM5S/(G2 * XM5S + 2.)
T6OT5 = P6OP5 * (G2 * XM5S + 2.)/(G1 * XM5S)
V6OV5 = 1. - 4. * (XM5S - 1.) * (G * XM5S + 1.)/((G1**XM5S)**2.)
A6OA5 = SQRT(T6OT5)
AS = G3 * XM5S
BS = 1./P6OP5
TT6 = TT5
PT6 = P5 * (AS ** EX1) * (BS ** EX2)
DT6 = PT6 * 144. * WH/(1545. * TT6)
AT6 = AT5
W6 = W5
T6 = T5 * T6OT5
P6 = P5 * P6OP5
D6 = D5 * D6OD5
```

Figure B.3. –Continued

```
      A6 = A5 * A60A5
      DELP = P6 - P2
      IF(DELP.LT.0.0) GO TO 118
      XM6S = (G2 * XM5S + 2.)/(2. * G * XM5S - G2)
      XM6 = SQRT(XM6S)
      Z6 = 1. + G4 * XM6S
      V6 = AT6 * XM6/(SQRT(Z6))
      TT7 = TT6
      PT7 = PT6
      DT7 = DT6
      AT7 = AT6
      P7 = P2
      PF = P7/PT7
      PFG = PF ** (-G2/G)
      XM7S = (PFG - 1.)/G4
      XM7 = SQRT(XM7S)
      XM7S = XM7 * XM7
      Z7 = 1. + G4 * XM7S
      BQ1 = Z7 **E1
      BQ2 = Z7 ** E2
      BQ3 = Z7 ** E3
      BQ4 = Z7 ** E4
      T7 = TT7 * BQ1
      P7C = PT7 * BQ2
      D7 = DT7 * BQ3
      A7 = AT7 * BQ4
      V7 = AT7 * XM7/(SQRT(Z7))
      CJN = 1. + G4 * XM6S
      CJD = 1. + G4 * XM7S
      CJE = CJN/CJD
      CJF =  XM6/XM7
      CJG = -G3/G2
      CJH = CJF * (CJE ** CJG)
      CJI = SQRT(CJH)
      W7 = W6 * CJI
      FCON = PI/576.
      F4 = D4 * V4 * W4 * W4 * FCON
      F4P = D4 * V4 * W4P * W4P * FCON
      F5 = D5 * V5 * W5 * W5 * FCON
      F6 = D6 * V6 * W6 * W6 * FCON
      F7 = D7 * V7 * W7 * W7 * FCON
  118 CONTINUE
      WRITE(6,120) NCASE
  120 FORMAT(T10,'SECONDARY JET',/,T10,'PROGRAMMED BY F.D.HAINS AND R.P
     *.OKULEWICZ',////,T10,'CASE NO. 'I3)
      WRITE(6,121) G,XM2
  121 FORMAT(////,T10,'INPUT',///,T10,'G',T19,'=',E12.4,T42,
     *'SPECIFIC HEAT RATIO',/T10,'XM2',T19,'=',E12.4,T42,
     *'MACH NO. IN REGION 2,FREESTREAM')
      WRITE(6,122) PT1,PT3,TT1
  122 FORMAT(T10,'PT1',T19,'=',E12.4,T42,'TOTAL PRESSURE,REGION 1',
     *T82,'(PSIA)',/,T10,'PT3',T19,'=',E12.4,T42,'TOTAL PRESSURE REGION 3
```

Figure B.3. –Continued

```
XM4 = 1.
Z4 = 1. + G4 * XM4 * XM4
Q1 = Z4 **E1
Q2 = Z4 ** E2
Q3 = Z4 ** E3
Q4 = Z4 ** E4
T4 = TT4 * Q1
P4 = PT4 * Q2
D4 = DT4 * Q3
A4 = AT4 * Q4
V4 = AT4 * XM4/(SQRT(Z4))
QR = D4 * V4 * V4/(D2 * V2 * V2)
PI = 3.1416
H4 = PI * W4 * W4/(4. * 144.)
F4 = D4 * V4 * H4
F4M = 453.6 * F4
EX1 = G/G2
EX2 = 1./G2
W4P = C1 * W4
CS4 = 4./PI
S4P = W4P * W4P / CS4
S5 = S4P * S5OS4P
W5S = CS4 * S5
W5 = SQRT(W5S)
XM5S = XM5 * XM5
Z5 = 1. + G4 * XM5S
AQ1 = Z5 ** E1
AQ2 = Z5 ** E2
AQ3 = Z5 ** E3
AQ4 = Z5 ** E4
TT5 = TT4
PT5 = PT4
DT5 = DT4
AT5 = AT4
T5 = TT5 * AQ1
P5 = PT5 * AQ2
D5 = DT5 * AQ3
A5 = AT5 * AQ4
V5 = AT5 * XM5/(SQRT(Z5))
P6OP5 = ( 2. *G * XM5S - G2)/G1
D6OD5 = G1 * XM5S/(G2 * XM5S + 2.)
T6OT5 = P6OP5 * (G2 * XM5S + 2.)/(G1 * XM5S)
V6OV5 = 1. - 4. * (XM5S - 1.) * (G * XM5S + 1.)/((G1**XM5S)**2.)
A6OA5 = SQRT(T6OT5)
AS = G3 * XM5S
BS = 1./P6OP5
TT6 = TT5
PT6 = P5 * (AS ** EX1) * (BS ** EX2)
DT6 = PT6 * 144. * WH/(1545. * TT6)
AT6 = AT5
W6 = W5
T6 = T5 * T6OT5
P6 = P5 * P6OP5
D6 = D5 * D6OD5
```

Figure B.3. – Continued

```
     *',T82,'(PSIA)',/,T10,'TT1',T19,'=',E12.4,T42,'TOTAL TEMPERATURE,RE
     *GION 1',T82,'(DEG.RANKINE)')
      WRITE(6,123) TT3,WA,WH
  123 FORMAT(T10,'TT3',T19,'=',E12.4,T42,'TOTAL TEMPERATURE REGION 3',
     *T82,'(DEG. RANKINE)',/,T10,'WA',T19,'=',E12.4,T42,'MOLECULAR WEIGH
     *T,AIR',T82,'(1/MOLE)',/,T10,'WH',T19,'=',E12.4,T42,'MOLECULAR WEIG
     *HT,HYDROGEN',T82,'(1/MOLE)')
      WRITE(6,124) C1,W4,XM5
  124 FORMAT(T10,'C1',T19,'=',E12.4,T42,'ORIFICE DISCHARGE COEFFICIENT'
     *,/
     *,T10,'W4',T19,'=',E12.4,T42,'DIAMETER OF ORIFICE',T82,'(INCHES)',
     */,T10,'XM5',T19,'=',E12.4,T42,'MACH NO. IN REGION 5')
      IF(DELP.LT.0.0) GO TO 202
      WRITE(6,125)PT1,DT1,TT1
  125 FORMAT(//,T10,'OUTPUT',//,T10,'PT1',T19,'=',E12.4,T42,
     *                                                'TOTAL PRESS
     *URE,REGION 1',T82,'(PSIA)',/,T10,'DT1',T19,'=',E12.4,T42,'TOTAL DE
     *NSITY,REGION 1',T82,'(LBM/CU.FT.)',/,T10,'TT1',T19,'=',E12.4,T42,
     *'TOTAL TEMPERATURE,REGION 1',T82,'(DEG.RANKINE)')
      WRITE(6,126) AT1,PT2,DT2
  126 FORMAT(T10,'AT1',T19,'=',E12.4,T42,'TOTAL SPEED OF SOUND,REGION 1'
     *,T82,'(FT./SEC.)',/,T10,'PT2',T19,'=',E12.4,T42,'TOTAL PRESSURE,RE
     *GION 2',T82,'(PSIA)',/,T10,'DT2',T19,'=',E12.4,T42,'TOTAL DENSITY,
     *REGION 2',T82,' (LBM/CU.FT.)')
      WRITE(6,127) TT2,AT2,P2
  127 FORMAT(T10,'TT2',T19,'=',E12.4,T42,'TOTAL TEMPERATURE REGION 2',
     *T82,'(DEG. RANKINE)',/,T10,'AT2',T19,'=',E12.4,T42,'TOTAL SPEED OF
     * SOUND,REGION 2',T82,' (FT./SEC.)',/,T10,'P2',T19,'=',E12.4,T42,
     * 'PRESSURE REGION 2',T82,'(PSIA)')
      WRITE(6,128) D2,T2,A2
  128 FORMAT(T10,'D2',T19,'=',E12.4,T42,'DENSITY,REGION 2',T82,'(LBM/CU.
     *FT.)',/,T10,'T2',T19,'=',E12.4,T42,'TEMPERATURE,REGION 2',T82,
     *'(DEG. RANKINE)',/,T10,'A2',T19,'=',E12.4,T42,'SPEED OF SOUND,REGI
     *ON 2',T82,'(FT./SEC.)')
      WRITE(6,129) V2,PT3,DT3
  129 FORMAT(T10,'V2',T19,'=',E12.4,T42,'VELOCITY, REGION 2',T82,'(FT./S
     *EC.)',/,T10,'PT3',T19,'=',E12.4,T42,'TOTAL PRESSURE REGION 3',T82,
     * '(PSIA)',/,T10,'DT3',T19,'=',E12.4,T42,'TOTAL DENSITY,REGION 3',
     * T82,'(LBM/CU.FT.)')
      WRITE(6,130)TT3,AT3,PT4
  130 FORMAT(T10,'TT3',T19,'=',E12.4,T42,'TOTAL TEMPERATURE,REGION 3',
     *T82 '(DEG. RANKINE)',/,T10,'AT3',T19,'=',E12.4,T42,'TOTAL SPEED OF
     * SOUND,REGION 3',T82,'(FT./SEC.)',/,T10,'PT4',T19,'=',E12.4,T42,
     *'TOTAL PRESSURE,REGION 4',T82,'(PSIA)')
      WRITE(6,131) DT4,TT4,AT4
  131 FORMAT (T10,'DT4',T19,'=',E12.4,T42,'TOTAL DENSITY,REGION 4',T82,
     * '(LBM/CU.FT.)',/,T10,'TT4',T19,'=',E12.4,T42,'TOTAL TEMPERATURE,R
     *EGION 4',T82,'(DEG. RANKINE)',/,T10,'AT4',T19,'=',E12.4,T42,'TOTAL
     * SPEED OF SOUND,REGION 4',T82,'(FT./SEC.)')
      WRITE(6,132) P4,D4,T4
```

Figure B.3. – Continued

```
132 FORMAT(T10,'P4',T19,'=',E12.4,T42,'PRESSURE,REGION 4',T82,'(PSIA)'
    *,/,T10,'D4',T19,'=',E12.4,T42,'DENSITY,REGION 4',T82,'(LBM./CU.FT.
    *)',T10,'T4',T19,'=',E12.4,T42,'TEMPERATURE,REGION 4',
    *T82,'(DEG. RANKINE)')
     WRITE(6,133) A4,V4,W4,W4P
133 FORMAT(T10,'A4',T19,'=',E12.4,T42,'SPEED OF SOUND,REGION 4',T82,
    * '(FT./SEC.)',/,T10,'V4',T19,'=',E12.4,T42,'VELOCITY,REGION 4',T82
    *,'(FT./SEC.)',/,T10,'W4',T19,'=',E12.4,T42,'JET WIDTH,REGION 4',
    * T82,'(INCHES)',/,T10,'W4P',T19,'=',E12.4,T42,'EFFECTIVE JET WIDTH
    *,REGION 4',T82,'(INCHES)')
     WRITE(6,134) PT5,DT5,TT5
134 FORMAT(T10,'PT5',T19,'=',E12.4,T42,'TOTAL PRESSURE,REGION 5',T82,
    * '(PSIA)',/,T10,'DT5',T19,'=',E12.4,T42,'TOTAL DENSITY,REGION 5',
    * T82,'(LBM./CU.FT.)',/,T10,'TT5',T19,'=',E12.4,T42,'TOTAL TEMPERAT
    *URE,REGION 5',T82,'(DEG. RANKINE)')
     WRITE(6,135) AT5,P5,D5
135 FORMAT(T10,'AT5',T19,'=',E12.4,T42,'TOTAL SPEED OF SOUND,REGION 5'
    *,T82,'(FT./SEC.)',/T10,'P5',T19,'=',E12.4,T42,'PRESSURE,REGION 5',
    * T82,'(PSIA)',/T10,'D5',T19,'=',E12.4,T42,'DENSITY,REGION 5',
    * T82,'(LBM./CU.FT.)')
     WRITE(6,136) T5,A5,V5
136 FORMAT(T10,'T5',T19,'=',E12.4,T42,'TEMPERATURE,REGION 5',T82,
    *'(DEG. RANKINE)',/,T10,'A5',T19,'=',E12.4,T42,'SPEED OF SOUND,REGI
    *ON 5',T82,'(FT./SEC.)',/,T10,'V5',T19,'=',E12.4,T42,'VELOCITY,REGI
    *ON 5',T82,'(FT./SEC.)')
     WRITE(6,137) XM5,W5
137 FORMAT(T10,'XM5',T19,'=',E12.4,T42,'MACH NUMBER,REGION 5',/,T10,
    *'W5',T19,'=',E12.4,T42,'JET WIDTH,REGION 5',T82,'(INCHES)')
     WRITE(6,138) PT6,DT6,TT6
138 FORMAT(T10,'PT6',T19,'=',E12.4,T42,'TOTAL PRESSURE,REGION 6',T82,
    * '(PSIA)',/,T10,'DT6',T19,'=',E12.4,T42,'TOTAL DENSITY,REGION 6',
    * T82,'(LBM./CU.FT.)',/,T10,'TT6',T19,'=',E12.4,T42,'TOTAL TEMPERAT
    *URE,REGION 6',T82,'(DEG. RANKINE)')
     WRITE(6,139) AT6,P6,D6
139 FORMAT(T10,'AT6',T19,'=',E12.4,T42,'TOTAL SPEED OF SOUND,REGION 6'
    *,T82,'(FT./SEC.)',/T10,'P6',T19,'=',E12.4,T42,'PRESSURE,REGION 6',
    * T82,'(PSIA)',/T10,'D6',T19,'=',E12.4,T42,'DENSITY,REGION 6',
    * T82,'(LBM./CU.FT.)')
     WRITE(6,140) T6,A6,V6
140 FORMAT(T10,'T6',T19,'=',E12.4,T42,'TEMPERATURE,REGION 6',T82,
    *'(DEG. RANKINE)',/,T10,'A6',T19,'=',E12.4,T42,'SPEED OF SOUND,REGI
    *ON 6',T82,'(FT./SEC.)',/,T10,'V6',T19,'=',E12.4,T42,'VELOCITY,REGI
    *ON 6',T82,'(FT./SEC.)')
     WRITE(6,141) XM6,W6
141 FORMAT(T10,'XM6',T19,'=',E12.4,T42,'MACH NUMBER,REGION 6',/,T10,
    *'W6',T19,'=',E12.4,T42,'JET WIDTH,REGION 6',T82,'(INCHES)')
     WRITE(6,142) PT7,DT7,TT7
142 FORMAT(T10,'PT7',T19,'=',E12.4,T42,'TOTAL PRESSURE,REGION 7',T82,
```

Figure B.3. – Continued

```
     *',T82,'(PSIA)',/,T10,'TT1',T19,'=',E12.4,T42,'TOTAL TEMPERATURE,RE
     *GION 1',T82,'(DEG.RANKINE)')
      WRITE(6,123) TT3,WA,WH
  123 FORMAT(T10,'TT3',T19,'=',E12.4,T42,'TOTAL TEMPERATURE REGION 3',
     *T82,'(DEG. RANKINE)',/,T10,'WA',T19,'=',E12.4,T42,'MOLECULAR WEIGH
     *T,AIR',T82,'(1/MOLE)',/,T10,'WH',T19,'=',E12.4,T42,'MOLECULAR WEIG
     *HT,HYDROGEN',T82,'(1/MOLE)')
      WRITE(6,124) C1,W4,XM5
  124 FORMAT(T10,'C1',T19,'=',E12.4,T42,'ORIFICE DISCHARGE COEFFICIENT'
     *,/
     *,T10,'W4',T19,'=',E12.4,T42,'DIAMETER OF ORIFICE',T82,'(INCHES)',
     */,T10,'XM5',T19,'=',E12.4,T42,'MACH NO. IN REGION 5')
      IF(DELP.LT.0.0) GO TO 202
      WRITE(6,125)PT1,DT1,TT1
  125 FORMAT(//,T10,'OUTPUT',//,T10,'PT1',T19,'=',E12.4,T42,
     *                                                 'TOTAL PRESS
     *URE,REGION 1',T82,'(PSIA)',/,T10,'DT1',T19,'=',E12.4,T42,'TOTAL DE
     *NSITY,REGION 1',T82,'(LBM/CU.FT.)',/,T10,'TT1',T19,'=',E12.4,T42,
     *'TOTAL TEMPERATURE,REGION 1',T82,'(DEG.RANKINE)')
      WRITE(6,126) AT1,PT2,DT2
  126 FORMAT(T10,'AT1',T19,'=',E12.4,T42,'TOTAL SPEED OF SOUND,REGION 1'
     *,T82,'(FT./SEC.)',/,T10,'PT2',T19,'=',E12.4,T42,'TOTAL PRESSURE,RE
     *GION 2',T82,'(PSIA)',/,T10,'DT2',T19,'=',E12.4,T42,'TOTAL DENSITY,
     *REGION 2',T82,' (LBM/CU.FT.)')
      WRITE(6,127) TT2,AT2,P2
  127 FORMAT(T10,'TT2',T19,'=',E12.4,T42,'TOTAL TEMPERATURE REGION 2',
     *T82,'(DEG. RANKINE)',/,T10,'AT2',T19,'=',E12.4,T42,'TOTAL SPEED OF
     * SOUND,REGION 2',T82,' (FT./SEC.)',/,T10,'P2',T19,'=',E12.4,T42,
     * 'PRESSURE REGION 2',T82,'(PSIA)')
      WRITE(6,128) D2,T2,A2
  128 FORMAT(T10,'D2',T19,'=',E12.4,T42,'DENSITY,REGION 2',T82,'(LBM/CU.
     *FT.)',/,T10,'T2',T19,'=',E12.4,T42,'TEMPERATURE,REGION 2',T82,
     *'(DEG. RANKINE)',/,T10,'A2',T19,'=',E12.4,T42,'SPEED OF SOUND,REGI
     *ON 2',T82,'(FT./SEC.)')
      WRITE(6,129) V2,PT3,DT3
  129 FORMAT(T10,'V2',T19,'=',E12.4,T42,'VELOCITY, REGION 2',T82,'(FT./S
     *EC.)',/,T10,'PT3',T19,'=',E12.4,T42,'TOTAL PRESSURE REGION 3',T82,
     * '(PSIA)',/,T10,'DT3',T19,'=',E12.4,T42,'TOTAL DENSITY,REGION 3',
     * T82,'(LBM/CU.FT.)')
      WRITE(6,130)TT3,AT3,PT4
  130 FORMAT(T10,'TT3',T19,'=',E12.4,T42,'TOTAL TEMPERATURE,REGION 3',
     *T82 '(DEG. RANKINE)',/,T10,'AT3',T19,'=',E12.4,T42,'TOTAL SPEED OF
     * SOUND,REGION 3',T82,'(FT./SEC.)',/,T10,'PT4',T19,'=',E12.4,T42,
     *'TOTAL PRESSURE,REGION 4',T82,'(PSIA)')
      WRITE(6,131) DT4,TT4,AT4
  131 FORMAT (T10,'DT4',T19,'=',E12.4,T42,'TOTAL DENSITY,REGION 4',T82,
     * '(LBM/CU.FT.)',/,T10,'TT4',T19,'=',E12.4,T42,'TOTAL TEMPERATURE,R
     *EGION 4',T82,'(DEG. RANKINE)',/,T10,'AT4',T19,'=',E12.4,T42,'TOTAL
     * SPEED OF SOUND,REGION 4',T82,'(FT./SEC.)')
      WRITE(6,132) P4,D4,T4
```

Figure B.3. – Concluded

```
     * '(PSIA)',/,T10,'DT7',T19,'=',E12.4,T42,'TOTAL DENSITY,REGION 7',
     * T82,'(LBM./CU.FT.)',/,T10,'TT7',T19,'=',E12.4,T42,'TOTAL TEMPERAT
     *URE,REGION 7',T82,'(DEG. RANKINE)')
      WRITE(6,143) AT7,P7,D7
  143 FORMAT(T10,'AT7',T19,'=',E12.4,T42,'TOTAL SPEED OF SOUND,REGION 7'
     *,T82,'(FT./SEC.)',/T10,'P7',T19,'=',E12.4,T42,'PRESSURE,REGION 7',
     * T82,'(PSIA)',/T10,'D7',T19,'=',E12.4,T42,'DENSITY,REGION 7',
     * T82,'(LBM./CU.FT.)')
      WRITE(6,144) T7,A7,V7
  144 FORMAT(T10,'T7',T19,'=',E12.4,T42,'TEMPERATURE,REGION 7',T82,
     *'(DEG. RANKINE)',/,T10,'A7',T19,'=',E12.4,T42,'SPEED OF SOUND,REGI
     *ON 7',T82,'(FT./SEC.)',/,T10,'V7',T19,'=',E12.4,T42,'VELOCITY,REGI
     *ON 7',T82,'(FT./SEC.)')
      WRITE(6,145) XM7,W7
  145 FORMAT(T10,'XM7',T19,'=',E12.4,T42,'MACH NUMBER,REGION 7',/,T10,
     *'W7',T19,'=',E12.4,T42,'JET WIDTH,REGION 7',T82,'(INCHES)')
      WRITE(6,146) F4,F4P,F5
  146 FORMAT(T10,'F4',T19,'=',E12.4,T42,'MASS FLOW,REGION 4',T82,'(LBM./
     *SEC.)',/,T10,'F4P',T19,'=',E12.4,T42,'EFFECTIVE MASS FLOW REGION 4
     *',T82,'LBM./SEC.)',/,T10,'F5',T19,'=',E12.4,T42,'MASS FLOW,REGION
     *5',T82,'(LBM./SEC.)')
      WRITE(6,147)F6,F7,QR
  147 FORMAT(T10,'F6',T19,'=',E12.4,T42,'MASS FLOW,REGION 6',T82,'(LBM./
     *SEC.)',/,T10,'F7',T19,'=',E12.4,T42,'MASS FLOW,REGION 7',T82,'(LBM
     *./SEC.)',/,T10,'QR',T19,'=',E12.4,T42,'DYNAMIC PRESSURE RATIO')
      WRITE(6,119) S5OS4P
  119 FORMAT(T10,'S5OS4P',T19,'=',E12.4,T42,'AREA RATIO REGION 5 TO REGI
     *ON 4P')
      GO TO 22
  202 WRITE(6,203)
  203 FORMAT(10X,'DELP LESS THAN 0.0')
    1 STOP
      END
/DATA
1.4         4.03        300.3
294.6       517.        509.
29.0        2.016       0.5
.040
4.6
999
END
```

Figure B.4. Sample Output from Barrel Shock Computer Program

```
INPUT

G        =   0.1400E 01 SPECIFIC HEAT RATIO
XM2      =   0.4030E 01 MACH NO. IN REGION 2,FREESTREAM
PT1      =   0.3003E 03 TOTAL PRESSURE,REGION 1              (PSIA)
PT3      =   0.2946E 03 TOTAL PRESSURE REGION3               (PSIA)
TT1      =   0.5170E 03 TOTAL TEMPERATURE,REGION 1           (DEG.RANKINE)
TT3      =   0.5090E 03 TOTAL TEMPERATURE REGION 3           (DEG. RANKINE)
WA       =   0.2900E 02 MOLECULAR WEIGHT,AIR                 (1/MOLE)
WH       =   0.2016E 01 MOLECULAR WEIGHT,HYDROGEN            (1/MOLE)
C1       =   0.5000E 00 ORIFICE DISCHARGE COEFFICIENT
W4       =   0.4000E-01 DIAMETER OF ORIFICE                  (INCHES)
XM5      =   0.4600E 01 MACH NO. IN REGION 5

OUTPUT

PT1      =   0.3003E 03 TOTAL PRESSURE,REGION 1              (PSIA)
DT1      =   0.1570E 01 TOTAL DENSITY,REGION 1               (LBM/CU.FT.)
TT1      =   0.5170E 03 TOTAL TEMPERATURE,REGION 1           (DEG.RANKINE)
AT1      =   0.1114E 04 TOTAL SPEED OF SOUND,REGION 1        (FT./SEC.)
PT2      =   0.3003E 03 TOTAL PRESSURE,REGION 2              (PSIA)
DT2      =   0.1570E 01 TOTAL DENSITY,REGION 2               (LBM/CU.FT.)
TT2      =   0.5170E 03 TOTAL TEMPERATURE REGION 2           (DEG. RANKINE)
AT2      =   0.1114E 04 TOTAL SPEED OF SOUND,REGION 2        (FT./SEC.)
P2       =   0.1900E 01 PRESSURE REGION 2                    (PSIA)
D2       =   0.4221E-01 DENSITY,REGION 2                     (LBM/CU.FT.)
T2       =   0.1217E 03 TEMPERATURE,REGION 2                 (DEG. RANKINE)
A2       =   0.5406E 03 SPEED OF SOUND,REGION 2              (FT./SEC.)
V2       =   0.2179E 04 VELOCITY, REGION 2                   (FT./SEC.)
PT3      =   0.2946E 03 TOTAL PRESSURE REGION 3              (PSIA)
DT3      =   0.1088E 00 TOTAL DENSITY,REGION 3               (LBM/CU.FT.)
TT3      =   0.5090E 03 TOTAL TEMPERATURE,REGION 3           (DEG. RANKINE)
AT3      =   0.4193E 04 TOTAL SPEED OF SOUND,REGION 3        (FT./SEC.)
PT4      =   0.2946E 03 TOTAL PRESSURE,REGION 4              (PSIA)
DT4      =   0.1088E 00 TOTAL DENSITY,REGION 4               (LBM/CU.FT.)
TT4      =   0.5090E 03 TOTAL TEMPERATURE,REGION 4           (DEG. RANKINE)
AT4      =   0.4193E 04 TOTAL SPEED OF SOUND,REGION 4        (FT./SEC.)
P4       =   0.1556E 03 PRESSURE,REGION 4                    (PSIA)
T4       =   0.4242E 03 TEMPERATURE,REGION 4                 (DEG. RANKINE)
A4       =   0.3828E 04 SPEED OF SOUND,REGION 4              (FT./SEC.)
V4       =   0.3828E 04 VELOCITY,REGION 4                    (FT./SEC.)
W4       =   0.4000E-01 JET WIDTH,REGION 4                   (INCHES)
W4P      =   0.2000E-01 EFFECTIVE JET WIDTH,REGION 4         (INCHES)
PT5      =   0.2946E 03 TOTAL PRESSURE,REGION 5              (PSIA)
DT5      =   0.1088E 00 TOTAL DENSITY,REGION 5               (LBM./CU.FT.)
```

Figure B.3. – Concluded

```
     * '(PSIA)',/,T10,'DT7',T19,'=',E12.4,T42,'TOTAL DENSITY,REGION 7',
     * T82,'(LBM./CU.FT.)',/,T10,'TT7',T19,'=',E12.4,T42,'TOTAL TEMPERAT
     *URE,REGION 7',T82,'(DEG. RANKINE)')
      WRITE(6,143) AT7,P7,D7
  143 FORMAT(T10,'AT7',T19,'=',E12.4,T42,'TOTAL SPEED OF SOUND,REGION 7'
     *,T82,'(FT./SEC.)',/T10,'P7',T19,'=',E12.4,T42,'PRESSURE,REGION 7',
     * T82,'(PSIA)',/T10,'D7',T19,'=',E12.4,T42,'DENSITY,REGION 7',
     * T82,'(LBM./CU.FT.)')
      WRITE(6,144) T7,A7,V7
  144 FORMAT(T10,'T7',T19,'=',E12.4,T42,'TEMPERATURE,REGION 7',T82,
     *'(DEG. RANKINE)',/,T10,'A7',T19,'=',E12.4,T42,'SPEED OF SOUND,REGI
     *ON 7',T82,'(FT./SEC.)',/,T10,'V7',T19,'=',E12.4,T42,'VELOCITY,REGI
     *ON 7',T82,'(FT./SEC.)')
      WRITE(6,145) XM7,W7
  145 FORMAT(T10,'XM7',T19,'=',E12.4,T42,'MACH NUMBER,REGION 7',/,T10,
     *'W7',T19,'=',E12.4,T42,'JET WIDTH,REGION 7',T82,'(INCHES)')
      WRITE(6,146) F4,F4P,F5
  146 FORMAT(T10,'F4',T19,'=',E12.4,T42,'MASS FLOW,REGION 4',T82,'(LBM./
     *SEC.)',/,T10,'F4P',T19,'=',E12.4,T42,'EFFECTIVE MASS FLOW REGION 4
     *',T82,'LBM./SEC.)',/,T10,'F5',T19,'=',E12.4,T42,'MASS FLOW,REGION
     *5',T82,'(LBM./SEC.)')
      WRITE(6,147)F6,F7,QR
  147 FORMAT(T10,'F6',T19,'=',E12.4,T42,'MASS FLOW,REGION 6',T82,'(LBM./
     *SEC.)',/,T10,'F7',T19,'=',E12.4,T42,'MASS FLOW,REGION 7',T82,'(LBM
     *./SEC.)',/,T10,'QR',T19,'=',E12.4,T42,'DYNAMIC PRESSURE RATIO')
      WRITE(6,119) S5OS4P
  119 FORMAT(T10,'S5OS4P',T19,'=',E12.4,T42,'AREA RATIO REGION 5 TO REGI
     *ON 4P')
      GO TO 22
  202 WRITE(6,203)
  203 FORMAT(10X,'DELP LESS THAN 0.0')
    1 STOP
      END
/DATA
1.4         4.03        300.3
294.6       517.        509.
29.0        2.016       0.5
.040
4.6
999
END
```

Figure B.4. – Concluded

TT5	=	0.5090E 03	TOTAL TEMPERATURE,REGION 5	(DEG. RANKINE)
AT5	=	0.4193E 04	TOTAL SPEED OF SOUND,REGION 5	(FT./SEC.)
P5	=	0.8993E 00	PRESSURE,REGION 5	(PSIA)
D5	=	0.1737E-02	DENSITY,REGION 5	(LBM./CU.FT.)
T5	=	0.9729E 02	TEMPERATURE,REGION 5	(DEG. RANKINE)
A5	=	0.1833E 04	SPEED OF SOUND,REGION 5	(FT./SEC.)
V5	=	0.8433E 04	VELOCITY,REGION 5	(FT./SEC.)
XM5	=	0.4600E 01	MACH NUMBER,REGION 5	
W5	=	0.8489E-01	JET WIDTH,REGION 5	(INCHES)
PT6	=	0.2492E 02	TOTAL PRESSURE,REGION 6	(PSIA)
DT6	=	0.9199E-02	TOTAL DENSITY,REGION 6	(LBM./CU.FT.)
TT6	=	0.5090E 03	TOTAL TEMPERATURE,REGION 6	(DEG. RANKINE)
AT6	=	0.4193E 04	TOTAL SPEED OF SOUND,REGION 6	(FT./SEC.)
P6	=	0.2205E 02	PRESSURE,REGION 6	(PSIA)
D6	=	0.8429E-02	DENSITY,REGION 6	(LBM./CU.FT.)
T6	=	0.4915E 03	TEMPERATURE,REGION 6	(DEG. RANKINE)
A6	=	0.4121E 04	SPEED OF SOUND,REGION 6	(FT./SEC.)
V6	=	0.1738E 04	VELOCITY,REGION 6	(FT./SEC.)
XM6	=	0.4217E 00	MACH NUMBER,REGION 6	
W6	=	0.8489E-01	JET WIDTH,REGION 6	(INCHES)
PT7	=	0.2492E 02	TOTAL PRESSURE,REGION 7	(PSIA)
DT7	=	0.9199E-02	TOTAL DENSITY,REGION 7	(LBM./CU.FT.)
TT7	=	0.5090E 03	TOTAL TEMPERATURE,REGION 7	(DEG. RANKINE)
AT7	=	0.4193E 04	TOTAL SPEED OF SOUND,REGION 7	(FT./SEC.)
P7	=	0.1900E 01	PRESSURE,REGION 7	(PSIA)
D7	=	0.1463E-02	DENSITY,REGION 7	(LBM./CU.FT.)
T7	=	0.2440E 03	TEMPERATURE,REGION 7	(DEG. RANKINE)
A7	=	0.2903E 04	SPEED OF SOUND,REGION 7	(FT./SEC.)
V7	=	0.6766E 04	VELOCITY,REGION 7	(FT./SEC.)
XM7	=	0.2330E 01	MACH NUMBER,REGION 7	
W7	=	0.1033E 00	JET WIDTH,REGION 7	(INCHES)
F4	=	0.2303E-02	MASS FLOW,REGION 4	(LBM./SEC.)
F4P	=	0.5758E-03	EFFECTIVE MASS FLOW REGION 4	LBM./SEC.)
F5	=	0.5758E-03	MASS FLOW,REGION 5	(LBM./SEC.)
F6	=	0.5758E-03	MASS FLOW,REGION 6	(LBM./SEC.)
F7	=	0.5758E-03	MASS FLOW,REGION 7	(LBM./SEC.)
QR	=	0.5042E 01	DYNAMIC PRESSURE RATIO	
S5OS4P	=	0.1802E 02	AREA RATIO REGION 5 TO REGION 4P	

APPENDIX C

MOLECULAR VISCOSITY FOR $H_2/N_2/O_2$ MIXTURES

In modeling of turbulent transport coefficient distributions, it is necessary to know the molecular viscosity at the wall. This parameter, μ_{mix}, is used in von Driest's damping function, and is also the limiting value for the transport coefficient of momentum at the wall where $\epsilon = 0$, i.e.,

$$\mu_{eff} = \epsilon + \mu_{mix} \tag{C.1}$$

where ϵ is the turbulent eddy viscosity.

For flow containing mixtures of gaseous hydrogen, oxygen, and nitrogen, the molecular viscosity may be calculated as follows (ref. 33):

$$\mu_{mix} = \sum_{i=1}^{N} x_i \mu_i / f_i \tag{C.2}$$

$$f_i = \sum_{j=1}^{N} \phi_{ij} x_i \tag{C.3}$$

where

$$\phi_{ij} = \frac{1}{\sqrt{8}} \left(1 + \frac{W_i}{W_j}\right)^{-1/2} \left[1 + \left(\frac{\mu_i}{\mu_j}\right)^{1/2} \left(\frac{W_j}{W_i}\right)^{1/4}\right]^2 \tag{C.4}$$

$W_i \equiv$ Molecular weight of species i

$\mu_i \equiv$ Viscosity of species i

$x_i \equiv$ Mole fraction of species i

$N \equiv$ Total number of species considered

A computer program was written (fig. C.1) to solve equation (C.2) for μ_{mix}, and calculations were performed to check the subroutine and determine the dependence of μ_{mix} on mass or mole fraction of hydrogen. The program was debugged against hand-calculated and redundant check cases. Figure C.2 shows the computed dependence of μ_{mix} of a hydrogen/air mixture. The high degree of nonlinearity between μ_{mix} and x_{H_2} is consistent with comments in reference 33.

```
L.0001          SUBROUTINE XMUMIX(X,XMUBAR)
L.0002    C  CALCULATE VISCOSITY IN H2/O2/N2 GAS MIXTURES
L.0003    C ENTER ROUTINE WITH MOLE FRACTIONS X(I)...I=1(H2),2(O2),3(N2)
L.0004    C LEAVE WITH VISCOSITY XMUBAR(LBM/FT-SEC)
L.0005    C
L.0006    C
L.0007    C       SEE PG. 24 OF BIRD,STEWART AND LIGHTFOOT
L.0008    C       FOR H2,O2,N2 MIXTURES  I=1,2,3 RESPECTIVELY
L.0009          DIMENSION W(3),XMU(3),X(3),PHI(10,10),F(10)
L.0010          DATA W/2.016,32.,28.016/
L.0011          DATA XMU/.00835,.0189,.01657/
L.0012    C     XMU IN CENTIPOISE
L.0013          DATA IONCE/0/
L.0014          IF(IONCE)4,4,5
L.0015    4     IONCE=1
L.0016          PHI(1,2)=1.8564
L.0017          PHI(1,3)=1.919
L.0018          PHI(2,1)=.26472
L.0019          PHI(2,3)=.99847
L.0020          PHI(3,1)=.27403
L.0021          PHI(3,2)=.99986
L.0022          PHI(1,1) = 1.
L.0023          PHI(2,2) = 1.
L.0024          PHI(3,3) = 1.
L.0025    5     CONTINUE
L.0026          DO 1 I=1,3
L.0027    1     F(I) = X(1)*PHI(I,1)+X(2)*PHI(I,2)+X(3)*PHI(I,3)
L.0028          XMUBAR = 0.
L.0029          DO 2 I=1,3
L.0030    2     XMUBAR = XMUBAR+X(I)*XMU(I)/F(I)
L.0031          XMUBAR = XMUBAR*6.72E-4
L.0032          RETURN
L.0033          END
```

Figure C.1. Listing of Mixture Viscosity Computer Program

APPENDIX C

MOLECULAR VISCOSITY FOR $H_2/N_2/O_2$ MIXTURES

In modeling of turbulent transport coefficient distributions, it is necessary to know the molecular viscosity at the wall. This parameter, μ_{mix}, is used in von Driest's damping function, and is also the limiting value for the transport coefficient of momentum at the wall where $\epsilon = 0$, i.e.,

$$\mu_{eff} = \epsilon + \mu_{mix} \tag{C.1}$$

where ϵ is the turbulent eddy viscosity.

For flow containing mixtures of gaseous hydrogen, oxygen, and nitrogen, the molecular viscosity may be calculated as follows (ref. 33):

$$\mu_{mix} = \sum_{i=1}^{N} x_i \mu_i / f_i \tag{C.2}$$

$$f_i = \sum_{j=1}^{N} \phi_{ij} x_i \tag{C.3}$$

where

$$\phi_{ij} = \frac{1}{\sqrt{8}} \left(1 + \frac{W_i}{W_j}\right)^{-1/2} \left[1 + \left(\frac{\mu_i}{\mu_j}\right)^{1/2} \left(\frac{W_j}{W_i}\right)^{1/4}\right]^2 \tag{C.4}$$

$W_i \equiv$ Molecular weight of species i

$\mu_i \equiv$ Viscosity of species i

$x_i \equiv$ Mole fraction of species i

$N \equiv$ Total number of species considered

A computer program was written (fig. C.1) to solve equation (C.2) for μ_{mix}, and calculations were performed to check the subroutine and determine the dependence of μ_{mix} on mass or mole fraction of hydrogen. The program was debugged against hand-calculated and redundant check cases. Figure C.2 shows the computed dependence of μ_{mix} of a hydrogen/air mixture. The high degree of nonlinearity between μ_{mix} and x_{H_2} is consistent with comments in reference 33.

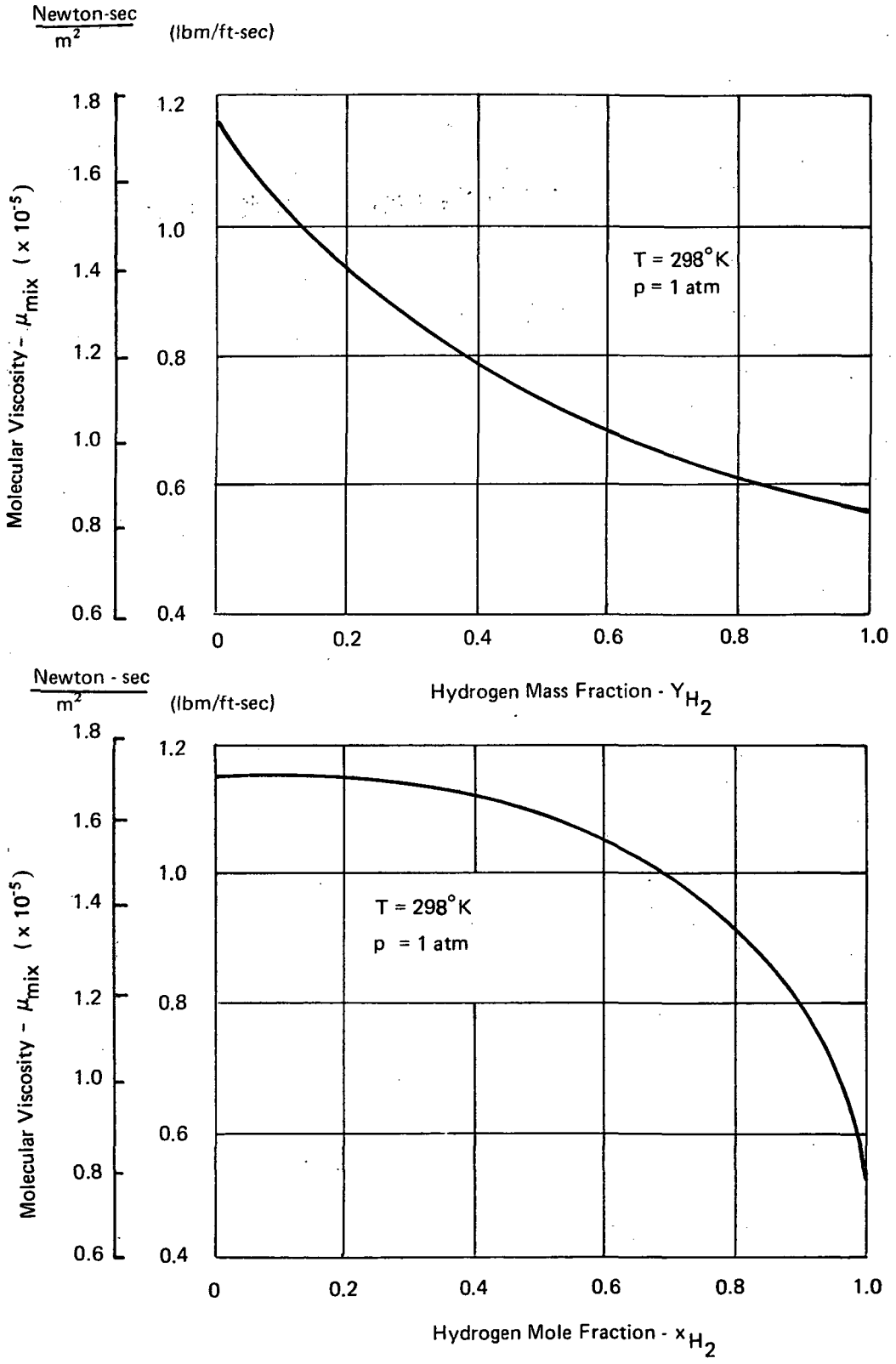

Figure C.2. Computed Molecular Viscosity of Hydrogen/Air Mixtures

REFERENCES

1. Becker, J.V.; and Kirkham, F.S.: Hypersonic Transports, Paper No. 25, NASA SP-292, Nov. 1971.

2. Bushnell, D.: Hypersonic Airplane Aerodynamic Technology, Paper No. 5, NASA SP-292, Nov. 1971.

3. Henry, J.R.; and Beach, H.L.: Hypersonic Air-Breathing Propulsion Systems, Paper No. 8, NASA SP-292, Nov. 1971.

4. Henry, J.R.; and Anderson, G.Y.: Design Considerations for the Airframe-Integrated Scramjet, presented at 1st Int. Sym. on Air-Breathing Engines, Marseille, France, June, 1972.

5. Rogers, R.C.: A Study of the Mixing of Hydrogen Injected Normal to a Supersonic Airstream, NASA TND-6114, Mar. 1971.

6. Rogers, R.C.: Mixing of Hydrogen Injected from Multiple Injectors Normal to a Supersonic Airstream, NASA TND-6476, Sept. 1971.

7. Wagner, J.P.; Cameron, J.M.; and Billig, F.S.: Penetration and Spreading of Transverse Jets of Hydrogen in a Mach 2.72 Airstream, NASA CR-1794, Mar. 1971.

8. Cooke, J; and Hall, M.: Boundary Layers in Three-Dimensions, Progress in Aeronautical Sciences, 2, Ferri, et al., Eds, Pergamon Press, pp. 222-281, 1962.

9. Baker, A.J.: Finite Element Theory for the Mechanics and Thermodynamics of a Viscous, Compressible Multi-Species Fluid, Bell Aerospace Company, Research Report No. 9500-920200, 1971.

10. Baker, A.J.: Finite Element Computational Theory for Three-Dimensional Boundary Layer Flow, AIAA Preprint 72-108, Jan. 1972.

11. Finlayson, B.A.; and Scriven, L.E.: The Method of Weighted Residuals - A Review, Appl. Mech. Rev., 19. No. 9, pp. 735-748, 1966 .

12. Nigro, B.: The Derivation of Optimally Stable, 3-Stage, One-Step, Explicit Numerical Integration Methods, Bell Aerospace Technical Note TCTN-1010, 1971.

13. Baker, A.J.; and Manhardt, P.D.: Finite Element Solution for Energy Conservation Using a Highly Stable Explicit Integration Algorithm, NASA CR-130149, 1972

14. Baker, A.J.: Numerical Solution to the Dynamics of Viscous Fluid Flow by a Finite Element Algorithm; A First Step Towards Computational Continuum Mechanics, Proceedings International Association for Shell Structures Pacific Symposium on Hydromechanically Loaded Shells, 1971.

15. Baker, A.J.: Finite Element Solution Algorithm for Viscous Incompressible Fluid Dynamics, Int. J. Num. Mtd. Engr, to appear.

16. Bradshaw, P.: Calculation of Three-Dimensional Turbulent Boundary Layers, J. Fluid Mech., 46, Part 3, pp. 417-445, 1971.

17. Nash, J.F.: The Calculation of Three-Dimensional Turbulent Boundary Layers in Incompressible Flow, J. Fluid Mech., 37, Part 4, 625-642, 1969.

18. Nash, J.F.: An Explicit Scheme for the Calculation of Three-Dimensional Turbulent Boundary Layers, ASME Preprint No. 71-FE-19, 1971.

19. Morgenthaler, J.H.: Supersonic Mixing of Hydrogen and Air, NASA CR-747, 1967.

20. Kline, S.J.; Morkovin, M.V.; Sovran, G.; and Cockrell, D.L. Editors,: Proceedings Computation of Turbulent Boundary Layers, 1968, Stanford University.

21. Zelazny, S.W.; Morgenthaler, J.H.; and Herendeen, D.L.: Shear Stress and Turbulent Intensity Models for Coflowing Axisymmetric Streams, AIAA Preprint 72-47, Jan. 1972. (Accepted for publication in AIAA J.)

22. Morgenthaler, J.H.; and Zelazny, S.W.: Predictions of Axisymmetric Free Turbulent Shear Flows Using a Generalized Eddy Viscosity Approach, presented at the Langley Working Conference on Free Turbulent Shear Flows, Hampton, Virginia, July 20-21, 1972. (To be published in a NASA SP.)

23. von Driest, E.R.: On Turbulent Flow Near a Wall, Journal of the Aeronautical Sciences, 23, No. 11, pp. 1007-1011, 1956.

24. Hinze, J.O.: Turbulence, McGraw-Hill, 1959.

25. Billig, F.S.; Orth, R.C.; Lasky, M.: A Unified Analysis of Gaseous Jet Penetration, AIAA J. 9, No. 6, pp. 1048-1057, 1971.

26. Orth, R.C.; Schetz, J.A.; and Billig, F.S.: The Interaction and Penetration of Gaseous Jets in Supersonic Flow, NASA CR 1386, 1969.

27. Wu, Jain-Ming; and Aoyama, Kinya: Analysis of Transverse Secondary Injection Penetration into Confined Supersonic Flow, AIAA Paper No. 69-2, 1969.

28. Werle, M.J.: Jet-Interaction-Induced Separation: The Two-Dimensional Problem, AIAA J.,10, No. 2, pp. 188-193, 1972.

29. Hains, F.D. and Baker, A.J.: Binary Diffusion of a Jet Imbedded in a Boundary Layer; AIAA J., 10, No. 7, pp. 938-940, 1972.

30. Morretti, G.: A New Technique for the Numerical Analysis of Non-Equilibrium Flows, AIAA J., 3, No. 2, pp. 223-229, 1965.

REFERENCES

1. Becker, J.V.; and Kirkham, F.S.: Hypersonic Transports, Paper No. 25, NASA SP-292, Nov. 1971.

2. Bushnell, D.: Hypersonic Airplane Aerodynamic Technology, Paper No. 5, NASA SP-292, Nov. 1971.

3. Henry, J.R.; and Beach, H.L.: Hypersonic Air-Breathing Propulsion Systems, Paper No. 8, NASA SP-292, Nov. 1971.

4. Henry, J.R.; and Anderson, G.Y.: Design Considerations for the Airframe-Integrated Scramjet, presented at 1st Int. Sym. on Air-Breathing Engines, Marseille, France, June, 1972.

5. Rogers, R.C.: A Study of the Mixing of Hydrogen Injected Normal to a Supersonic Airstream, NASA TND-6114, Mar. 1971.

6. Rogers, R.C.: Mixing of Hydrogen Injected from Multiple Injectors Normal to a Supersonic Airstream, NASA TND-6476, Sept. 1971.

7. Wagner, J.P.; Cameron, J.M.; and Billig, F.S.: Penetration and Spreading of Transverse Jets of Hydrogen in a Mach 2.72 Airstream, NASA CR-1794, Mar. 1971.

8. Cooke, J; and Hall, M.: Boundary Layers in Three-Dimensions, Progress in Aeronautical Sciences, 2, Ferri, et al., Eds, Pergamon Press, pp. 222-281, 1962.

9. Baker, A.J.: Finite Element Theory for the Mechanics and Thermodynamics of a Viscous, Compressible Multi-Species Fluid, Bell Aerospace Company, Research Report No. 9500-920200, 1971.

10. Baker, A.J.: Finite Element Computational Theory for Three-Dimensional Boundary Layer Flow, AIAA Preprint 72-108, Jan. 1972.

11. Finlayson, B.A.; and Scriven, L.E.: The Method of Weighted Residuals - A Review, Appl. Mech. Rev., 19. No. 9, pp. 735-748, 1966.

12. Nigro, B.: The Derivation of Optimally Stable, 3-Stage, One-Step, Explicit Numerical Integration Methods, Bell Aerospace Technical Note TCTN-1010, 1971.

13. Baker, A.J.; and Manhardt, P.D.: Finite Element Solution for Energy Conservation Using a Highly Stable Explicit Integration Algorithm, NASA CR-130149, 1972

14. Baker, A.J.: Numerical Solution to the Dynamics of Viscous Fluid Flow by a Finite Element Algorithm; A First Step Towards Computational Continuum Mechanics, Proceedings International Association for Shell Structures Pacific Symposium on Hydromechanically Loaded Shells, 1971.

31. Tyson, T.J.; and Kliegel, J.R.: An Implicit Integration Procedure for Chemical Kinetics, AIAA Paper 68-180, 1968.

32. Morgenthaler, J.H.; Zelazny, S.W.; Rudinger, G.: High Speed Turbulent Mixing and Combustion Application to Advanced Air Breathing Propulsion Engines, Bell Aerospace Report 9500-920258. 1973.

33. Bird, R.B.; Stewart, W.E.; and Lightfoot, E.N: Transport Phenomena, J. Wiley and Sons, 1960.